Communauté d'Universités et d'Établissements Lille Nord de France

Université de Lille

FACULTÉ DES SCIENCES ET TECHNOLOGIES

Unité Mécanique Lille UML J.Boussinesq

Université de Lille

Doctoral School **ED Régionale SPI 72**

Laboratory **Unité de Mécanique de Lille - Joseph Boussinesq**

Thesis defended by **Dário Oliveira Canossi**

Defended on **22nd November, 2019**

In order to become Doctor from Université de Lille

Academic Field **Mechanics, Energetics, Materials**

Speciality **Fluid Mechanics**

Thesis Title

Numerical simulation of the transition to elastic turbulence in viscoelastic inertialess flows

Thesis supervised by

Prof. Gilmar Mompean	Supervisor
Dr. Stefano Berti	Co-Advisor

Committee members

Referees	Prof. Manuel Alves	FEUP – Universidade do Porto	
	Dr. Serge Simoëns	CNRS LMFA – École Centrale de Lyon	
Examiners	Prof. Najib Ouarzazi	Université de Lille	Committee President
	Dr. Alexandre Delache	LMFA – Université de Saint-Étienne	
	Dr. Silvia Hirata	Université de Lille	
Invited	Dr. Stefano Berti	Université de Lille	
Supervisor	Prof. Gilmar Mompean	Université de Lille	

Communauté d'Universités et d'Établissements Lille Nord de France

Université de Lille

FACULTÉ DES SCIENCES ET TECHNOLOGIES

Unité Mécanique Lille UML J.Boussinesq

Université de Lille

Doctoral School **ED Régionale SPI 72**

Laboratory **Unité de Mécanique de Lille - Joseph Boussinesq**

Thesis defended by **Dário Oliveira Canossi**

Defended on **22nd November, 2019**

In order to become Doctor from Université de Lille

Academic Field **Mechanics, Energetics, Materials**

Speciality **Fluid Mechanics**

Thesis Title

Numerical simulation of the transition to elastic turbulence in viscoelastic inertialess flows

Thesis supervised by

Prof. Gilmar Mompean	Supervisor
Dr. Stefano Berti	Co-Advisor

Committee members

Referees	Prof. Manuel Alves	FEUP – Universidade do Porto	
	Dr. Serge Simoëns	CNRS LMFA – École Centrale de Lyon	
Examiners	Prof. Najib Ouarzazi	Université de Lille	Committee President
	Dr. Alexandre Delache	LMFA – Université de Saint-Étienne	
	Dr. Silvia Hirata	Université de Lille	
Invited	Dr. Stefano Berti	Université de Lille	
Supervisor	Prof. Gilmar Mompean	Université de Lille	

Communauté d'Universités et d'Établissements Lille Nord de France

Université de Lille

FACULTÉ DES SCIENCES ET TECHNOLOGIES

Unité Mécanique Lille UML J.Boussinesq

Université de Lille

École doctorale **ED Régionale SPI 72**

Laboratoire **Unité de Mécanique de Lille - Joseph Boussinesq**

Thèse présentée par **Dário Oliveira Canossi**

Soutenue le 22 **novembre 2019**

En vue de l'obtention du grade de docteur de l'Université de Lille

Discipline **Mécanique, Énergétique, Matériaux**

Spécialité **Mécanique des Fluides**

Titre de la thèse

Simulation numérique de la transition à la turbulence élastique dans des écoulements viscoélastiques sans inertie

Thèse dirigée par	Prof. Gilmar Mompean	directeur
	Dr. Stefano Berti	co-encadrant

Composition du jury

Rapporteurs	Prof. Manuel Alves	FEUP – Universidade do Porto	
	Dr. Serge Simoëns	CNRS LMFA – École Centrale de Lyon	
Examinateurs	Prof. Najib Ouarzazi	Université de Lille	président du jury
	Dr. Alexandre Delache	LMFA – Université de Saint-Étienne	
	Dr. Silvia Hirata	Université de Lille	
Invité	Dr. Stefano Berti	Université de Lille	
Directeur de thèse	Prof. Gilmar Mompean	Université de Lille	

Keywords: numerical simulation, elastic turbulence, viscoelastic fluid, cross-slot, high-Weissenberg number problem, finite-volume method, Oldroyd-B, OpenFOAM, mixing

Mots clés : simulation numérique, turbulence élastique, fluide viscoélastique, cross-slot, problème du haut nombre de Weissenberg, méthode des volumes finis, Oldroyd-B, OpenFOAM, mélange

This thesis has been prepared at

Unité de Mécanique de Lille - Joseph Boussinesq
(UML) EA 7512
Université de Lille - Cité Scientifique
Bâtiment ESPRIT
Avenue Henri Poincaré
59655 Villeneuve d'Ascq, France

☎ +33 (0)3 20 33 71 74
Web Site uml.univ-lille.fr

*À mon père bien-aimé, Gianpietro Canossi (*in memoriam*)*

Do not fear to be eccentric in opinion, for every opinion now accepted was once eccentric.

Bertrand Russell

Acknowledgements

I am immensely thankful to my mother Regina Canossi and my twin brother Mário Canossi, who never stopped motivating me and providing emotional support, since the first day of my thesis and for its entire duration.

A very special gratitude goes out to professor Gilmar Mompean, who offered me the opportunity to engage in this work, giving fundamental advices throughout my research. With a special mention to my co-advisor, professor Stefano Berti, whose contribution was critical and whose door has always been open to my insistent questioning.

To live in another country, far from family and friends, can sometimes be very tough. Firstly, I thank those who supported me even before arriving in France: Cristina Martinsh and professors Douglas Riffel and Paulo Mário. Then, I must express my profound gratitude to my friend and training partner Antoine Duhamel, and specially to Mia Decat, for her lovely and sincere friendship, as well as her decisive presence in good and bad moments.

I am also grateful for all the precious moments and support given by the Brazilian community in the city of Lille, represented here by my ex-workmates and now special friends Ramon Martins and João Rodrigo. I also thank my laboratory colleagues, in particular Himani Garg, Vinicius Tergolina and Thaynan Oliveira. Without their daily companionship, my Ph.D. thesis would have been a lot more arduous.

My sincere thanks goes to professors Manuel Alves and Serge Simoëns for accepting the invitation to be the reviewers of this work, and to the other members of my thesis committee: professors Alexandre Delache, Silvia Hirata and Najib Ouarzazi.

I would also like to acknowledge the *Conselho Nacional de Desenvolvimento Científico e Tecnológico* (CNPq) from Brazil for providing the funding for my work, and the *Calcul Scientifique Intensif* team from the University of Lille for the access and valuable help with the University supercomputer.

And finally, I thank all the people who contributed for this long-awaited moment to become real.

Thanks for all your encouragement!

Numerical simulation of the transition to elastic turbulence in viscoelastic inertialess flows

Abstract

Fluid mixing represents an important component of the field of fluid dynamics, what makes the understanding of this subject so meaningful from both the fundamental and applied (*e.g.* industrial processes) point of view. In miniaturised geometries, under typical conditions, mixing is a slow, difficult and inefficient process due to the naturally laminar character of these flows, which forces the homogenisation of different fluid elements to occur via molecular diffusion instead of faster-acting advective transport. However, recent experimental studies on low-Reynolds-number viscoelastic flows have shown that efficient mixing can be triggered in several geometrical configurations (including micro-scale devices), by the phenomenon of elastic turbulence. The first part of this thesis is devoted to the understanding and investigation of numerical challenges present in the domain of non-Newtonian fluid dynamics, focusing in particular on the high-Weissenberg number problem. The latter manifests as a breakdown of the numerical scheme when the polymeric extra-stress evolution equations are implemented in a direct way, which poses severe limits to the possibility to accurately simulate elastic turbulent flows. We provide numerical evidence of the beneficial effect (in terms of increased stability) of the square-root decomposition of the extra-stress in a finite-volume-based implementation of the governing equations in a two-dimensional channel. The second part of the thesis reports about the emergence and characterisation of purely elastic instabilities in numerical simulations of zero-Reynolds-number Oldroyd-B fluids in a two-dimensional cross-slot geometry. By means of extensive numerical work, we provide a detailed characterisation of the purely elastic instabilities arising in the system for wide ranges of both the fluid elasticity and the polymer concentration. For concentrated solutions and large enough Weissenberg numbers, our simulations indicate the emergence of disordered flow pointing to elastic turbulence. We analyse the transition to irregular dynamics and characterise the statistical properties of such highly elastic flows, discussing the similarities and differences with experimental results from the literature.

Keywords: numerical simulation, elastic turbulence, viscoelastic fluid, cross-slot, high-Weissenberg number problem, finite-volume method, Oldroyd-B, OpenFOAM, mixing

Simulation numérique de la transition à la turbulence élastique dans des écoulements viscoélastiques sans inertie

Résumé

Le mélange de fluides représente un élément important du domaine de la dynamique des fluides, ce qui rend la compréhension de ce sujet si significative du point de vue fondamental et appliqué (*p. ex.*, les processus industriels). Dans les géométries miniaturisées (dans des conditions typiques) le mélange est un processus lent, difficile et inefficace. Cela en raison du caractère naturellement laminaire de ces écoulements, qui oblige l'homogénéisation de différents éléments fluides à se produire par diffusion moléculaire au lieu d'un transport advectif, à l'action plus rapide. Cependant, des études expérimentales récentes sur les écoulements viscoélastiques à faible nombre de Reynolds ont montré qu'un mélange efficace peut être déclenché dans plusieurs configurations géométriques (y compris les dispositifs à l'échelle microscopique), par le phénomène de la turbulence élastique. La première partie de cette thèse est consacrée à la compréhension et à l'investigation des défis numériques présents dans le domaine de la dynamique des fluides non newtonienne, en se concentrant plus particulièrement au problème du haut nombre de Weissenberg. Ce dernier se manifeste par une rupture du schéma numérique, lorsque les équations d'évolution d'extra-contraintes polymériques sont évaluées de façon directe. Ceci pose des limites importantes à la possibilité de simuler avec précision des écoulements turbulents-élastiques. Nous fournissons des preuves numériques de l'effet bénéfique (en termes de gain en stabilité) de la décomposition en racine carrée de l'extra-contrainte dans une implémentation en volumes finis des équations régissant l'écoulement dans un canal bidimensionnel. La deuxième partie de la thèse traite de l'émergence et de la caractérisation d'instabilités purement élastiques dans des simulations numériques de fluides Oldroyd-B à nombre de Reynolds zéro dans une géométrie du type *cross-slot* bidimensionnel. Grâce à un travail numérique approfondi, nous présentons une caractérisation détaillée des instabilités purement élastiques. Ces instabilités apparaissant dans le système pour de larges plages d'élasticité du fluide et de concentration des polymères. Pour les solutions concentrées et des nombres de Weissenberg assez grands, nos simulations indiquent l'apparition d'un écoulement désordonné pointant vers la turbulence élastique. Nous analysons le passage à une dynamique irrégulière et caractérisons les propriétés statistiques de tels écoulements très élastiques, en discutant des similitudes et des différences avec les résultats expérimentaux de la littérature.

Mots clés : simulation numérique, turbulence élastique, fluide viscoélastique, cross-slot, problème du haut nombre de Weissenberg, méthode des volumes finis, Oldroyd-B, OpenFOAM, mélange

Abbreviations

2D two-dimensional. 18, 40, 73, 83, 85, 86

3D three-dimensional. 23, 30, 47, 50, 75

AVSS Adaptive Viscoelastic Stress Splitting. 19

CFD computational fluid dynamics. 17, 53, 59, 85

CFL Courant-Friedrichs-Lewy. 26, 61, 62

CUBISTA Convergent and Universally Bounded Interpolation Scheme for the Treatment of Advection. 54, 60

CV control volume. 22–24

DNA deoxyribonucleic acid. 44

DNS direct numerical simulation. 2

EEME Explicitly Elliptic Momentum Equation. 19

EFOR Extensional Flow Oscillatory Rheometer. 44

EVSS Elastic-Viscous Split Stress. 19

FENE Finitely Extensible Non-linear Elastic. 12, 14, 15, 50, 54, 87

GP geometric progression. 109

HRS high-resolution discretisation scheme. 54, 60

HWNP high Weissenberg number problem. 2, 3, 18, 29

LCR log-conformation representation. 3, 20, 40, 55

MAC Marker-and-Cell. 27

OpenFOAM® Open Source Field Operation and Manipulation. 4, 40, 53–55, 59, 61, 80, 85, 111

pdf probability density function. 73, 75, 78, 83, 86

PISO Pressure-Implicit with Splitting of Operators. 54

PMcK Pakdel-McKinley. 43

QUICK Quadratic Upstream Interpolation Scheme for the Convective Kinematics. 23–25

rms root-mean-square. 72

SIMPLEC Semi-Implicit Method for Pressure-Linked Equations-Consistent. 54

SPD symmetric positive definite. 13, 29, 105

UCM upper-convected Maxwell. 12, 13, 15, 19, 46, 69, 76–78, 80, 83, 85–87

UDS upwind differencing scheme. 23–25

Symbols

$\boldsymbol{a}$	generic anti-symmetric tensor
A	scale parameter of the cross-slot bifurcation
A_{in} and A_{out}	surface area of opposite faces in a control volume
A_r	length-to-width aspect ratio of the cross-slot arm
$\boldsymbol{b}$	square-root tensor
β	solvent-to-total viscosity ratio
$\boldsymbol{c}$	conformation tensor
C	Courant number
C_{max}	maximum Courant number
d	cross-slot arm width
De	Deborah number
$\partial/\partial i$	partial differential operator
δ	power-law exponent
Δt	time step
Δt_a	advection time step
Δt_d	diffusion time step
Δx	distance between mesh nodes, in the streamwise direction
Δy	distance between mesh nodes, in the wall-normal direction
Δz	distance between mesh nodes, in the spanwise direction
Δx_{min} and Δy_{min}	cross-slot minimal grid spacing
$E(f)$	power spectra in the temporal domain
$E(k)$	power spectra in the spatial domain
E^{tot}	total energy
$\dot{\varepsilon}$	strain rate
$\dot{\varepsilon}_0$	strain rate at the cross-slot stagnation point
η_p	polymeric viscosity

η_s	solvent viscosity
η_t	total viscosity
$f(tr(\boldsymbol{c}))$	Peterlin function
f_s	cross-slot stretching factor
$\boldsymbol{F}$	generic continuously differentiable vector field
$\boldsymbol{\mathcal{F}}$	body forces vector
γ and φ	generic spatial directions
$\dot{\gamma}$	shear rate
$\dot{\boldsymbol{\gamma}}$	rate-of-strain tensor
H	dumbbell spring constant
i	mesh index, in the streamwise direction
$\boldsymbol{I}$	identity tensor or matrix
∞	infinity
j	mesh index, in the wall-normal direction
k	mesh index, in the spanwise direction
k_B	Boltzmann constant
L	channel half-width
L^2	maximum stretch of polymer molecules
L_c	characteristic flow length scale
λ	characteristic relaxation time
μ	Newtonian dynamic viscosity
$\boldsymbol{n}$	unitary normal vector field
N	number of mesh cells in the cross-slot central region
N_1	first normal stress difference
$\boldsymbol{\nabla}$	gradient operator
$\boldsymbol{\nabla}\cdot$	divergence operator
ν_0	kinematic viscosity
$\mathcal{O}$	order estimator

p	pressure
Q_a	cross-slot asymmetric flow parameter
Q_{in}	cross-slot inflow
Q_{out}	cross-slot outflow
$\boldsymbol{R}$	end-to-end vector
Re	Reynolds number
${R_{eq}}^2$	molecule size in the equilibrium state
ρ	mass density
σ	standard deviation
$\boldsymbol{\sigma}$	viscous solvent tensor
t	temporal coordinate
T	matrix transpose operator
t_c	characteristic observation time
$\mathcal{T}$	absolute temperature
$\boldsymbol{\tau}$	elastic extra-stress tensor
τ_{xx}, τ_{yy} and τ_{zz}	normal components of the extra-stress tensor
τ_{xy}, τ_{xz} and τ_{yz}	shear components of the extra-stress tensor
$\boldsymbol{\Theta}$	logarithmic tensor
$\boldsymbol{u}$	velocity vector
u_{avg}	mean flow velocity
U_b	bulk average velocity magnitude
U_c	characteristic flow velocity scale
u_{in} and u_{out}	interpolated velocities entering and exiting a control volume
$\boldsymbol{u}_L$	instantaneous velocity of a Lagrangian particle
u_x and u	streamwise (axial) velocity component
u_y and v	wall-normal (transversal) velocity component
u_z and w	spanwise velocity component
Wi	Weissenberg number
Wi_0	local Weissenberg number at the cross-slot centre
$Wi_c^{(\mathrm{I})}$	critical Weissenberg for the first cross-slot instability
$Wi_c^{(\mathrm{II})}$	critical Weissenberg for the second cross-slot instability
x	streamwise (axial) spatial component

$\boldsymbol{x}$	position vector
$\boldsymbol{x}_*^{(1)}$, $\boldsymbol{x}_*^{(2)}$ and $\boldsymbol{x}_*^{(3)}$	positions of cross-slot probes
$\boldsymbol{x}_L$	instantaneous position of a Lagrangian particle
$\boldsymbol{\Xi}$	total stress tensor
y	wall-normal (transversal) spatial component
z	spanwise spatial component

Summary

List of Tables

List of Figures

Introduction

A *fluid* is a material that is unable to sustain the application of shear stress without undergoing some kind of deformation. When describing such deformation of fluid parcels, the term *fluid flow* is employed. For centuries, the scientific knowledge over the broad field of Fluid Mechanics has been developed, improved and formalised focusing mainly on Newtonian fluids, whose flow is accurately described by the famous Navier-Stokes equation. In the last century though, interest on non-Newtonian fluids has sharply grown among the scientific community, as more and more unexpected phenomena related to *e.g. viscoelastic* flow behaviour were discovered and explained.

Fluid mixing represents an important component of the field of fluid dynamics, where the association of two or more material components must efficiently and in a practical way produce homogeneous solutions [1–4]. Understanding of this subject is thus quite meaningful from both the fundamental and applied (*e.g.* industrial processes) point of view. In miniaturised geometries, under typical conditions, mixing is a slow, difficult and inefficient process due to the naturally laminar character of these flows, which forces the homogenisation of different fluid elements to occur via molecular diffusion instead of faster-acting advective transport [5]. However, recent experimental studies on low-Reynolds-number viscoelastic flows have shown that efficient mixing (as *e.g.* in Fig. 1) can be triggered in several geometrical configurations (including micro-scale devices), by the phenomenon of elastic turbulence [1, 6–8].

In their seminal work, Groisman and Steinberg [9] reported that purely elastic instabilities produced in a specific geometric setup may lead to a molecular coil-stretch transition [10, 11] and consequent appearance of chaotic flows corresponding to a dynamical regime known as *elastic turbulence*. In particular, this regime is characterised by a whole range of active scales, irregular temporal behaviour, growth of flow resistance by a factor up to twenty and enhanced mixing properties. Following its pioneer discovery, the elastic turbulence phenomenon has been induced and characterised in many different flow setups, numerically and through experiments [7, 12–21]. Heat transfer processes are known to be enhanced as well in fluid flows undergoing this disordered regime, as it was recently proved for a von Karman swirling flow [22], a cross-slot setup [23] and a curvilinear microchannel [24, 25].

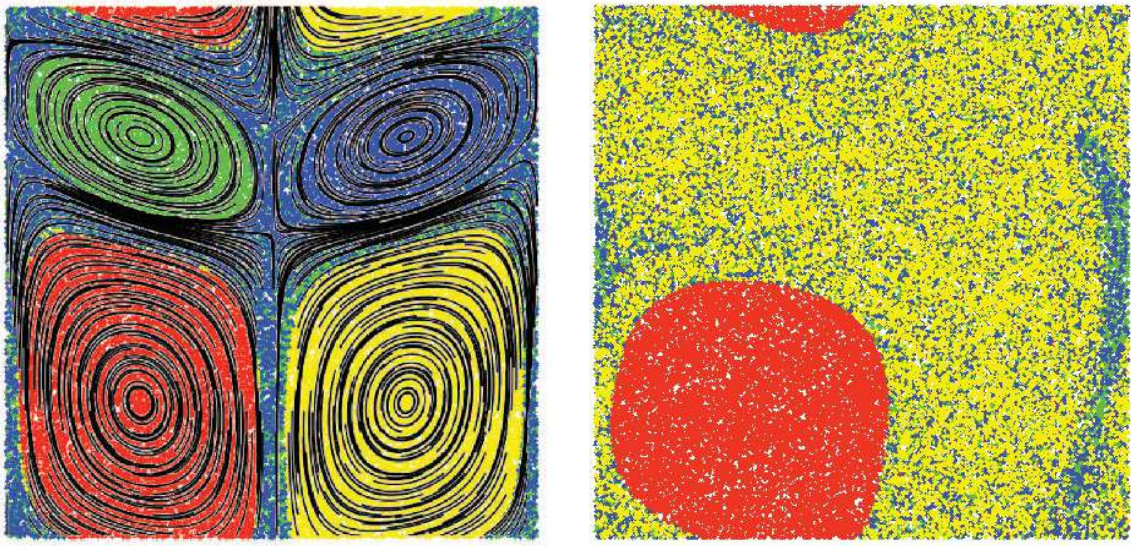

(a) $Wi = 6$ (b) $Wi = 10$

Figure 1 – Lagrangian particle distributions for different elasticity levels – expressed in terms of the Weissenberg (Wi) number – in a viscoelastic fluid flow driven by a simple periodic background force, illustrating its mixing properties (extracted from [8]).

Recently, Samanta et al. [26] pointed out that the inertial turbulence, occurring for high-Reynolds non-Newtonian fluid flows, seems to be related to the elastic turbulence, by performing experiments on viscoelastic pipe flows and direct numerical simulation (DNS) on three-dimensional straight channels. The authors introduced the concept of *elasto-inertial turbulence*, since the instability mechanism that was found to delay the transition point where turbulence would be initially observed relied upon an interaction between elastic stresses and a non-negligible amount of inertia. Moreover, it was theorised that making further progresses in the understanding of the turbulent drag reduction problem can be related to a better comprehension of key features of the elastic turbulence [27].

However, performing numerical simulations of fluid flows undergoing the elastic-turbulent regime is far from an easy task. Since the late 1970's, we know that existing models of viscoelastic fluids present challenging problems for numerical computation [28], among which the most outstanding one is the high Weissenberg number problem (HWNP) [29, 30]. The latter manifests as a breakdown of the numerical scheme when the polymeric extra-stress evolution equations are implemented in a direct way [31], which poses severe limits to the possibility to accurately simulate elastic turbulent flows; after its discovery, it has indeed been considered one of the biggest obstacles from providing solutions for viscoelastic fluid flows, beyond some elasticity level. In this context, several miscellaneous attempts were made to improve numerical stability when solving the constitutive equations of viscoelastic models. An artificially large global (or local) stress diffusion term can be included into the numerical

problem [32, 33], although this proposal was very recently found to have a dramatic effect on the qualitative spatial and temporal dynamics of some fluid flows [34]; instead, one can employ a mathematical stabilising tool, in which some kind of decomposition or factorisation of the conformation tensor is taken in account, as in the pioneer strategy of the log-conformation representation (LCR) by Fattal and Kupferman [35] and its subsequent adapted versions. In Fig. 2, we can remark the appearance of numerical oscillations as a consequence of the HWNP.

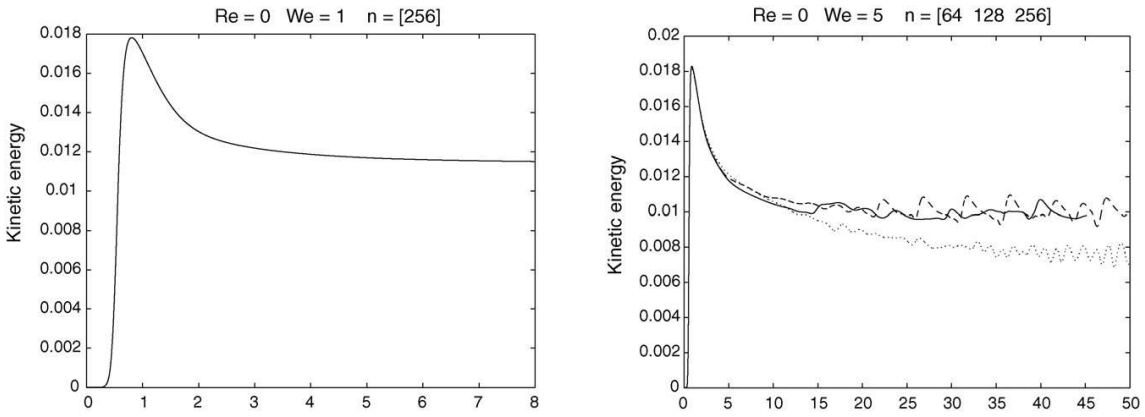

(a) $Wi = 1$ (b) $Wi = 5$

Figure 2 – Kinetic energy as a function of time, for an Oldroyd-B fluid flow in a lid-driven cavity. As the elasticity increases, strong oscillations arise due to the HWNP, but the implemented LCR tool guarantees numerical stability (extracted from [36]).

Despite the indisputable progress observed over the last few decades, computing stable and accurate numerical flow solutions at arbitrarily high elasticity levels remains a non-trivial and thus unreached task. It is generally acknowledged that much research is yet to be carried out in the field of numerical simulation of viscoelastic fluid flows, a fact which provides a strong motivation for the first part of this thesis.

The second part of the present document reports about the emergence and characterisation of purely elastic instabilities in numerical simulations of inertialess Oldroyd-B fluids in a two-dimensional *cross-slot* geometry. The cross-slot, made of two perpendicularly intersecting channels with two inlets and two outlets was chosen as our main work geometry for the following reasons. Mainly, it is considered as one of the most representative cases of geometries with stagnation points, with great potential for a mixing system and a fundamental device for extensional rheometric measurements [37]. So, understanding and characterisation of flow phenomena in this geometry is fundamental for developing such fluidic apparatuses. Cross-slot devices were employed even for the evaluation and improvement of viscoelastic constitutive equations, in numerical studies and in experiments [38, 39]. Besides that, elastic turbulence states have never been, to the best of our knowledge, numerically obtained in this geometrical setup.

Objectives

This document is subdivided in two parts, with distinct objectives from the standpoint of the expected results.

Part I of this manuscript brings an extensive analysis of the implementation of stabilising tools into a in-house flow solver code, with the objective of establishing the powerfulness of mathematical formulations recently derived for that purpose. These numerical methodologies concern the evolution equation of the extra-stress tensor for viscoelastic models, coupled with the momentum and the mass conservation equations. The degree of improvement on the numerical stability of the code, lead by the implemented tools, will equally be assessed.

Part II of the thesis considers numerical studies performed in a powerful and stable open-source viscoelastic solver (the OpenFOAM® toolbox), which already possesses the numerical tools dealt with in the first part. The main objective here is to provide a comprehensive mapping of the different flow states that arise in a two-dimensional cross-slot geometry as a function of the variation of several parameters and to establish through numerical and statistical investigations if, for sufficiently high elasticity levels, the phenomenon of elastic turbulence can be identified in this geometry.

Organisation of the thesis

I. **Improvement of a finite-volume-based flow solver through the implementation of stabilising numerical tools**

The first part of the document starts by presenting, in Chapter 1, the theory behind the mathematical description employed for modelling viscoelastic fluid flows, following some of the available constitutive models; then, in the same Chapter, we bring a review on particular challenges inside the domain of numerical fluid dynamics and introduce different techniques adopted for stabilising the evolution of the extra-stress equation, present in constitutive models. In Chapter 2 we present in great detail the structure of the in-house numerical code named Gilcart and its specificities. The original methods handled by the algorithm are explained, from which a solver was developed to simulate three-dimensional unsteady flows in complex geometries. Then, we describe the mathematical factorisation implemented and provide numerical evidence of the beneficial effect (in terms of increased stability) of the square-root decomposition of the extra-stress tensor in a finite-volume-based implementation of the governing equations in a two-dimensional channel. As a concluding topic of this Chapter, an argumentation is built concerning the need for substituting our in-house solver to achieve even more stable simulations and substantial results.

II. **Viscoelastic fluid flows in a two-dimensional cross-slot and transition to elastic turbulence**

In Chapter 3 we present the compilation of a bibliographic review relating to the second part of the thesis. It encompasses past and recent advances in the study of purely elastic instabilities and the elastic turbulence phenomenon in itself, for multiple setups; focus here is given to experiments and numerical simulations in the cross-slot device. The alternative flow solver and the numerical methods already available on it are specified in Chapter 4, where we also detail the cross-slot geometric model, specific boundary and initial conditions of the problem and meshing procedures. Last, but not least, we provide in Chapter 5, by means of extensive numerical work, a detailed characterisation of the purely elastic instabilities arising in the system for wide ranges of both the fluid elasticity and the polymer concentration. For concentrated solutions and large enough Weissenberg numbers, our simulations indicate the emergence of disordered flow pointing to elastic turbulence. We analyse the transition to irregular dynamics and characterise the statistical properties of such highly elastic flows, discussing the similarities and differences with experimental results from the literature. A Section on the ability of the chaotic cross-slot flows to generate mixing is also provided. In the end, general conclusions are drawn and future perspectives are offered.

Part I

Improvement of a finite-volume-based flow solver through the implementation of stabilising numerical tools

Chapter 1

Mathematical modelling of viscoelastic fluid flows and numerical challenges

1.1 Navier-Stokes equation

Modelling fluid motion and transport phenomena requires some assumptions and considerations to be made, regarding physical properties and the dynamics of the fluid particles. By assuming general assumptions in that regard, the French engineer Claude-Louis Navier together with the Irish physicist George Stokes derived independently the prominent Navier-Stokes equation, based on basic principles of classical mechanics – mass and momentum conservation (inherited from Newton's second law) and conservation of energy – and whose solution is the flow velocity and pressure fields [40].

The general form of the Navier-Stokes equation (which encompasses both three-dimensional compressible and incompressible fluid flows) is indeed a set of four coupled partial differential equations: one for the mass conservation and one for each component of the momentum conservation. In a differential index notation for a Cartesian coordinate system, it writes:

$$\frac{\partial \rho}{\partial t} + \frac{\partial (\rho u_i)}{\partial x_i} = 0, \tag{1.1}$$

$$\frac{\partial (\rho u_i)}{\partial t} + \frac{\partial \left(\rho u_j u_i\right)}{\partial x_j} = \frac{\partial \tau_{ij}}{\partial x_j} - \frac{\partial}{\partial x_i}\left(p + \frac{2}{3}\mu \frac{\partial u_j}{\partial x_j}\right), \tag{1.2}$$

where x_i is the i^{th} spatial coordinate, u_i is the velocity of the flow in the direction of axis i, p is the pressure field and t the temporal coordinate. τ_{ij} refers to the j^{th} component of the total stress acting on the faces of the elementary fluid element perpendicular to axis i. The physical parameters ρ and μ stand for the mass density and the dynamic

viscosity of the fluid, respectively. Note that in this notation, repeated indices indicate a summation.

Decades of experimental studies in the most varied and conceivable setups proved the accuracy of the Navier-Stokes equation for low molecular weight *Newtonian* fluid flows. This class of fluids comprises all fluids that obey Newton's law of viscosity, a simple equation that dates back to 1687 and was devised by sir Isaac Newton, being represented mathematically in Eq. 1.3. This formula states that viscous stresses generated from the fluid flow are linearly proportional to the deformation rate undergone, with the fluid viscosity μ being the proportionality constant. For these fluids, viscosity is exclusively dependent on temperature.

$$\tau_{ij} = \mu\left(\frac{\partial u_i}{\partial x_j} + \frac{\partial u_j}{\partial x_i}\right). \tag{1.3}$$

The Navier-Stokes equation is more challenging that one may consider. Given its outstanding complexity, even the existence and smoothness of solutions in three-dimensional space (given some initial conditions) is an open problem in the fields of mathematics and physics [41]. In most practical cases, even simplified variants of Eqs. 1.1 and 1.2 cannot be solved analytically by currently known tools and numerical methods must be employed to approximate solutions, instead.

1.2 Non-Newtonian fluids

Most of real world fluids are *non-Newtonian* though, from which the *viscoelastic fluids* (also known as *polymeric fluids*) compose quite a large subclass. The rheological behaviour of viscoelastic flows can be related to strongly non-linear phenomena, also at vanishingly small inertia, as a consequence of an association of viscous and elastic effects (hence the *viscoelastic* designation).

1.2.1 Polymers and polymer solutions

Polymers are large molecules usually formed by the polymerisation of (thousands of) simple repeating chemical units called monomers [42]. When immersed in fluid solutions where velocity gradients are present, long polymer molecules have the ability to coil, stretch and tumble, which generally leads to an alteration of the dynamics of the carrying fluid; the nature of the flow strongly affects the amount of distortion that a single polymer molecule may undergo. For instance, pure extensional flows have a greater ability to stretch and orient flexible polymer molecules compared to simple steady shear flows [43, 44]. Polymer solutions typically behave as non-Newtonian viscoelastic fluids and differ from simple Newtonian fluids in a particular aspect called *fluid memory*:

the total stress applied to the fluid does not immediately become zero when the fluid returns to a static regime, but rather decays with a characteristic relaxation time λ. For polymer solutions, λ actually corresponds to the largest value in the spectrum of relaxation times displayed by polymer molecules [45].

These non-linear rheological effects can generate enhanced normal stress differences [46], resulting in complex flow regimes, which can be of major importance in many scientific and industrial applications. Many special and fascinating phenomena occur when viscoelastic fluids flow in specific geometries [47] and some of them have been known for almost a century, like the Weissenberg (or rod-climbing) effect, in which an extra tension along the flow streamlines forces the fluid to climb a rotating rod put in contact with it, by opposing both the centrifugal and gravitational forces [48, 49]. Other interesting and complex effects arising due to the flow viscoelasticity include the turbulent drag reduction [50], the appearance of large recirculation regions in confined geometries [51] and the elastic turbulence [6, 9].

1.3 Mathematical modelling of viscoelastic fluids

In Section 1.1, we presented a set of equations derived for flow modelling and widely known as Navier-Stokes equation. Although very accurate when representing Newtonian fluid flows, this equation fails in the attempt of reproducing viscoelastic fluid's behaviour. Therefore, the objective of this Section is to present general equations for physical modelling in non-Newtonian Fluid Mechanics. For the ensemble of studies in the present thesis, an isothermal, incompressible, viscoelastic fluid flow is considered. Under these conditions, the set of equations that needs to be solved is the conservation of mass, along with the momentum conservation equation. In standard notation, they write:

$$\begin{cases} \boldsymbol{\nabla} \cdot \boldsymbol{u} = 0 & (1.4) \\ \dfrac{D\boldsymbol{u}}{Dt} = \dfrac{1}{\rho}\boldsymbol{\nabla} \cdot \boldsymbol{\Xi} - \dfrac{1}{\rho}\boldsymbol{\nabla} p + \boldsymbol{\mathcal{F}} & (1.5) \end{cases} ,$$

where the symbol $\boldsymbol{\nabla}()$ is the gradient operator, while $\boldsymbol{\nabla} \cdot ()$ expresses the divergence operator; $\boldsymbol{u}(\boldsymbol{x}, t) = (u(\boldsymbol{x}, t), v(\boldsymbol{x}, t), w(\boldsymbol{x}, t))$ at position $\boldsymbol{x} = (x, y, z)$ and time t represents the velocity field, $\boldsymbol{\Xi}$ is the total (viscous plus elastic) stress tensor, p the pressure, ρ the mass density and $\boldsymbol{\mathcal{F}}$ stands for the body forces.

The special derivative $D\boldsymbol{u}/Dt$ present in Eq. 1.5 is called *material derivative* and is expressed by:

$$\frac{D\boldsymbol{u}}{Dt} = \frac{\partial \boldsymbol{u}}{\partial t} + \boldsymbol{u} \cdot \boldsymbol{\nabla} \boldsymbol{u}. \quad (1.6)$$

In general, the stress tensor $\boldsymbol{\Xi}$ can be thought as composed by a Newtonian viscous solvent component ($\boldsymbol{\sigma}$) and an additional elastic extra-stress component ($\boldsymbol{\tau}$), as $\boldsymbol{\Xi} = \boldsymbol{\sigma} + \boldsymbol{\tau}$. In addition to being a physically intuitive reasoning, it allows to change the mathematical structure thus improving the coupling between the elliptical continuity and momentum equations and the hyperbolic stress equation, for numerical simulation [52]. The Newtonian component of the extra-stress tensor is expressed by:

$$\boldsymbol{\sigma} = \eta_s \dot{\boldsymbol{\gamma}}, \tag{1.7}$$

where η_s is the solvent viscosity and $\dot{\boldsymbol{\gamma}}$ is the rate-of-strain tensor, which is twice the symmetric part of the velocity gradient tensor and is defined as $\dot{\boldsymbol{\gamma}} = \boldsymbol{\nabla u} + \boldsymbol{\nabla u}^T$ [45], with the superscript T denoting the transpose matrix. It is important to remark that the velocity gradient tensor has entries $\nabla u_{ij} = \partial u_j / \partial x_i$, for Cartesian coordinates.

By taking into account the incompressibility of the velocity field in Eq. 1.5 and neglecting external body forces, we can find now an alternative formulation for the momentum conservation equation, as displayed in Eq. 1.8:

$$\rho\left(\frac{\partial \boldsymbol{u}}{\partial t} + \boldsymbol{u} \cdot \boldsymbol{\nabla u}\right) = \boldsymbol{\nabla} \cdot (\eta_s \boldsymbol{\nabla u}) + \boldsymbol{\nabla} \cdot \boldsymbol{\tau} - \boldsymbol{\nabla} p. \tag{1.8}$$

In its turn, the tensor $\boldsymbol{\tau}$ can be described in many different ways, depending on the viscoelastic model chosen. Here, we will adopt and describe three different non-Newtonian models: the *Oldroyd-B* constitutive model (as well as its reduced version, the *upper-convected Maxwell* model) and the more complex FENE models; note, however, that there are many other viscoelastic models that have been extensively studied in the last few decades (*e.g.* the White-Metzner model [53], the PTT [54] and sPTT [55] models and the Giesekus model [56]).

1.3.1 Oldroyd-B constitutive model

Rheological models can approximate polymer molecules through a *dumbbell* model, composed by two beads joined by an elastic connector, in the form of a linear or non-linear spring (see Fig. 1.1). Even though very simplified, these models can accurately describe many rheological properties and largely predict flow dynamics [57]. When a linear (Hookean) spring is considered, an infinite extensibility of polymers follows. This consideration gives rise to fluid models like the Oldroyd-B constitutive equation, which may eventually be simplified into the upper-convected Maxwell (UCM) model [58, 59].

The UCM model represents the simplest rheological constitutive model, which was first obtained from molecular theory in the work of [60]. It accounts for the dynamics of highly concentrated solutions, in which no solvent contribution is considered ($\eta_s = 0$, so the first term on the right-hand side of Eq. 1.8 vanishes). In its turn, the Oldroyd-B

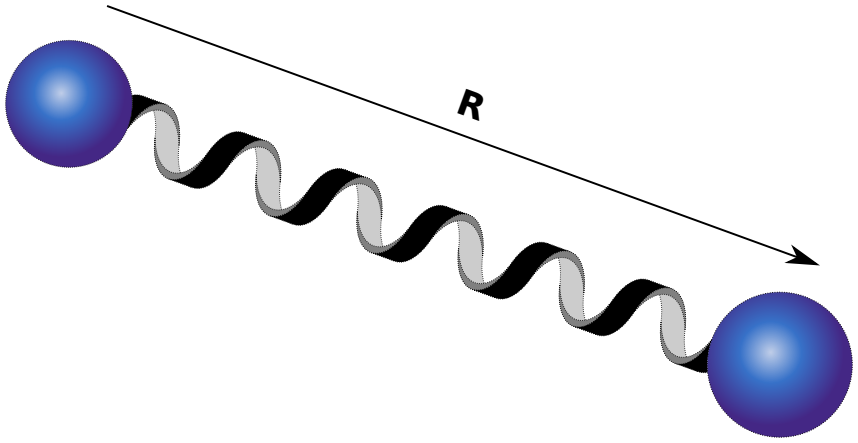

Figure 1.1 – Schematic of an elastic dumbbell model, with two beads (dark blue spheres) joined by a spring. Here, $\boldsymbol{R}$ represents the end-to-end vector (see Eq. 1.10).

model is an extension of UCM fluids and presents a constitutive equation capable of describing the viscoelastic behaviour of non-Newtonian polymeric solutions under general flow conditions. The equation for the polymer extra-stress tensor $\boldsymbol{\tau}$ in the Oldroyd-B and UCM models reads [59]:

$$\boldsymbol{\tau} + \lambda \left[\frac{\partial \boldsymbol{\tau}}{\partial t} + \boldsymbol{\nabla} \cdot (\boldsymbol{u}\boldsymbol{\tau}) - \boldsymbol{\nabla}\boldsymbol{u}^T \cdot \boldsymbol{\tau} - \boldsymbol{\tau} \cdot \boldsymbol{\nabla}\boldsymbol{u} \right] = \eta_p \left(\boldsymbol{\nabla}\boldsymbol{u} + \boldsymbol{\nabla}\boldsymbol{u}^T \right), \tag{1.9}$$

in which λ is the characteristic fluid relaxation time and η_p is the constant polymeric viscosity. We can define here an useful parameter, which will be used throughout this document, the *solvent-to-total viscosity ratio* β. It is expressed as the ratio of the solvent (η_s) to the fluid total ($\eta_t = \eta_s + \eta_p$) viscosity and is inversely proportional to the polymer concentration in a solution. Note that for UCM fluids, $\beta = 0$.

Oldroyd-B corresponds to the simplest differential constitutive equation that is capable of capturing important viscoelastic flow features (*e.g.* the existence of normal stress differences), in a quantitative manner. However, this constitutive model displays well-known deficiencies, such as the absence of shear-dependent viscosity effects and the infinite extensibility of polymers (resulting from the linear elasticity inherent to this model). As a result, it features unbounded steady-state extensional viscosity at, or above a finite strain rate of $\dot{\varepsilon} = 1/2\lambda$ (even if no singularities inside the geometry exist) [57, 61, 62].

1.3.1.1 Conformation tensor formulation

Viscoelastic models can also describe polymer molecules conformation by making use of a second-order, ensemble-averaged configuration tensor named *conformation tensor*, which is, by definition, symmetric positive definite (SPD). This tensor is defined as:

$$\boldsymbol{c} = \frac{\langle \boldsymbol{R}\boldsymbol{R} \rangle}{{R_{eq}}^2}, \tag{1.10}$$

in which $\boldsymbol{R}$ is the end-to-end vector of a polymer molecule (see Fig. 1.1) and the angle brackets $\langle\,\rangle$ indicate an ensemble average (over realisations representing thermal noise). The term ${R_{eq}}^2$ represents the molecule size in the equilibrium state and is defined by the relation $\boldsymbol{R_{eq}} = (3k_B\mathcal{T}/H)^{1/2}\,\boldsymbol{I}$, where k_B, $\mathcal{T}$ and H stand for the Boltzmann constant, the absolute temperature and the dumbbell spring constant, respectively; $\boldsymbol{I}$ represents the identity tensor. The conformation tensor $\boldsymbol{c}$ carries information about an averaged configuration of polymer molecules and its trace $tr(\boldsymbol{c})$ expresses the polymer molecule elongation. It evolves according to the equation:

$$\frac{\partial \boldsymbol{c}}{\partial t} + \boldsymbol{\nabla}\cdot(\boldsymbol{u}\boldsymbol{c}) = \boldsymbol{c}\cdot\boldsymbol{\nabla}\boldsymbol{u} + \boldsymbol{\nabla}\boldsymbol{u}^T\cdot\boldsymbol{c} + \boldsymbol{s}(\boldsymbol{c}). \tag{1.11}$$

In a similar way to that of the tensor $\boldsymbol{\tau}$ in Eq. 1.8, the tensor $\boldsymbol{s}(\boldsymbol{c})$ in Eq. 1.11 takes different forms, depending on the non-Newtonian model assumed. For the Oldroyd-B model, we have:

$$\boldsymbol{s}(\boldsymbol{c}) = \frac{1}{\lambda}(\boldsymbol{I} - \boldsymbol{c}). \tag{1.12}$$

Following this formulation, the extra-stress tensor $\boldsymbol{\tau}$ can be retrieved from the conformation tensor $\boldsymbol{c}$ using the relation:

$$\boldsymbol{\tau} = \frac{\eta_p}{\lambda}(\boldsymbol{c} - \boldsymbol{I}). \tag{1.13}$$

1.3.2 FENE family of constitutive models

We describe here an alternative viscoelastic fluid model, the so-called Finitely Extensible Non-linear Elastic (FENE) dumbbell model, which is actually an extensive class of models. The FENE family of models was developed for kinetic theory calculations [63] and greatly detailed in the work of Bird et al. [57]. In FENE models, a non-linear and only finitely extensible spring is employed for the connection between beads in the dumbbell model, which is more physically realistic (compared to linearly elastic models). Consequently, they can reproduce additional fluid flow behaviours thus providing improved prediction of material functions.

Nonetheless, in order to be translated into an equivalent macroscopic constitutive equation, FENE models need a *closure* approximation. Among the different closures proposed in the literature [64–70], we adopt the classical *Peterlin closure* [64, 71], which corresponds to:

$$\boldsymbol{s}(\boldsymbol{c}) = \frac{1}{\lambda}\left(\boldsymbol{I} - f(tr(\boldsymbol{c}))\cdot\boldsymbol{c}\right), \tag{1.14}$$

in which $f(tr(\boldsymbol{c}))$ is a pre-averaging approximation to the dumbbell spring force law, called *Peterlin function* and defined as:

$$f(tr(\boldsymbol{c})) = \frac{1}{1 - \dfrac{tr(\boldsymbol{c})}{L^2}}, \tag{1.15}$$

where $tr()$ stands for the trace operation, $\boldsymbol{c}$ is the polymer conformation tensor and the parameter L^2 is proportional to the square of the maximum stretch of the polymer molecules, with respect to the equilibrium distance.

A typical extensibility value of $L^2 = 100$ has often been adopted in literature works (*e.g.* [68, 71, 72]), but quite different values also appear (for instance, Xi and Graham [73] choose $L^2 = 1000$, which is typical of high molecular weight polymers). Constitutive models that feature unbounded polymer stretch – like the UCM and Oldroyd-B models – correspond to the limiting case $L^2 \to \infty$.

The relation between extra-stress tensor $\boldsymbol{\tau}$ and the conformation tensor $\boldsymbol{c}$ for the FENE-P model is given in Eq. 1.16,

$$\boldsymbol{\tau} = \frac{\eta_p}{\lambda}\left(f(tr(\boldsymbol{c}))\cdot\boldsymbol{c} - \boldsymbol{I}\right). \tag{1.16}$$

Several closures for the FENE family have alternatively been proposed, like the constant-viscosity FENE-CR constitutive model [65], the more theoretically accurate FENE-L model [66] (capable of reproducing hysteretic behaviours, as opposed to FENE-P model) and its simplified version, the FENE-LS model [67].

1.3.3 Dimensionless parameters

The equations displayed in Section 1.1 can be made non-dimensional, so they can allow scaling to real flow conditions. We accomplish that by employing appropriate normalisations for all dimensional variables using some reference quantities, which will depend on the study performed. This process will give rise to a set of non-dimensional quantities that can be useful for assessing the relative importance of the various terms present in the physical equations.

1.3.3.1 Reynolds number (Re)

Probably the most widely known dimensionless parameter in fluid mechanics, the *Reynolds number* (Re) quantifies the relative importance of the inertial forces acting on a given fluid flow, compared to the internal viscous forces. The Reynolds number is defined as:

$$Re = \frac{\rho U_c L_c}{\mu} \tag{1.17}$$

in which U_c and L_c are flow characteristic velocity and length scales, respectively. When the Reynolds number is specially large – the sense of *large* depending on the geometry – the characteristic behaviour of the system tends to be turbulent and many degrees of freedom are excited, creating irregular patterns in the flow velocity [74].

1.3.3.2 Deborah number (De)

The *Deborah number* (De) was formally defined by Reiner [75] as being the ratio of the fluid relaxation time λ to the characteristic time scale of observation. The Deborah number discriminates how a material will behave in a given period of time, considering that this material is experiencing a physical deformation over this time frame. The greater the Deborah number, the more *solid-like* the material behaves; similarly, the smaller the Deborah number, the more *Newtonian-like* it will appear [75]. The definition for Deborah number is:

$$De = \frac{\lambda}{t_c} = \frac{\lambda U_c}{L_c} \tag{1.18}$$

where t_c represents the characteristic observation time, $t_c = L_c/U_c$.

1.3.3.3 Weissenberg number (Wi)

Alternatively, the *Weissenberg number* (Wi) has been defined as the ratio of elastic to viscous forces in the flow and is a fundamental dimensionless quantity in non-Newtonian fluid dynamics [76, 77]. Dealy [78] states that the Weissenberg number represents the degree of non-linearity in the rheological response of a fluid flow, being written as:

$$Wi = \dot{\gamma}\lambda \tag{1.19}$$

where $\dot{\gamma}$ stands for the shear rate applied to the fluid.

A relevant property which is worth-noting is that in geometries where one single length scale determines the dynamics of the problem, the definitions for Deborah and Weissenberg numbers will coincide [77].

1.4 Challenges in fluid numerical computation: The high Weissenberg number problem

Computational fluid dynamics (CFD) emerged as a powerful complementary method to the problem exposed in the last paragraph of Section 1.1. By employing discretisation tools, one can approximate the equations by a system of algebraic equations, which can then be solved in a much simpler way. Although being an effective approach to deal with complex fluid flows, some issues appear when solving partial differential equations numerically, regarding convergence, accuracy, stability and consistency of the numerical scheme [79]. This issue can become even more important when dealing with viscoelastic flows. In the last few decades, the constitutive equations that describe the behaviour of viscoelastic fluids have been subject of extensive discussion and improvement [80] and even a comprehensive review on current challenges in computational rheology was produced by Walters and Webster [81].

Existing models of viscoelastic fluids present challenging problems for numerical computation, among which the most outstanding obstacle to provide solutions for complex flows beyond some critical elasticity level is the high Weissenberg number problem [29, 30]. This problem manifests as a breakdown of the numerical scheme caused by the loss of positive-definiteness of the conformation tensor when calculating the evolution of the viscoelastic extra-stress tensor directly [31] and has been one of the biggest barriers from stably simulating viscoelastic fluid flows, even in simple geometries, since its discovery in the late 1970's [82].

Numerical simulations of viscoelastic fluid flows, when performed above a certain elasticity level, generally face non-physical instabilities, known as *Hadamard instabilities* [83], in which a sharp growth of short-wave disturbances leads to the loss of the positive-definiteness of the conformation tensor [31, 84, 85]. Still back in the 1980's, the close relationship between the change of type (elliptic, hyperbolic or parabolic) and the loss of the evolutionary character of the system of flow equations started to be investigated [86].

Joseph and Saut [87] remarked that a set of conservation and constitutive equations of the hyperbolic type is more prone to generate this kind of disruption in numerical simulations. Based upon this knowledge, Hulsen [88] reported a sufficient condition to be respected in order to keep the polymer stress tensor positive definite, which in its turn guarantees that the system of equations is mathematically well-posed and thus provides the necessary requirements for stable solutions of viscoelastic fluid flows at elasticity levels of practical interest [89]. Posteriorly, Kwon and Leonov [90] proposed strong stability criteria in the formulation of integral and differential constitutive models, with regard to Hadamard instabilities.

1.4.1 The employment of artificial stress diffusivity

In this context, several miscellaneous attempts were made to improve numerical stability when solving the constitutive equations of viscoelastic fluid models, by better controlling the high Weissenberg number problem. In the mid 1990's, Sureshkumar and Beris [32] firstly proposed the addition of an artificially large global stress diffusion term into the numerical problem in an attempt to surmount the stability issues. The authors reported that for large Reynolds number channel flows of an Oldroyd-B model, the addition of artificial stress diffusion can significantly improve numerical stability without bringing qualitative discrepancies into the flow dynamics.

This clever and extensively used solution has in fact a mathematical meaning. For solutions to exist at arbitrary levels of elasticity, El-Kareh and Leal [91] proved that a given realistic constitutive model must include some quantity of polymer-stress diffusion. Still, a challenging problem that emerges is that this diffusivity term brought into the equation must be adjusted to be as small as possible, since the amount of diffusivity needed to attain numerical stability is usually three to six orders of magnitude greater than that suitable for physical polymer solutions [57, 92]. By performing numerical studies on a two-dimensional flow driven by simple background forcing, Thomases [93] showed that the artificial stress diffusivity keeps the conformation tensor (and hence the polymer stress tensor) bounded and smooth and that this holds true for both the Oldroyd-B and the FENE-P constitutive models. Furthermore, numerical studies on turbulent FENE-P and Giesekus fluid flows with artificial stress diffusion reported a qualitative agreement between numerics and experiments [94, 95].

However, the employment of this artificial method was recently found to have a dramatic effect on the qualitative spatial and temporal dynamics of two-dimensional cellular flows, including the formation of some spurious large-scale phenomena (like the symmetry-breaking in the vorticity field) which are not present when no artificial diffusivity is used (see Fig. 1.2) [34]. The impact of this method can be remarkable for some flow settings, particularly in flows characterised by regions of pure strain. However, the effects of such strategy may reveal less pronounced for other flow conditions, *e.g.* high Reynolds numbers flows and in setups that mix strain and vorticity, like the simulation of elastic turbulence in two-dimensional (2D) periodic Kolmogorov flows [96, 97]. In conclusion, as pointed out by Gupta and Vincenzi [34], "[...] great caution should be taken in using artificial diffusivity to prevent numerical instabilities in simulations of elastic turbulence".

1.4.2 Alternative methods

Because of the physical inaccuracy inherent to the numerical method presented in Subsection 1.4.1, many alternative possibilities were proposed to alleviate the HWNP,

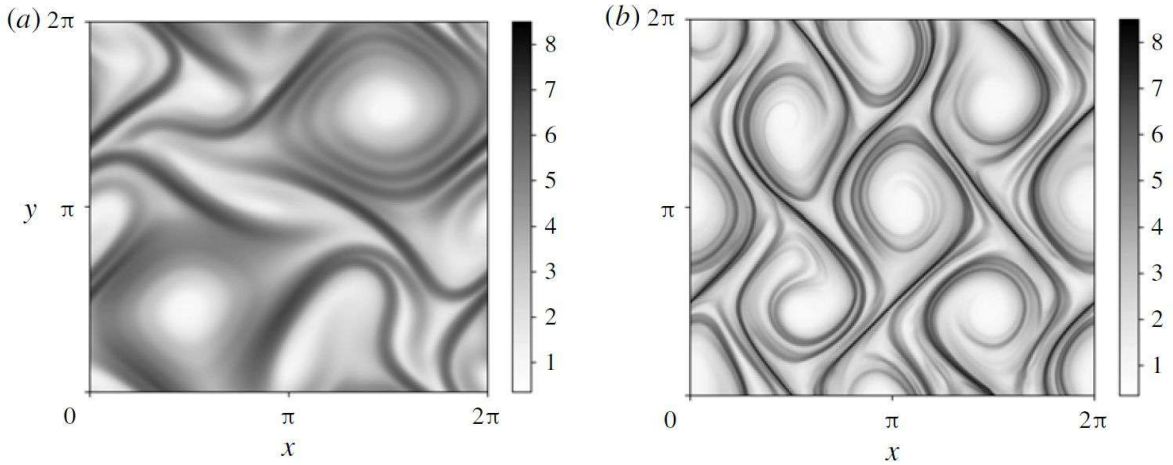

(a) $\kappa = 5 \times 10^{-5}$ (b) $\kappa = 0$

Figure 1.2 – Snapshots of $\ln(tr(\boldsymbol{c}))$ taken at the same times for simulations of a two-dimensional cellular flow with (left panel) and without (right panel) artificial diffusion included, evidencing a substantial qualitative difference in the behaviour of the polymer stresses. Here, κ is the coefficient of diffusivity, which was set to $\kappa = 5 \times 10^{-5}$ in the viscoelastic flows with artificial diffusion (extracted from [34]).

e.g. the less intrusive method of *locally added artificial diffusion*, by which artificial diffusion is inserted only at critical locations, where the conformation tensor's positive-definiteness constraint was being infringed [33].

Nonetheless, the first known method that considered the change of mathematical type of the constitutive equations was proposed by King et al. [98] and named Explicitly Elliptic Momentum Equation (EEME) formulation. This methodology restructures the momentum balance equation by making more explicit the elliptic character of the mathematical equation and it allowed to obtain numerically stable and accurate solutions for different two-dimensional UCM fluid flows. Following that, Rajagopalan et al. [52] introduced the Elastic-Viscous Split Stress (EVSS) formulation, an alternative numerical scheme which splits the elastic and the viscous components of the polymer stress tensor, in a procedure previously introduced by Mendelson et al. [99]. Some years later, Sun et al. [100] presented results for a modified version of the viscoelastic stress splitting scheme which allows the Newtonian component of the extra-stress tensor to depend on the magnitude of the local elastic stresses. This novel formulation was called Adaptive Viscoelastic Stress Splitting (AVSS) scheme and performed very well for higher Weissenberg values of viscoelastic flows. The merits of this set of methodologies to stabilise the numerical computation of non-Newtonian flows compared to the addition of an artificial stress diffusion term have been systematically studied later on, for Oldroyd-B fluid flows, by Amoreira and Oliveira [101].

Following to the AVSS scheme, other remarkable methodologies have been introduced, in which some kind of decomposition or factorisation of the conformation

tensor is taken in account; in 2004, Fattal and Kupferman [35] firstly proposed a *logarithmic decomposition* of the conformation tensor (whose details are reported in Subsection 4.2.1 of the present document) and some years later, Balci et al. [102] proved that a unique *square-root factorisation* can also be obtained in order to guarantee the positive-definiteness of the conformation tensor (see Section 2.3 for a deep analysis on this technique). Moreover, Afonso et al. [103] reported a generic decomposition of the conformation tensor (from which both the log-conformation representation and the square-root method can be retrieved) that was called *kernel-conformation* tensor transformation. Many other alternative techniques to ensure the positive-definiteness of the polymer stress tensor followed, based on the pioneering strategy of the LCR with varied modifications [104–108].

All these promising methods have been applied to a variety of flow conditions featuring (very) low Reynolds and high Weissenberg numbers in two and three-dimensional cases [109–114], where their performance and effectiveness in stabilising numerical simulations of turbulent flows was assessed and compared. Despite the indisputable progress observed over the last few decades, computing stable and accurate numerical flow solutions at arbitrarily high elasticity levels remains a non-trivial and so far unreached task. It is generally acknowledged that much research is yet to be carried out in this direction.

Chapter 2

Stabilisation methods

2.1 The Gilcart solver and stability issues

In the present Chapter, an extensive analysis is presented for flow simulations performed by means of an in-house numerical flow solver, named Gilcart. The Gilcart code is a finite-volume algorithm written in Fortran language and developed by Mompean [115], that allows the simulation of three-dimensional flows of Newtonian and non-Newtonian fluids, in rectilinear Cartesian coordinates [116]. Although very powerful and robust in performing simulations even of highly turbulent Newtonian flows, this software lacks stability for progressively increased levels of elasticity in viscoelastic flows. The main goal of the study reported here is hence to provide conclusions on whether the sole implementation of the square-root stabilising tool, introduced in Subsection 1.4.2, is capable of improving the solver's overall numerical stability on varied flow conditions, taking into account the ambitious objective of making it suitable for stably achieving the levels of elasticity needed when simulating flows undergoing purely elastic instabilities (and elastic turbulence). Potential limitations of this formulation are also discussed.

In a first moment, a deep scrutiny of the numerical methods behind the *original* solver formulation is introduced (*original* will hereafter denote the algorithm formulation devoid of the stabilising technique) and afterwards, some relevant modifications are described: the alternative formulation presented in Subsection 1.3.1 (conformation tensor) and the square-root factorisation method that have been implemented in the numerical code. After the process of implementing the square-root factorisation introduced by Balci et al. [102], numerical simulations of Oldroyd-B fluid flows in a channel geometry were performed for validation and benchmark purposes.

2.2 Numerical methods of the GILCART solver

GILCART's numerical method is based upon a finite-volume technique, with a second-order discretisation in space and explicit first-order discretisation in time using Euler's method. This Section provides a brief review on the methods used to discretise the mathematical equations (in both space and time), whereas a full documentation of this code's formulation is presented in the work of Mompean and Deville [116].

2.2.1 Spatial discretisation

The physical equations presented in Section 1.3 are integrated over a staggered control volume (CV), in order to reduce instabilities in systems containing geometrical singularities [117]. A representation of a finite-volume cell is displayed in Fig. 2.1. The pressure (p) and the normal extra-stress tensor components (shown here as τ_{xx}, τ_{yy} and τ_{zz}) are evaluated at the centre of the CV; the components of the velocity field (u, v and w) are calculated at the centre of the faces and finally, the remaining components of the extra-stress tensor (τ_{xy}, τ_{xz} and τ_{yz}) are considered at the mid-edges.

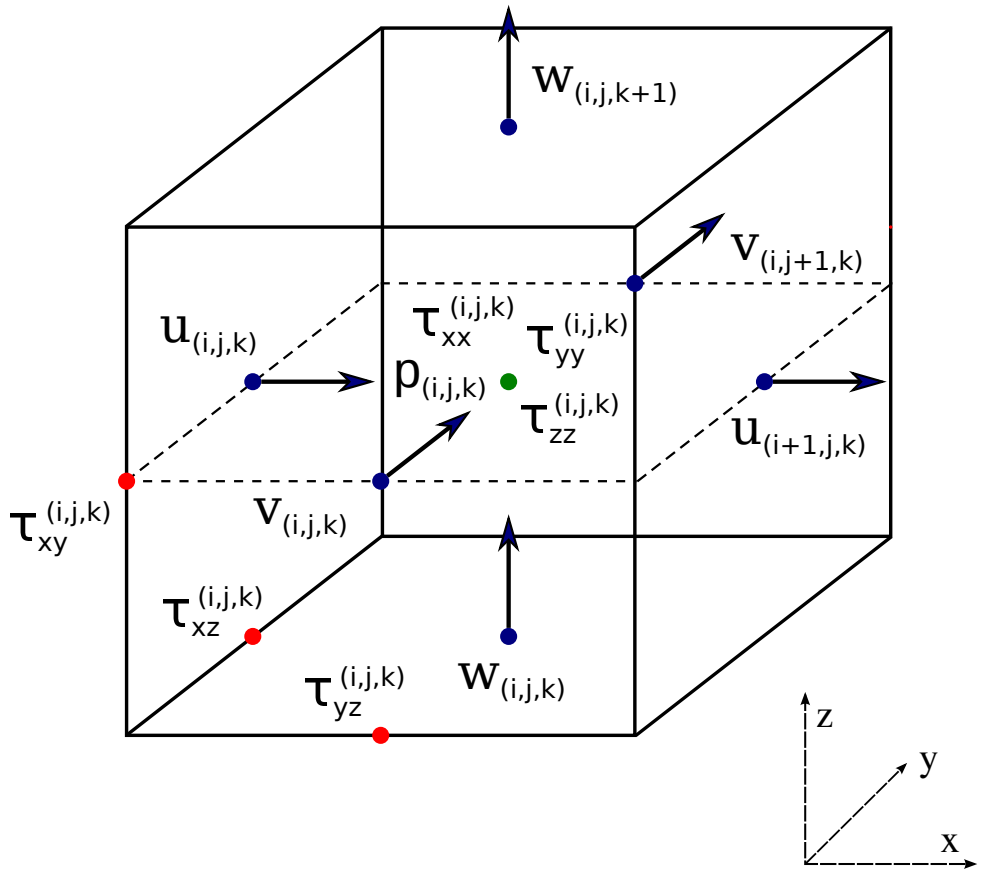

Figure 2.1 – Control volume with the position of all variables (pressure, velocity and stress components). Blue dots with arrows indicate components of a vector quantity (on face centres), red dots represent mid-edges and the green dot is the CV centre.

We perform an integration of the equations of conservation of mass and momentum over this CV and then, all resulting volume integrals are transformed into surface integrals using the divergence (or Gauss) theorem,

$$\int_V \boldsymbol{\nabla} \cdot \boldsymbol{F}\, dV = \oint_S \boldsymbol{F} \cdot \boldsymbol{n}\, dS\,, \tag{2.1}$$

where $\boldsymbol{F}$ is any continuously differentiable vector field, V represents a volume in three-dimensional (3D) space with smooth boundary S and $\boldsymbol{n}$ is the outward pointing, unitary, normal vector field of the boundary S. For instance, the divergence theorem applied to the continuity equation (Eq. 1.4) in three dimensions gives:

$$\left(u_{i+1,j,k} - u_{i,j,k}\right)\Delta y_j \Delta z_k + \left(v_{i,j+1,k} - v_{i,j,k}\right)\Delta x_i \Delta z_k + \left(w_{i,j,k+1} - w_{i,j,k}\right)\Delta x_i \Delta y_j = 0\,, \tag{2.2}$$

in which Δx_i, Δy_j and Δz_k represent the distances between two neighbour mesh nodes (of indices i and $i+1$ for x, j and $j+1$ for y, and k and $k+1$ for z), concerning the velocity components u, v and w, respectively.

2.2.1.1 Discretisation of diffusive terms

Considering both the momentum conservation (Eq. 1.8) and the Oldroyd-B constitutive equation (Eq. 1.9), the linear diffusive terms are discretised by a second-order accuracy, centred difference scheme. In order to discretise the diffusive flux term in Eq. 1.8, we use at first the divergence theorem,

$$\int_V \boldsymbol{\nabla} \cdot \left(\eta_s \boldsymbol{\nabla} u_\varphi\right) dV = \eta_s \oint_S \frac{\partial u_\varphi}{\partial \gamma} \cdot \boldsymbol{n}_{\boldsymbol{\gamma}}\, dS\,, \tag{2.3}$$

where u_φ is the velocity component in the $\varphi-$direction and $\boldsymbol{n}_{\boldsymbol{\gamma}}$ is the unitary vector in the $\gamma-$direction. Note that repeated indices indicate a summation.

The derivative $\partial u_\varphi / \partial \gamma$ for *e.g.* the u velocity component with respect to the $x-$coordinate, is discretised as follows:

$$\frac{\partial u}{\partial x} \simeq \frac{u_{i+1,j,k} - u_{i-1,j,k}}{2\,\Delta x_i} + \mathcal{O}\left({\Delta x_i}^2\right). \tag{2.4}$$

The discretisation process for the other spatial coordinates, velocity components and diffusive terms proceeds in an equivalent manner.

2.2.1.2 Discretisation of advective terms

The non-linear terms can be evaluated either by a simple upwind differencing scheme (UDS) or by applying the more complex QUICK scheme (QUICK being the acronym for **Q**uadratic **U**pstream **I**nterpolation Scheme for the **C**onvective **K**inematics). While the

UDS is the most stable among the existing discretisation methods for advection [118], it only offers first order of accuracy, not suitable in many cases. The QUICK method for advective modelling, proposed by Leonard [119] is an alternative, higher-order accuracy, scheme. We describe next the details for both discretisation methods inside the algorithm.

Upwind differencing scheme (UDS) In the same way we did for the diffusive terms, the divergence theorem is used to discretise the advective flux term in Eq. 1.8,

$$\int_V \boldsymbol{\nabla} \cdot (\rho \boldsymbol{u}\boldsymbol{u})\, dV = \rho \oint_S \boldsymbol{u}\boldsymbol{u} \cdot \boldsymbol{n}\, dS\,. \tag{2.5}$$

Then, we can discretise the integral on the right-hand side of Eq. 2.5,

$$\oint_S \boldsymbol{u}\boldsymbol{u} \cdot \boldsymbol{n}\, dS \simeq \sum_i A_{in}\, u_{in}\, (\boldsymbol{u} \cdot \boldsymbol{n})_{in} - \sum_j A_{out}\, u_{out}\, (\boldsymbol{u} \cdot \boldsymbol{n})_{out}\,, \tag{2.6}$$

where A_{in} and A_{out} represent the surface area of each pair of opposite faces of the control volume, and u_{in} and u_{out} are the interpolated mean velocities in each direction, respectively entering and exiting the CV, as follows:

$$A_{in} = A_{out} = \begin{cases} \Delta y_j \Delta z_k & \text{in } x\text{–direction} \\ \Delta x_i \Delta z_k & \text{in } y\text{–direction} \\ \Delta x_i \Delta y_j & \text{in } z\text{–direction} \end{cases}, \tag{2.7}$$

$$u_{in} = \begin{cases} \frac{1}{2}\left(u_{i+1,j,k} + u_{i,j,k}\right) & \text{in } x\text{–direction} \\ \frac{1}{2}\left(v_{i-1,j+1,k} + v_{i,j+1,k}\right) & \text{in } y\text{–direction} \\ \frac{1}{2}\left(w_{i-1,j,k+1} + w_{i,j,k+1}\right) & \text{in } z\text{–direction} \end{cases}, \tag{2.8}$$

$$u_{out} = \begin{cases} \frac{1}{2}\left(u_{i-1,j,k} + u_{i,j,k}\right) & \text{in } x\text{–direction} \\ \frac{1}{2}\left(v_{i-1,j,k} + v_{i,j,k}\right) & \text{in } y\text{–direction} \\ \frac{1}{2}\left(w_{i-1,j,k} + w_{i,j,k}\right) & \text{in } z\text{–direction} \end{cases}. \tag{2.9}$$

So, the complete equation writes:

$$\begin{aligned}\oint_S \boldsymbol{u}\boldsymbol{u}\cdot\boldsymbol{n}\,dS \simeq &\left[\frac{1}{2}\left(u_{i+1,j,k}+u_{i,j,k}\right)\cdot u_{i+1/2}-\frac{1}{2}\left(u_{i-1,j,k}+u_{i,j,k}\right)\cdot u_{i-1/2}\right]\Delta y_j\Delta z_k\\ &+\left[\frac{1}{2}\left(v_{i-1,j+1,k}+v_{i,j+1,k}\right)\cdot u_{j+1/2}-\frac{1}{2}\left(v_{i-1,j,k}+v_{i,j,k}\right)\cdot u_{j-1/2}\right]\Delta x_i\Delta z_k\\ &+\left[\frac{1}{2}\left(w_{i-1,j,k+1}+w_{i,j,k+1}\right)\cdot u_{k+1/2}-\frac{1}{2}\left(w_{i-1,j,k}+w_{i,j,k}\right)\cdot u_{k-1/2}\right]\Delta x_i\Delta y_j\end{aligned}, \quad (2.10)$$

where the terms $u_{i+1/2}$, $u_{j+1/2}$ and $u_{k+1/2}$ are evaluated following the UDS as:

$$u_{i+1/2}=\begin{cases}u_{i,j,k} & \text{if } \frac{1}{2}\left(u_{i+1,j,k}+u_{i,j,k}\right)>0\\ u_{i+1,j,k} & \text{if } \frac{1}{2}\left(u_{i+1,j,k}+u_{i,j,k}\right)<0\end{cases}, \quad (2.11)$$

$$u_{j+1/2}=\begin{cases}u_{i,j,k} & \text{if } \frac{1}{2}\left(v_{i-1,j+1,k}+v_{i,j+1,k}\right)>0\\ u_{i,j+1,k} & \text{if } \frac{1}{2}\left(v_{i-1,j+1,k}+v_{i,j+1,k}\right)<0\end{cases}, \quad (2.12)$$

$$u_{k+1/2}=\begin{cases}u_{i,j,k} & \text{if } \frac{1}{2}\left(w_{i-1,j,k+1}+w_{i,j,k+1}\right)>0\\ u_{i,j,k+1} & \text{if } \frac{1}{2}\left(w_{i-1,j,k+1}+w_{i,j,k+1}\right)<0\end{cases}. \quad (2.13)$$

The terms $u_{i-1/2}$, $u_{j-1/2}$ and $u_{k-1/2}$ are calculated analogously.

QUICK scheme The QUICK scheme provides an improvement in the accuracy offered by the first-order UDS, exhibiting a third-order accuracy for a regularly spaced grid. A more detailed description of this method can be found in the work of Leonard [119]. With respect to the UDS, this method provides a more accurate calculation for the interpolated values of the terms $(\boldsymbol{u}\cdot\boldsymbol{n})_{in}$ and $(\boldsymbol{u}\cdot\boldsymbol{n})_{out}$ in Eq. 2.6, replacing Eqs. 2.11, 2.12 and 2.13 by:

$$u_{i+1/2}=\frac{1}{2}\left(u_{i,j,k}+u_{i+1,j,k}\right)+\frac{{\Delta x_i}^2}{8\,\Delta l_{\xi-1}}\left(\frac{u_{\xi+1,j,k}-u_{\xi,j,k}}{\Delta x_\xi}-\frac{u_{\xi,j,k}-u_{\xi-1,j,k}}{\Delta x_{\xi-1}}\right), \quad (2.14)$$

where:

$$\xi=\begin{cases}i & \text{if } \frac{1}{2}\left(u_{i,j,k}+u_{i-1,j,k}\right)\geq 0\\ i+1 & \text{if } \frac{1}{2}\left(u_{i,j,k}+u_{i-1,j,k}\right)<0\end{cases}. \quad (2.15)$$

Once again, the terms regarding the remaining spatial coordinates are calculated similarly to Eqs. 2.14 and 2.15.

2.2.2 Temporal discretisation

The solution for the discretised equations derived here is obtained by a time-marching algorithm, which follows a first-order explicit Euler scheme. Expressing the continuity equation at a specific time step – which will be defined as $n+1$ – we obtain:

$$\boldsymbol{\nabla} \cdot \boldsymbol{u}^{(n+1)} = 0. \tag{2.16}$$

From Eq. 1.8, we can also get the momentum equation discretised in time, which states that every term on it will be evaluated at the previous time (n), except for the pressure gradient, which will be calculated at the new time $(n+1)$ for each iteration,

$$\frac{\boldsymbol{u}^{(n+1)} - \boldsymbol{u}^{(n)}}{\Delta t} + \boldsymbol{u}^{(n)} \cdot \boldsymbol{\nabla} \boldsymbol{u}^{(n)} = \frac{1}{\rho}\left[\boldsymbol{\nabla} \cdot \left(\eta_s \boldsymbol{\nabla} \boldsymbol{u}^{(n)} + \boldsymbol{\tau}^{(n)}\right) - \boldsymbol{\nabla} p^{(n+1)}\right]. \tag{2.17}$$

We can thus rewrite this equation in a simpler way, grouping the terms to be considered in the same time step:

$$\boldsymbol{u}^{(n+1)} = \Delta t \left[\boldsymbol{S}(\boldsymbol{u})^{(n)} - \frac{1}{\rho}\boldsymbol{\nabla} p^{(n+1)}\right], \tag{2.18}$$

where $\boldsymbol{S}(\boldsymbol{u})$ is the explicit part – *i.e.* evaluated at time (n) – of Eq. 2.17 and contains both the advective and diffusive terms,

$$\boldsymbol{S}(\boldsymbol{u}) = \frac{\boldsymbol{u}}{\Delta t} + \boldsymbol{\nabla} \cdot \left(\nu_0 \boldsymbol{\nabla} \boldsymbol{u} + \frac{1}{\rho}\boldsymbol{\tau} - \boldsymbol{u}\boldsymbol{u}\right), \tag{2.19}$$

where $\nu_0 = \eta_s/\rho$ is the kinematic viscosity of the solvent and the last term $(\boldsymbol{u}\boldsymbol{u})$ indicates a tensor product.

The equations for the six different components of the viscoelastic extra-stress tensor $\boldsymbol{\tau}$ are also discretised in time using the first-order explicit Euler scheme, applied to Eq. 1.9, in the following fashion:

$$\boldsymbol{\tau}^{(n+1)} = \boldsymbol{\tau}^{(n)} + \Delta t \left[\frac{\eta_p \dot{\boldsymbol{\gamma}} - \boldsymbol{\tau}}{\lambda} - \boldsymbol{\nabla} \cdot (\boldsymbol{u}\boldsymbol{\tau}) + \boldsymbol{\nabla} \boldsymbol{u}^T \cdot \boldsymbol{\tau} + \boldsymbol{\tau} \cdot \boldsymbol{\nabla} \boldsymbol{u}\right]^{(n)}. \tag{2.20}$$

2.2.2.1 Time-step evaluation

In order to calculate the maximum time step for the non-linear advection, the *Courant-Friedrichs-Lewy* (CFL) stability condition [120] is adopted, which gives:

$$\Delta t_a = \frac{1}{\max\left\{\dfrac{|u|}{\Delta x} + \dfrac{|v|}{\Delta y} + \dfrac{|w|}{\Delta z}\right\}}. \tag{2.21}$$

For the diffusion time step, the adopted limit is given by Patankar [121]:

$$\Delta t_d = \frac{1}{3\,\nu_0 \max\left\{\dfrac{1}{(\Delta x)^2} + \dfrac{1}{(\Delta y)^2} + \dfrac{1}{(\Delta z)^2}\right\}}. \tag{2.22}$$

The global maximum time step for the numerical simulation is then calculated as being half of the harmonic mean of both advection and diffusion time steps [79]:

$$\Delta t = \frac{1}{\dfrac{1}{\Delta t_a} + \dfrac{1}{\Delta t_d}}. \tag{2.23}$$

When performing non-Newtonian fluid flow simulations, an extra time step restriction must be considered: the global time step determined by Eq. 2.23 cannot be greater than the polymeric time scale of the problem, expressed by the fluid relaxation time λ, so the minimum value between Eq. 2.23 and λ is taken. Further, for good accuracy in time, Δt should be considerably smaller than λ [122].

2.2.2.2 Velocity-pressure coupling

The procedure for obtaining the pressure in each node is based upon the mass conservation requirement, by decoupling the velocity and pressure variables based on the SOLA method [123], a numerical solution algorithm for transient fluid flows, which was designed as a simplified version of the notable *Marker-and-Cell* (MAC) technique [124–126]. Firstly, we write the discretised form of Eq. 2.18,

$$u_\varphi^{(n+1)} = \Delta t \left[S_\varphi(\boldsymbol{u})^{(n)} - \frac{1}{\rho}\frac{\partial p}{\partial \varphi}^{(n+1)} \right], \tag{2.24}$$

where u_φ and S_φ are the components of $\boldsymbol{u}$ and $\boldsymbol{S}(\boldsymbol{u})$, respectively, in the φ–direction.

The gradient of the pressure field is evaluated, for each component, using a first-order finite-difference scheme,

$$\begin{cases} \dfrac{1}{\rho}\dfrac{\partial p}{\partial x} = \dfrac{p_{i,j,k} - p_{i-1,j,k}}{\Delta x_{i-1/2}} & \text{in } x\text{–direction} \\ \dfrac{1}{\rho}\dfrac{\partial p}{\partial y} = \dfrac{p_{i,j,k} - p_{i,j-1,k}}{\Delta y_{i-1/2}} & \text{in } y\text{–direction} \\ \dfrac{1}{\rho}\dfrac{\partial p}{\partial z} = \dfrac{p_{i,j,k} - p_{i,j,k-1}}{\Delta z_{i-1/2}} & \text{in } z\text{–direction} \end{cases}, \tag{2.25}$$

where the mass density ρ is incorporated to the new pressure variable p. To apply mass conservation, we replace Eq. 2.24 into the discretised mass conservation equation displayed in Eq. 2.2, using Eq. 2.25 for the pressure terms:

$$\begin{aligned}
&\Delta y_j \Delta z_k \Delta t \left\{ \left[S(u)^{(n)}_{i+1,j,k} - \frac{p^{(n+1)}_{i+1,j,k} - p^{(n+1)}_{i,j,k}}{\Delta x_{i+1/2}} \right] - \left[S(u)^{(n)}_{i,j,k} - \frac{p^{(n+1)}_{i,j,k} - p^{(n+1)}_{i-1,j,k}}{\Delta x_{i-1/2}} \right] \right\} + \\
&\Delta x_i \Delta z_k \Delta t \left\{ \left[S(v)^{(n)}_{i,j+1,k} - \frac{p^{(n+1)}_{i,j+1,k} - p^{(n+1)}_{i,j,k}}{\Delta y_{j+1/2}} \right] - \left[S(v)^{(n)}_{i,j,k} - \frac{p^{(n+1)}_{i,j,k} - p^{(n+1)}_{i,j-1,k}}{\Delta y_{j-1/2}} \right] \right\} + \quad . \qquad (2.26) \\
&\Delta x_i \Delta y_j \Delta t \left\{ \left[S(w)^{(n)}_{i,j,k+1} - \frac{p^{(n+1)}_{i,j,k+1} - p^{(n+1)}_{i,j,k}}{\Delta z_{k+1/2}} \right] - \left[S(w)^{(n)}_{i,j,k} - \frac{p^{(n+1)}_{i,j,k} - p^{(n+1)}_{i,j,k-1}}{\Delta z_{k-1/2}} \right] \right\} = 0
\end{aligned}$$

By rearranging Eq. 2.26, we can obtain the final form of the equation for the pressure nodes:

$$\begin{aligned}
&AW_{i,j,k} \cdot p^{(n+1)}_{i-1,j,k} + AE_{i,j,k} \cdot p^{(n+1)}_{i+1,j,k} + AS_{i,j,k} \cdot p^{(n+1)}_{i,j-1,k} + AN_{i,j,k} \cdot p^{(n+1)}_{i,j+1,k} \\
&+ AB_{i,j,k} \cdot p^{(n+1)}_{i,j,k-1} + AT_{i,j,k} \cdot p^{(n+1)}_{i,j,k+1} - A_{i,j,k} \cdot p^{(n+1)}_{i,j,k} = B^{(n)}_{i,j,k}
\end{aligned}, \qquad (2.27)$$

where:

$$\begin{aligned}
AW_{i,j,k} &= \frac{\Delta y_j \Delta z_k}{\Delta x_{i-1/2}} & AE_{i,j,k} &= \frac{\Delta y_j \Delta z_k}{\Delta x_{i+1/2}} \\
AS_{i,j,k} &= \frac{\Delta x_i \Delta z_k}{\Delta y_{j-1/2}} & AN_{i,j,k} &= \frac{\Delta x_i \Delta z_k}{\Delta y_{j+1/2}}. \qquad (2.28) \\
AB_{i,j,k} &= \frac{\Delta x_i \Delta y_j}{\Delta z_{k-1/2}} & AT_{i,j,k} &= \frac{\Delta x_i \Delta y_j}{\Delta z_{k+1/2}}
\end{aligned}$$

$$A_{i,j,k} = AW_{i,j,k} + AE_{i,j,k} + AS_{i,j,k} + AN_{i,j,k} + AB_{i,j,k} + AT_{i,j,k}. \qquad (2.29)$$

$$\begin{aligned}
B^{(n)}_{i,j,k} = \Delta y_j \Delta z_k \left[S(u)^{(n)}_{i+1,j,k} - S(u)^{(n)}_{i,j,k} \right] + \Delta x_i \Delta z_k \left[S(v)^{(n)}_{i,j+1,k} - S(v)^{(n)}_{i,j,k} \right] \\
+ \Delta x_i \Delta y_j \left[S(w)^{(n)}_{i,j,k+1} - S(w)^{(n)}_{i,j,k} \right].
\end{aligned} \qquad (2.30)$$

Summarising, we have to solve the following linear system, in order to determine the pressure field:

$$\boldsymbol{A}\, p^{(n+1)} = \boldsymbol{B}^{(n)}. \qquad (2.31)$$

The Gilcart solver presents two different methods for solving the above linear equations system: the direct *Cholesky decomposition* method – which has a prohibitive memory cost for highly refined meshes – and the iterative *conjugate gradient method*, which is based on a minimisation procedure. A step-by-step algorithm detailing each iteration of the time-marching Gilcart solver can be found in Appendix A.

2.3 Numerical implementation of stabilising tools

Preliminary simulations with the original solver suggested that stability issues related to the HWNP were strongly affecting our results, which motivated us to proceed to the implementation of the square-root factorisation of the conformation tensor. This operation required the pre-implementation of the conformation tensor formulation for the extra-stresses, as described in Subsection 1.3.1. The square-root method, as formulated by Balci et al. [102], proposes an alternative way of writing the conformation tensor, as the product between the transpose matrix of the square-root tensor $\boldsymbol{b}$ and the tensor itself,

$$\boldsymbol{c} = \boldsymbol{b}^T \cdot \boldsymbol{b}, \tag{2.32}$$

in which the central dot $(\cdot)$ stands here for the matrix multiplication operator. This notation will be adopted throughout the present Section.

The tensor $\boldsymbol{c}$ is by definition a SPD tensor, so it possesses a unique positive definite symmetric square-root $\boldsymbol{b}$. That being said, we can also write Eq. 2.32 as $\boldsymbol{c} = \boldsymbol{b} \cdot \boldsymbol{b}$. We can now derive an evolution equation for $\boldsymbol{b}$ following the Oldoyrd-B constitutive model, by adapting the mathematical manipulation suggested in the work of Chen et al. [111]. Replacing Eq. 2.32 into Eq. 1.11 and using Eq. 1.12 gives

$$\frac{D\boldsymbol{b}^T}{Dt} \cdot \boldsymbol{b} + \boldsymbol{b}^T \cdot \frac{D\boldsymbol{b}}{Dt} - \boldsymbol{b}^T \cdot \boldsymbol{b} \cdot \boldsymbol{\nabla u} - \boldsymbol{\nabla u}^T \cdot \boldsymbol{b}^T \cdot \boldsymbol{b} + \frac{\boldsymbol{b}^T \cdot \boldsymbol{b} - \boldsymbol{I}}{\lambda} = 0, \tag{2.33}$$

in which $\boldsymbol{I}$ represents the identity matrix.

Multiplying Eq. 2.33 on the left by $\boldsymbol{b}^{-T}$ $(= (\boldsymbol{b}^{-1})^T$, *i.e.* the transpose of the inverse of $\boldsymbol{b})$ and on the right by $\boldsymbol{b}^{-1}$, and rearranging, yields

$$\left(\frac{D\boldsymbol{b}}{Dt} - \boldsymbol{b} \cdot \boldsymbol{\nabla u} + \frac{\boldsymbol{b} - \boldsymbol{b}^{-T}}{2\lambda} \right) \cdot \boldsymbol{b}^{-1} = -\boldsymbol{b}^{-T} \cdot \left(\frac{D\boldsymbol{b}^T}{Dt} - \boldsymbol{\nabla u}^T \cdot \boldsymbol{b}^T + \frac{\boldsymbol{b}^T - \boldsymbol{b}^{-1}}{2\lambda} \right). \tag{2.34}$$

Regarding Eq. 2.34, it can readily be shown that one side is minus the transpose of the other. Therefore, each side of this equation must be anti-symmetric, which gives

$$\left(\frac{D\boldsymbol{b}}{Dt} - \boldsymbol{b}\cdot\boldsymbol{\nabla u} + \frac{\boldsymbol{b}-\boldsymbol{b}^{-T}}{2\lambda}\right)\cdot\boldsymbol{b}^{-1} = \boldsymbol{a}, \tag{2.35}$$

or

$$-\boldsymbol{b}^{-T}\cdot\left(\frac{D\boldsymbol{b}^{T}}{Dt} - \boldsymbol{\nabla u}^{T}\cdot\boldsymbol{b}^{T} + \frac{\boldsymbol{b}^{T}-\boldsymbol{b}^{-1}}{2\lambda}\right) = \boldsymbol{a}, \tag{2.36}$$

where $\boldsymbol{a}$ is an anti-symmetric tensor. Since $\boldsymbol{b} = \boldsymbol{b}^T$ and the goal here is to find an evolution equation for the square-root of the tensor $\boldsymbol{c}$, one can either multiply Eq. 2.35 by $\boldsymbol{b}$ (on the right) or $\boldsymbol{b}^T$ by Eq. 2.36 (on the left), which respectively yields

$$\frac{D\boldsymbol{b}}{Dt} - \boldsymbol{b}\cdot\boldsymbol{\nabla u} - \boldsymbol{a}\cdot\boldsymbol{b} + \frac{\boldsymbol{b}-\boldsymbol{b}^{-1}}{2\lambda} = 0, \tag{2.37}$$

and

$$\frac{D\boldsymbol{b}}{Dt} - \boldsymbol{\nabla u}^{T}\cdot\boldsymbol{b} + \boldsymbol{b}\cdot\boldsymbol{a} + \frac{\boldsymbol{b}-\boldsymbol{b}^{-1}}{2\lambda} = 0, \tag{2.38}$$

where we remark that the equivalences $\boldsymbol{b}^{-T} = (\boldsymbol{b}^{-1})^T = (\boldsymbol{b}^T)^{-1}$ and $\boldsymbol{b}^T = \boldsymbol{b}$ were used.

We can now expand the material derivative of the tensor $\boldsymbol{b}$ in Eq. 2.37 to achieve the final form of the evolution equation we are looking for:

$$\left(\frac{\partial\boldsymbol{b}}{\partial t} + \boldsymbol{u}\cdot\boldsymbol{\nabla b}\right) - \boldsymbol{b}\cdot\boldsymbol{\nabla u} - \boldsymbol{a}\cdot\boldsymbol{b} + \frac{\boldsymbol{b}-\boldsymbol{b}^{-1}}{2\lambda} = 0. \tag{2.39}$$

As highlighted by Balci et al. [102], the key point of this factorisation is to ensure the symmetry of $\boldsymbol{b}$ by suitably choosing the anti-symmetric tensor $\boldsymbol{a}$. Remark that the first and the last terms on the left-hand side in Eq. 2.37 are the same as in Eq. 2.38. Defining $\boldsymbol{r} = \boldsymbol{b}\cdot\boldsymbol{\nabla u} + \boldsymbol{a}\cdot\boldsymbol{b}$, the transpose of $\boldsymbol{r}$ is $\boldsymbol{r}^T = \boldsymbol{\nabla u}^T\cdot\boldsymbol{b}^T + \boldsymbol{b}^T\cdot\boldsymbol{a}^T = \boldsymbol{\nabla u}^T\cdot\boldsymbol{b} - \boldsymbol{b}\cdot\boldsymbol{a}$. Looking closely, we can recognise that the two inner terms in Eq. 2.37 are equal to $-\boldsymbol{r}$ and, in Eq. 2.38, equal to $-\boldsymbol{r}^T$. Since Eq. 2.37 is equal to Eq. 2.38, $\boldsymbol{r}$ must be equal to $\boldsymbol{r}^T$, which implies that $\boldsymbol{r}$ is symmetric. Thus, if $\boldsymbol{r} = \boldsymbol{r}^T$, the entries of tensor $\boldsymbol{a}$ can be calculated as a function of $\boldsymbol{b}$ and $\boldsymbol{\nabla u}(=\nabla u_{ij})$ by the relation $r_{ij} = r_{ji}$, which sets the linear system

$$\begin{pmatrix} b_{11}+b_{22} & b_{23} & -b_{13} \\ b_{23} & b_{11}+b_{33} & b_{12} \\ -b_{13} & b_{12} & b_{22}+b_{33} \end{pmatrix}\begin{pmatrix} a_{12} \\ a_{13} \\ a_{23} \end{pmatrix} = \begin{pmatrix} t_1 \\ t_2 \\ t_3 \end{pmatrix}, \tag{2.40}$$

where the terms $t_{1,2,3}$ read (for 3D space):

$$\begin{aligned} t_1 &= (b_{12}\nabla u_{11} - b_{11}\nabla u_{12}) + (b_{22}\nabla u_{21} - b_{12}\nabla u_{22}) + (b_{23}\nabla u_{31} - b_{13}\nabla u_{32}) \\ t_2 &= (b_{13}\nabla u_{11} - b_{11}\nabla u_{13}) + (b_{33}\nabla u_{31} - b_{13}\nabla u_{33}) + (b_{23}\nabla u_{21} - b_{12}\nabla u_{23}) \\ t_3 &= (b_{13}\nabla u_{12} - b_{12}\nabla u_{13}) + (b_{23}\nabla u_{22} - b_{22}\nabla u_{23}) + (b_{33}\nabla u_{32} - b_{23}\nabla u_{33}) \end{aligned} . \tag{2.41}$$

In Appendix A, we can inspect the steps added to the GILCART algorithm after the implementation of this stabilising technique.

2.4 Validation of implemented tools: improvement on numerical stability

To validate the code modifications executed following the procedures exposed in Section 2.3, numerical simulations were performed for a standard benchmark geometry, a two-dimensional planar channel. Mostly due to its simplicity, the planar channel flow has been a particularly appealing reference flow for both theoretical and experimental research in fluid dynamics. For that reason, these initial studies that concern validation of numerical implementations into the flow solver were carried out on this setup. We start by detailing the geometry and simulation parameters, then we present an analytical solution for our benchmark problem; following that, we discuss the results obtained by means of the square-root formulation, by comparing the latter with the original method; finally, conclusions are drawn.

2.4.1 Geometric configuration and simulation settings

We consider here our two-dimensional channel, whose length-to-width ratio was fixed at $10:1$; this proportion is confirmed to be enough for the flow to be fully developed away from the inlet [127]. A schematic representation of the channel geometry is displayed in Fig. 2.2.

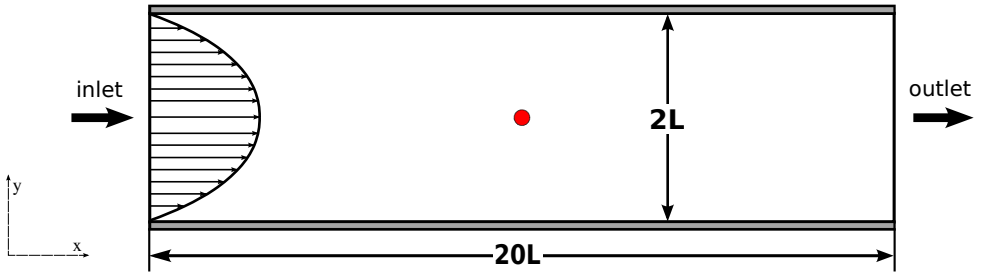

Figure 2.2 – Schematics of the 2D channel geometry, with half-width L and length-to-width ratio of $10:1$; the position of a numerical probe located at the centre of the channel is shown as a red dot.

Fully developed velocity profile (with bulk average magnitude U_b) is applied at the inlet, where a zero-gradient boundary condition is imposed for the pressure field and extra-stress is set to zero. At the outlet, a homogeneous Dirichlet boundary condition is assumed for the pressure (*i.e.* $p = 0$), as well as zero-gradient conditions for both velocity and extra-stress fields. At the walls, we apply the no-slip condition (*i.e.* $u = v = 0$). The

velocity and stress initial condition corresponds to no flow and initial pressure is set to zero.

For all the results hereafter exposed, we adopted the Oldroyd-B constitutive model with the classical viscosity ratio of $\beta = 1/9$, representing concentrated polymer solutions; the other control parameters of our flows are the Reynolds $Re = \rho U_b L/\eta_t$ and the Weissenberg $Wi = \lambda\dot{\gamma} = \lambda U_b/L$ numbers, where L is the channel half-width and $\eta_t = \eta_s + \eta_p$.

2.4.2 Mathematical and analytical framework

We present mathematical hypotheses that lead to closed-form analytical solutions of the governing equations, applied to an Oldroyd-B fluid flow in a two-dimensional channel, where x and y represent the streamwise and wall-normal directions, respectively, and $\boldsymbol{u} = (u, v)$ are the corresponding velocity components. The procedures illustrated here are based on those described in the work of Cruz et al. [128].

In a first moment, we write the momentum conservation equation displayed in Eq. 1.8 for the relevant momentum component in a laminar flow (here, in the streamwise $x-$direction),

$$\rho\left(\frac{\partial u}{\partial t} + u\frac{\partial u}{\partial x} + v\frac{\partial u}{\partial y}\right) = \eta_s\left(\frac{\partial^2 u}{\partial x^2} + \frac{\partial^2 u}{\partial y^2}\right) + \left(\frac{\partial \tau_{xx}}{\partial x} + \frac{\partial \tau_{xy}}{\partial y}\right) - \frac{\partial p}{\partial x}. \tag{2.42}$$

We make some considerations at this point:

- Steady state reached, the flow is time-independent $\left(\frac{\partial}{\partial t} = 0\right)$;
- Flow velocity components, other than the main direction are negligible, which yields $v = 0$;
- Flow is considered to be fully developed, so velocity and stress fields do not depend any more on the main flow direction, which implies $\frac{\partial}{\partial x} = 0$ for all terms in Eq. 2.42, except the pressure gradient;
- All body forces are neglected, including gravity.

After all the above considerations, Eq. 2.42 is reduced to

$$\frac{\partial}{\partial y}\left(\eta_s\frac{\partial u}{\partial y} + \tau_{xy}\right) = \frac{\partial p}{\partial x}, \tag{2.43}$$

which can be solved analytically for the $x-$component of the velocity (see Appendix B, for details on the solution),

$$u(y) = \frac{3}{2} \cdot u_{avg} \left[1 - \left(\frac{y}{L} \right)^2 \right], \tag{2.44}$$

in which u_{avg} is the mean velocity.

Note that, for the Oldroyd-B model the expression for the flow velocity coincides with the Poiseuille flow parabolic solution. An explicit analytical expression for the three components of the symmetric extra-stress tensor $\boldsymbol{\tau}$ can be derived as well, in the case of a steady parallel flow $\boldsymbol{u} = u(y)$ in a planar channel, directly from Eq. 1.9 and evaluating the derivative of the function displayed in Eq. 2.44,

$$\tau_{xx} = 2\,\eta_p \lambda \left(\frac{\partial u}{\partial y} \right)^2 = 18\,\eta_p \lambda\, u_{avg}^2 \left(\frac{y}{L^2} \right)^2, \tag{2.45}$$

$$\tau_{xy} = \tau_{yx} = \eta_p \frac{\partial u}{\partial y} = -3\,\eta_p\, u_{avg} \left(\frac{y}{L^2} \right), \tag{2.46}$$

$$\tau_{yy} = 0\,. \tag{2.47}$$

We remind that the analytical solutions provided above are valid only for steady laminar flows, with relatively low Re and Wi numbers.

2.4.3 Assessing the code's spatial accuracy

As a preliminary result, we check the order of convergence of the spatial accuracy of the numerical methods employed, after the implementation of the square-root factorisation. The parameters adopted for this first study are $Re = 1$ and $Wi = 0.1$, which was verified as corresponding to a laminar flow. For the spatial accuracy analysis, a regular quadrilateral mesh was used, with 40 cells in the streamwise (x) direction and progressively increasing number of cells in the wall-normal (y) direction.

In Fig. 2.3, we verify that solutions for increasingly refined meshes and calculated for the channel geometry approach the analytical velocity profile. The numerical profiles were extracted here from the vertical axis passing through the middle of the channel and the quantity displayed has been made dimensionless by an appropriate parameter.

The normalised average error in this study (ε_{norm}) is obtained in a similar way to that presented in the work of Duarte et al. [129], by averaging the absolute value of the difference between numerical streamwise velocity given by the flow solver and analytical solution provided by Eq. 2.44, over the y–direction, for a fully developed flow,

$$\varepsilon_{norm} = \frac{1}{N_y} \sum_{j=1}^{N_y} |u_j - u_j^a|, \tag{2.48}$$

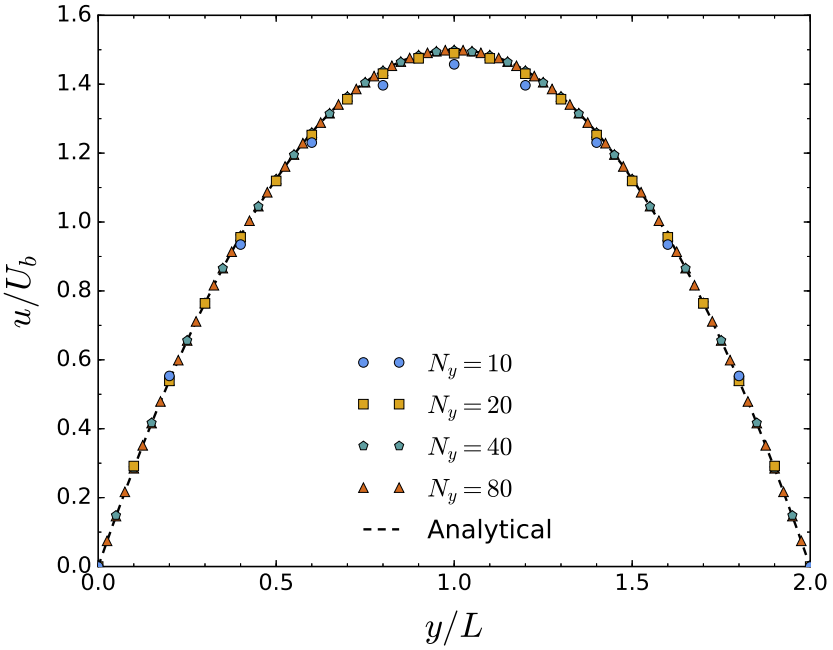

Figure 2.3 – Convergence of the fully developed normalised velocity profile in the channel geometry, for meshes with successive refinement in the wall-normal direction; here $Re = 1$ and $Wi = 0.1$.

where u_j is the calculated velocity at the point j, u_j^a is the analytical exact value for the velocity magnitude at that point and N_y represents the number of cells in the y–direction. Figure 2.4 shows the convergence of average error as the grid is refined, in a log-log plot, along with the corresponding fitting curve, whose logarithmic slope matches with the expected value of a second-order scheme (slope $\simeq 2$).

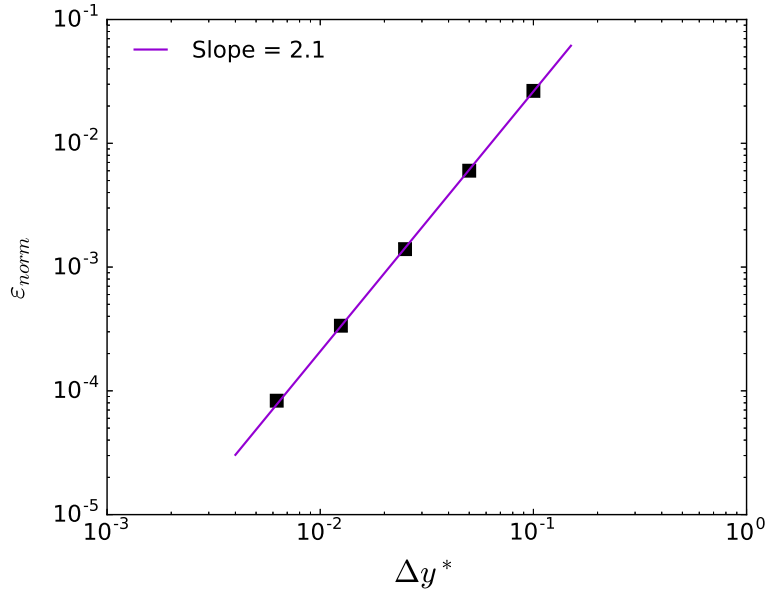

Figure 2.4 – Normalised average discretisation error ε_{norm}, evaluated by Eq. 2.48, as function of the normalised grid spacing Δy^*, for $Re = 1$ and $Wi = 0.1$.

2.4.4 Comparison between different formulations

Multiple analyses were performed to validate the implementation of the square-root technique into the fluid flow solver. Adopting the same two-dimensional channel geometry, with the viscosity ratio fixed at $\beta = 1/9$, we increased the elasticity parameter Wi by discrete increments, verifying the usefulness and effectiveness of the stabilising technique compared to previously validated flow solutions. In order to minimise the contribution from effects of flow inertia, Reynolds number is fixed once more at a relatively small value of $Re = 1$.

For the following results a non-regular mesh was selected, in order to achieve a (mirrored) geometrical refinement along the cross-stream direction, starting from the central axis of the geometry; a total of 100×40 cells composes the grid along the $x-$ and $y-$directions, respectively. Fully developed profiles calculated numerically for the velocity and extra-stresses components have been compared to their analytical counterparts, derived in Subsection 2.4.2 and that match with those provided by Dallas et al. [130]. These profiles are extracted from the vertical axis passing through the middle of the channel and are depicted in Figs. 2.5 and 2.6, for $Wi = 0.1$ and 1, respectively. Concerning the simulations performed following the square-root factorisation, the extra-stress tensor $\boldsymbol{\tau}$ is retrieved from the square-root tensor $\boldsymbol{b}$ by using the relation shown in Eq. 2.49,

$$\boldsymbol{\tau} = \frac{\eta_p}{\lambda}\left(\boldsymbol{b}\cdot\boldsymbol{b} - \boldsymbol{I}\right). \tag{2.49}$$

The velocity profiles exhibited in Figs. 2.5a and 2.6a are normalised by the bulk velocity U_b, while the extra-stress profiles in Figs. 2.5b to 2.5d and Figs. 2.6b to 2.6d are non-dimensionalised according to Eq. 2.50,

$$\tau_{ij}^{*} = \tau_{ij}\,\frac{2L}{U_b\left(\eta_s + \eta_p\right)}. \tag{2.50}$$

An explicit result presented in Fig. 2.5 is the very good agreement between the two formulations (standard and square-root) for each one of the four profiles at $Wi = 0.1$, which is the expected result due to the absence of elastic instabilities at that level of elasticity. These formulations are validated by a comparison with the analytical solution for the same profiles. One can notice that the small difference found in Fig. 2.5c is due to numerical round-off errors.

Figure 2.6 depicts a similar behaviour, when Wi is increased tenfold ($Wi = 1$). Both numerical formulations produce the exact same fully developed profiles, but this time the numerical solutions start to slightly deviate from analytical curves. We suggest that this is caused by a decreasing in the accuracy of the numerical methods [131], even with the mathematical factorisation implemented, manifested also by larger discretisation

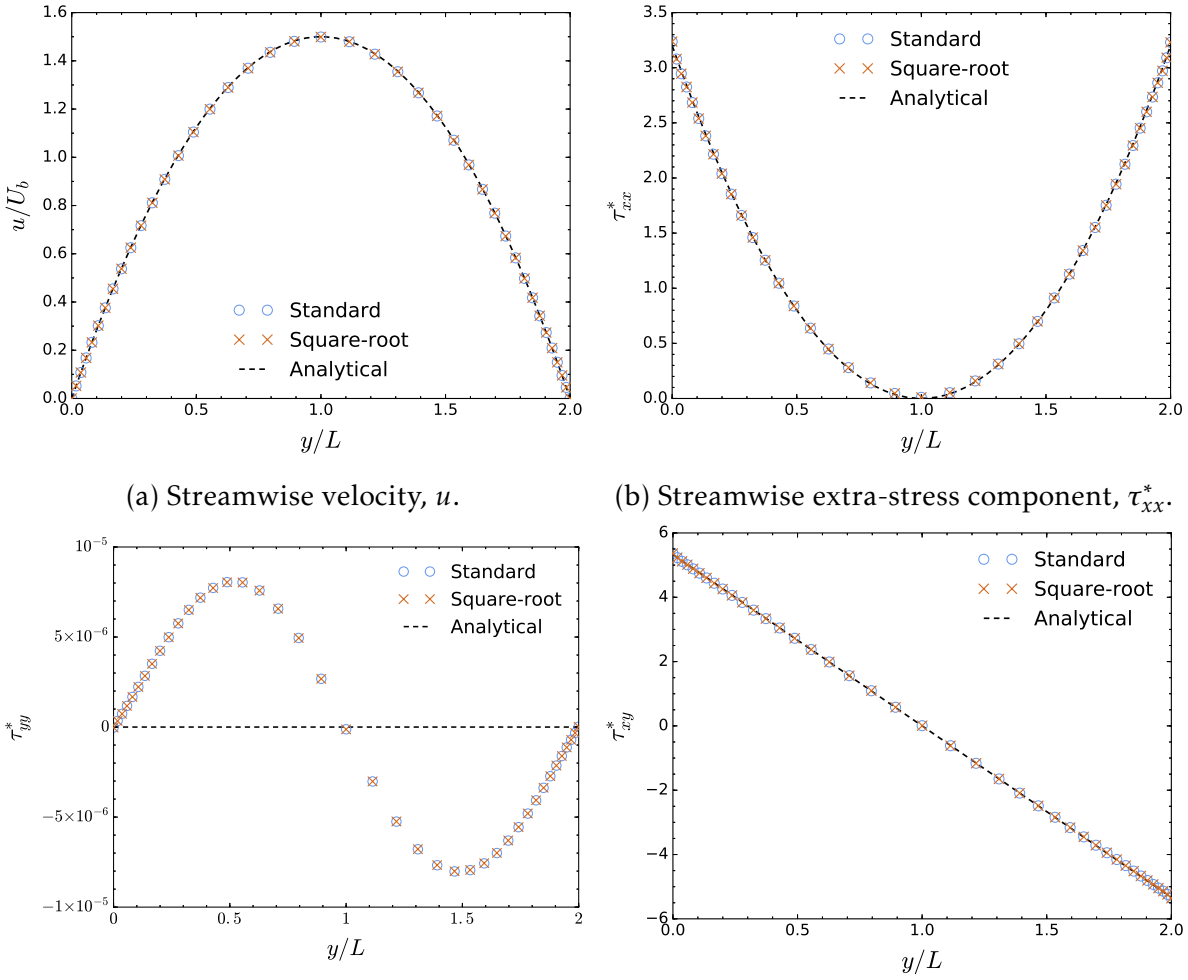

(a) Streamwise velocity, u.

(b) Streamwise extra-stress component, τ^*_{xx}.

(c) Wall-normal extra-stress component, τ^*_{yy}.

(d) Shearwise extra-stress component, τ^*_{xy}.

Figure 2.5 – Dimensionless profiles of (a) the streamwise velocity and (b – d) the components of the extra-stress tensor, extracted from a vertical axis at the middle of the two-dimensional channel; here $Re = 1$ and $Wi = 0.1$.

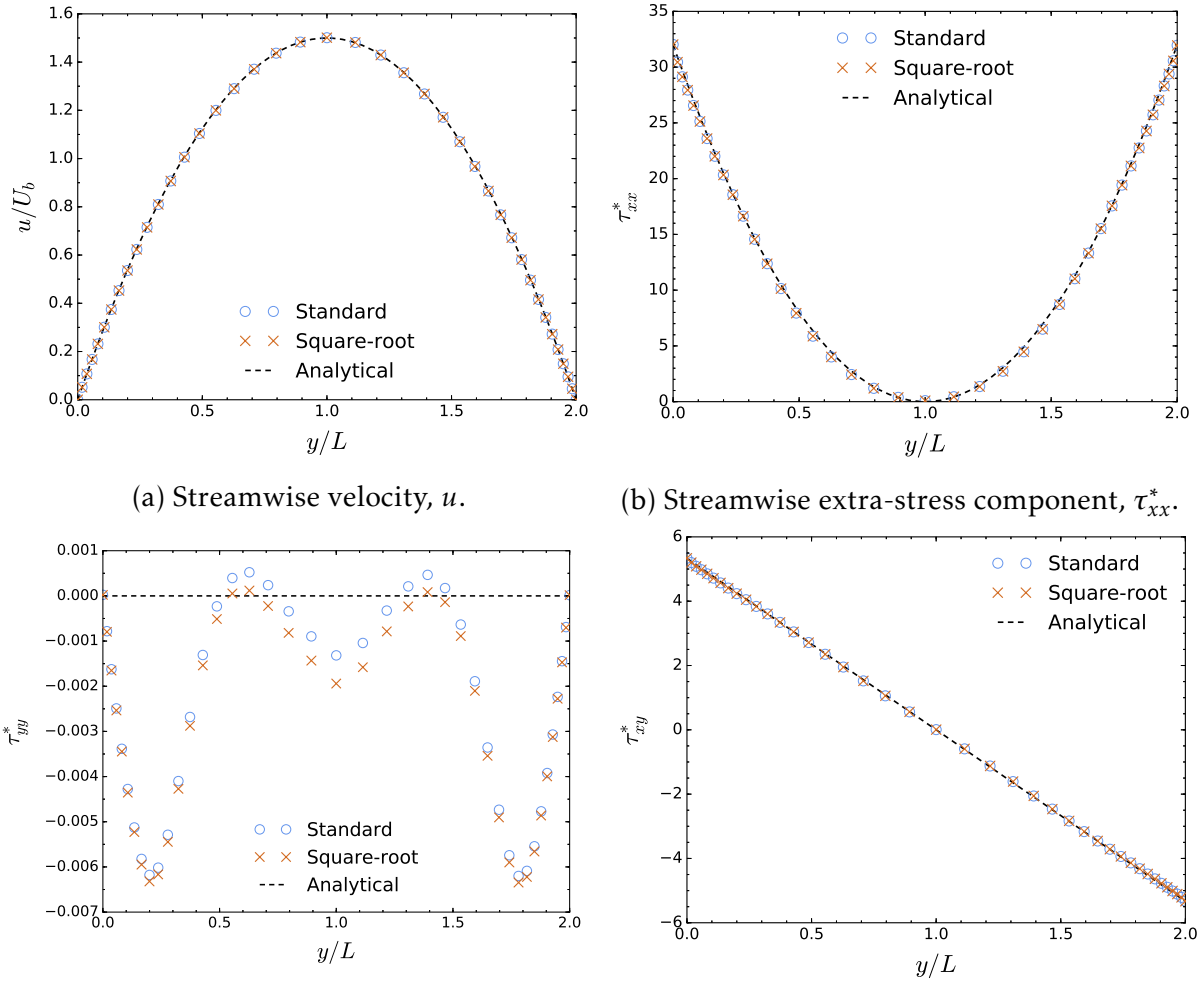

(a) Streamwise velocity, u.

(b) Streamwise extra-stress component, τ^*_{xx}.

(c) Wall-normal extra-stress component, τ^*_{yy}.

(d) Shearwise extra-stress component, τ^*_{xy}.

Figure 2.6 – Dimensionless profiles of (a) the streamwise velocity and (b – d) the components of the extra-stress tensor, for $Re = 1$ and $Wi = 1$.

errors for the wall-normal component of the extra-stress tensor (see Fig. 2.6c and compare it to Fig. 2.5c).

Moreover, simulations have been performed for increasingly more elastic flows (higher Wi) to detect the appearance of numerical instabilities and inspect to which extent the square-root formulation could control them. Our analysis here is based on the measurement of time series of velocity and of the material function N_1 at the centre of the channel, over durations corresponding to at least 40λ and up to 200λ. N_1 stands for the *first normal stress difference* and is defined as

$$N_1 = \tau_{xx} - \tau_{yy}\,. \tag{2.51}$$

A first notable result can be seen in Fig. 2.7, showing a non-negligible stabilisation of the temporal evolution of the measured quantities, for $Wi = 3$. Remark that the non-zero N_1 output comes from extrapolation errors at the computational cell closest to the central channel axis.

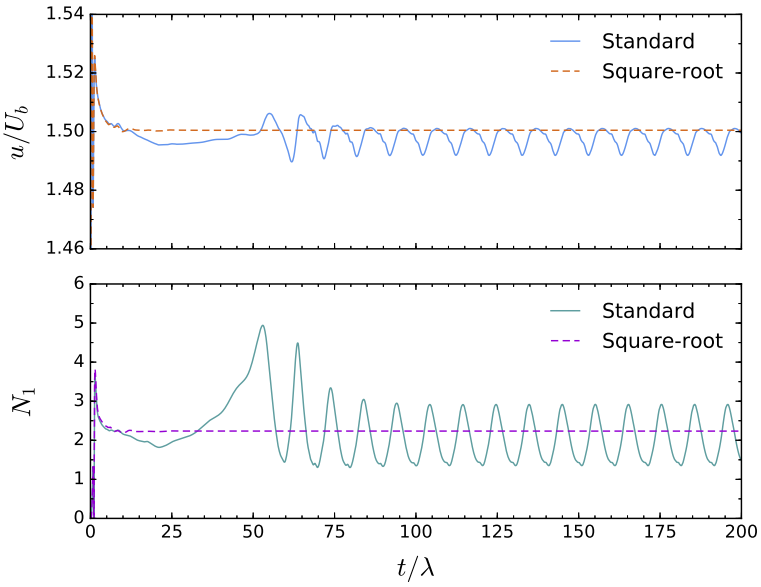

Figure 2.7 – Temporal evolution (including initial transient) of the normalised streamwise velocity component (top panel) and of the first normal stress difference (bottom panel) at the central point of the channel (see Fig. 2.2), for both formulations of the evolution of extra-stresses equation; here $Re = 1$ and $Wi = 3$.

Even for higher values of Wi (see Fig. 2.8, for $Wi = 4$), the square-root factorisation of the extra-stress equation indicates that a stationary state is reached, which provides evidence that neither the velocity oscillations nor the fluctuations in the first normal stress difference found by the original solver come from physical elastic instabilities, a fact that is equally corroborated by previous works [132–134]. Instead, these perturbations arise from numerical errors accumulated by the algorithm and comparable behaviours were investigated and reported elsewhere (*e.g.* by Chen et al. [111]).

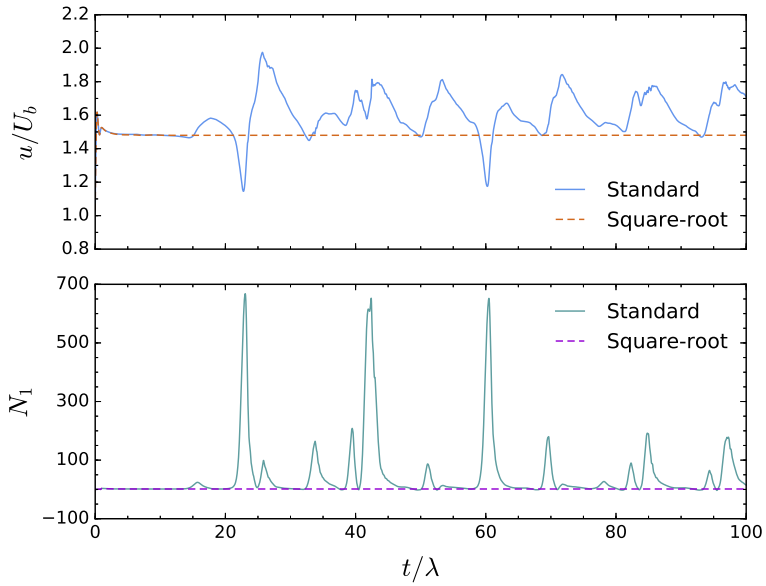

Figure 2.8 – Temporal evolution (including initial transient) of the normalised streamwise velocity component (top panel) and of the first normal stress difference (bottom panel) at the centre of the channel, for both formulations of the evolution of extra-stresses equation; here $Re = 1$ and $Wi = 4$.

When Wi is increased beyond a critical level of $Wi \approx 5$, the original formulation diverges numerically, while the square-root factorisation starts displaying fluctuations in the velocity field, as seen in the top panel of Fig. 2.9, for $Wi = 10$. Eventually, the code version with the stabilising feature will diverge as well, when stronger elasticity levels are attained.

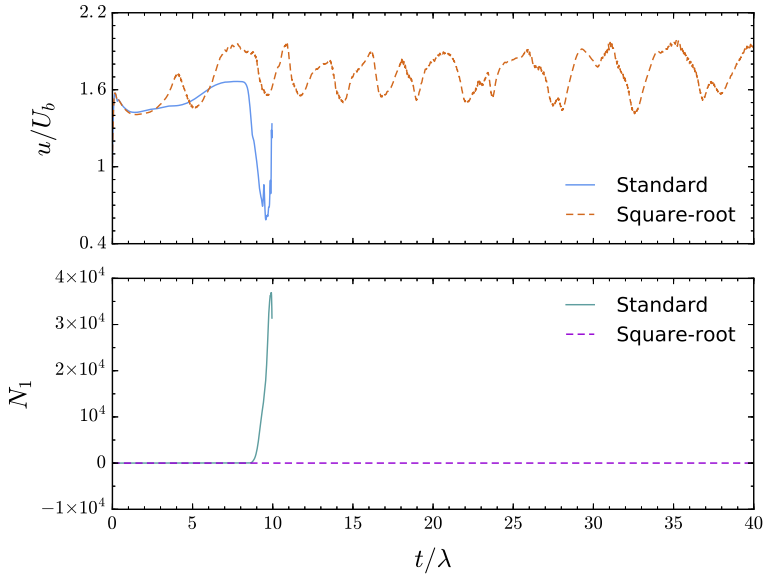

Figure 2.9 – Temporal evolution (including initial transient) of the normalised streamwise velocity component (top panel) and of the first normal stress difference (bottom panel) at the centre of the channel, for both formulations of the evolution of extra-stresses equation; here $Re = 1$ and $Wi = 10$.

2.5 Concluding remarks and motivation for an alternative solver

The results aforementioned could assertively validate the satisfactory implementation of the square-root method into the numerical algorithm, as well as its reliability and accuracy for laminar, low-Wi flows, for which the results matched accurately with those from the original and previously validated in-house solver. Increasing Wi, up to moderate levels, the formulation presented great success in stabilising the numerical output, confirming our expectations. A benchmark 2D geometry was adopted for the task, in order to assess the coverage and performance of this tool.

Even if this mathematical factorisation proved itself as a powerful technique to increase numerical stability in a finite-volume algorithm, it could not enable stable simulations in the planar channel for flows above an elasticity level corresponding to $Wi \gtrsim 5$. Furthermore, numerical simulations were performed using the square-root factorisation in a two-dimensional cross-slot geometry [135] and numerical divergence was again reported beyond certain limits of elasticity. These limits were found to be around $Wi \approx 0.1$, *i.e.* at least one order of magnitude smaller than the required Wi to numerically explore time-dependent instabilities in the cross-slot geometry, according to previous studies from the literature, in similar setups [136, 137].

The results obtained for these elasticity levels can be compared to those in the work of Fattal and Kupferman [36], where their original implementation of a different stabilising methodology (the log-conformation representation) produced enhanced accuracy at low and moderate Wi, but eventually lost stability at tougher conditions (see Fig. 2 in the introductory Chapter of this document). To numerically explore physical behaviours that happen at even more elastic flows, like the interesting phenomena outlined in the introductory Section of this document, one can thus infer that multiple and advanced numerical tools must be present in a given viscoelastic flow solver.

In order to extend our calculations, we decided to change our main solver for the upcoming analyses, which forms the second part of this thesis. The open-source numerical solver rheoTool® [138] was chosen as the alternative code, which is developed within the C++ OpenFOAM® framework [139]. This solver is equally based on a finite-volume discretisation and features the square-root method along with many other techniques for increased stability (including the LCR approach previously mentioned).

Part II

Viscoelastic fluid flows in a two-dimensional cross-slot and transition to elastic turbulence

Chapter 3

Purely elastic instabilities in the cross-slot geometry

3.1 Viscoelastic flows: instabilities in the cross-slot geometry

The elasticity of the flow of polymer solutions can give rise to complex dynamics and instabilities that are relevant for both fundamental studies and industrial applications, as *e.g.* efficient mixing and heat transfer in microdevices [22], or painting and coating processes [140, 141]. A particular class of instabilities is the so-called *purely elastic* one, occurring in the limit of vanishing fluid inertia, in which the flow instabilities that arise and yield unusual (in comparison to equivalent Newtonian flows) states or time-dependent behaviour are generated solely by the elasticity of the fluid [142].

Probably, the first experimental evidence of this kind of instabilities was provided by Giesekus [143], where a secondary flow in non-Newtonian solutions has been produced by a purely elastic mechanism. The purely elastic instabilities marking the transitions between different flow regimes have since then been documented in a variety of geometrical configurations [9, 96, 144–146], including complex ones, such as the abrupt axisymmetric contraction [147] and the lid-driven cavity [148]. Even some comprehensive review of purely elastic instabilities have been compiled (*e.g.* by Shaqfeh [140]). To illustrate this point and show the richness of purely elastic instabilities, we display in Fig. 3.1 an extensive flow instability map, as reported by Poole [149]. In that chart, they have been divided in categories according to the prevalent kinematics of the setup, *e.g.* extension-dominated, shear-dominated or mixed kinematics.

Posteriorly, a dimensionless criterion was proposed by McKinley et al. [150], defining some critical conditions beyond which the onset of purely elastic instabilities can develop. This non-dimensional parameter, sometimes called *Pakdel-McKinley (PMcK) criterion* combines the calculation of flow streamlines' curvature and normal stresses,

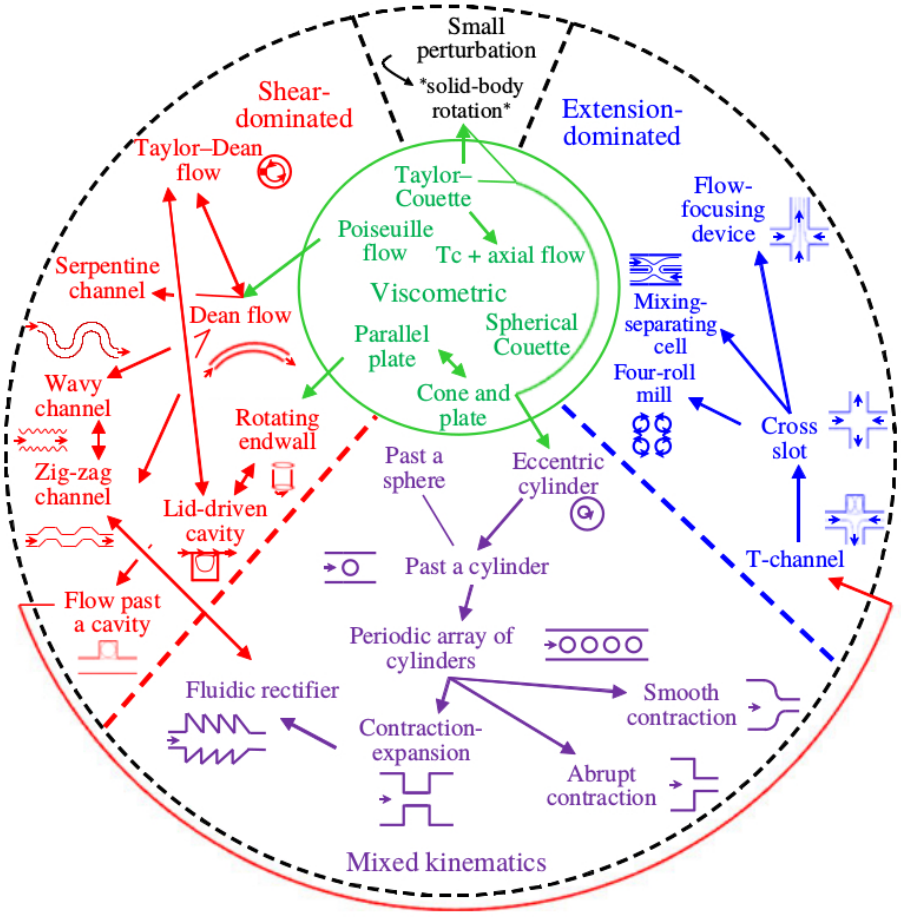

Figure 3.1 – Chart of purely elastic flow instabilities, categorised according to the prevalent kinematics of the geometric setup (extracted from [149]).

two properties which are thought to be the main responsible for the destabilising mechanism. In all these cases, small geometrical length scales have great importance on the appearance and amplification of remarkable non-Newtonian effects, because of the inherent low Reynolds (Re) and high Weissenberg (Wi) numbers [151].

The standard cross-slot setup is made of two perpendicularly intersecting channels with two inlets and two outlets, displaying a free (not-pinned) central stagnation point, in which fluid velocity is zero and strain rate is finite [152]. This geometrical configuration has attracted considerable attention for practical applications, as *e.g.* its employment by Dylla-Spears et al. [153] to trap and stretch single molecules in the central stagnation point in the purpose of targeting sequences along the DNA backbone. Nonetheless, this setup was especially adopted for rheometrical measurements. Using the cross-slot device, Odell and Carrington [154] proposed an Extensional Flow Oscillatory Rheometer (EFOR), for the evaluation of the extensional viscosity of low-viscosity fluids. The apparatus (shown in Fig. 3.2) operates using a combination of the extensional flow field generated downstream the stagnation point with an oscillatory flow. This technique proved itself capable of precisely characterising both the shear

and extensional response of low-viscosity fluids and has actually been used in recent studies on low-viscosity polymer solutions [155, 156].

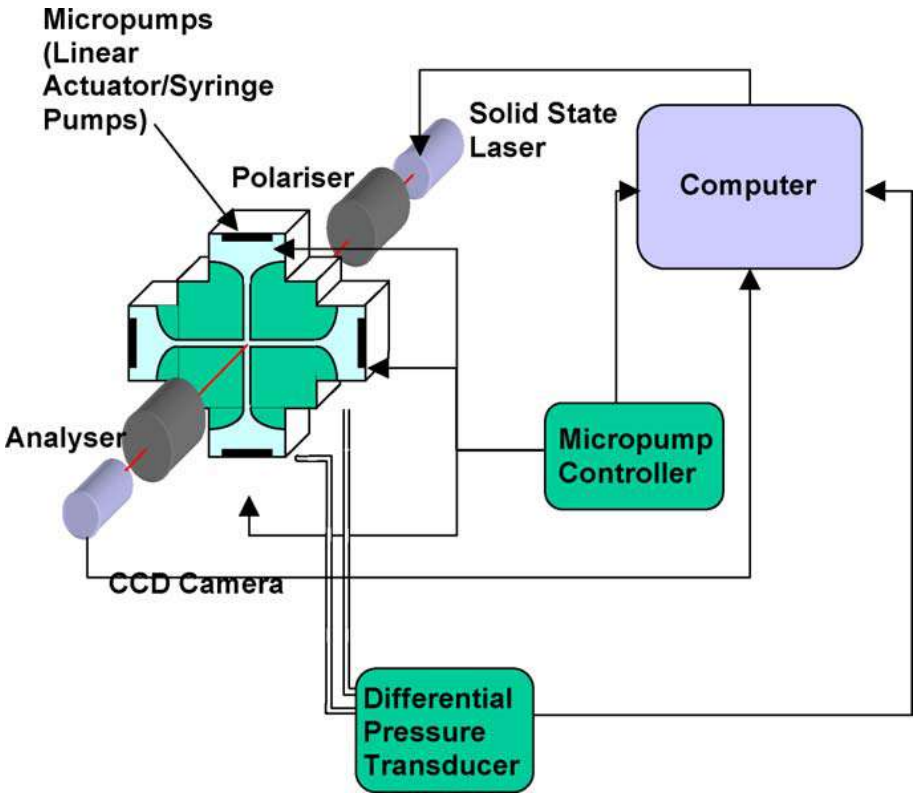

Figure 3.2 – Schematics of the **E**xtensional **F**low **O**scillatory **R**heometer (EFOR), in which a cross-slot geometry is used for rheological measures of low-viscosity fluids (extracted from [154]).

Due to its relevance for mixing and rheology, it has been the subject of extensive studies. Indeed, experimental [157–159], theoretical [160, 161] and numerical [68, 72, 136] investigations have reported about the existence of instabilities solely driven by elasticity in this setup. Two conceptually different types of instabilities have been reported for low-Reynolds-number polymeric flows in this geometry: a first one, corresponding to a steady asymmetric bifurcation [72, 136], and a second one leading to unsteady oscillatory behaviour [136, 158, 162]. Along with numerical solutions, analytical solutions for somewhat specific cases have been provided. Such solutions rely on flow symmetry properties and some simplifications, as in the works of Becherer et al. [161] and Cruz and Pinho [163], where wall-free purely extensional flows were considered. Analogously, Chaffin and Rees [164] provided analytical solutions (although not explicitly) for the stress components in a viscoelastic cross-slot flow under the shallow, Hele-Shaw flow limit [165].

Recently, this flow configuration has been proposed as a benchmark problem [137], for its geometrical characteristics and the existence of the instability leading to asymmetric flow at appropriate β, Re and Wi values. Similar viscoelastic instabilities were

reported for geometries alike to the cross-slot with minor modifications, as in the case of a flow-focusing device [166] or a T-junction setup [167].

3.1.1 The asymmetric bifurcation

A stationary bifurcation induced by a purely elastic instability in the cross-slot geometry (displayed in Fig. 3.3) was detected initially in the work of Gardner et al. [168] and extensively explored by Arratia et al. [158], where both types (see previous Section) of flow instabilities were identified experimentally in this planar extensional flow. They proved also by their experiments that the Poiseuille outflow is strongly perturbed far downstream of the central stagnation point, due to these purely elastic instabilities. Later on, Poole et al. [136] showed numerically that even simple differential viscoelastic models, like the UCM model, could predict such behaviour in two-dimensional flows, in total absence of inertia.

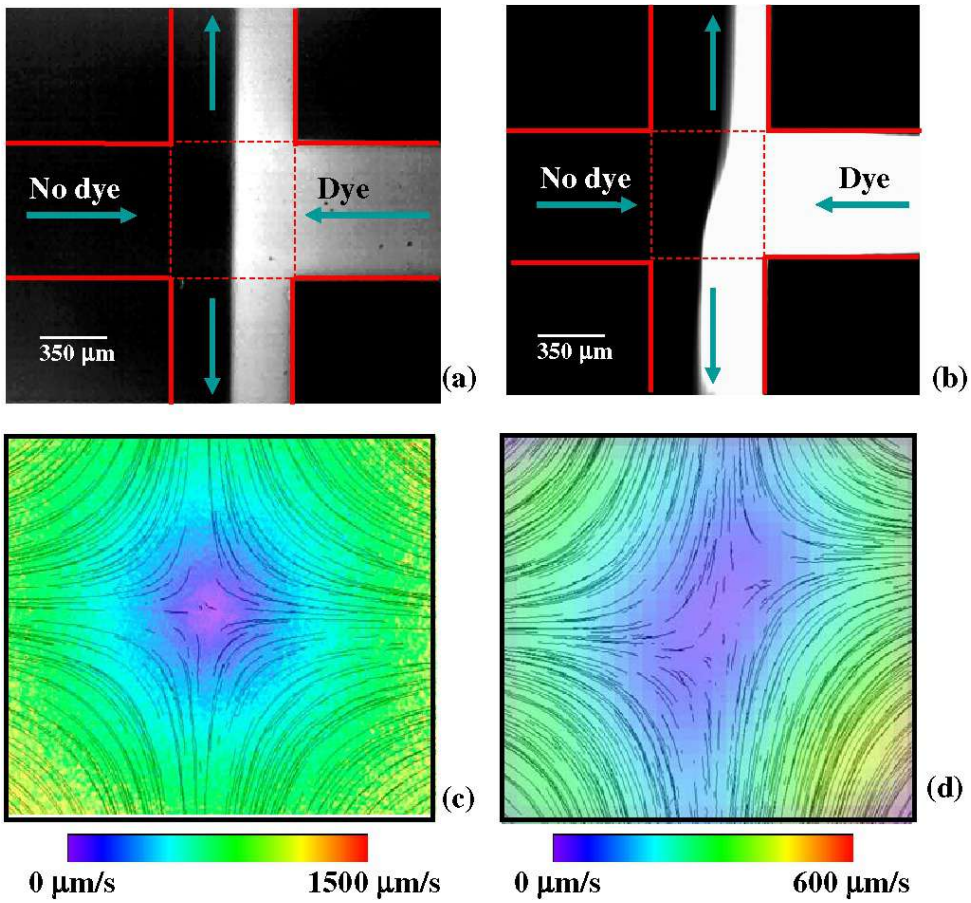

Figure 3.3 – Patterns of dye advection (a) and (b), and particle streak lines (c) and (d), comparing a Newtonian fluid flow (left panels) to the flow of a PAA flexible polymer solution (right panels) at $Re < 10^{-2}$. A purely elastic, symmetry-breaking steady flow bifurcation is clearly visible (extracted from [158]).

The asymmetric flow pattern produced in the cross-slot viscoelastic flow for small and moderate Wi was characterised as arising from a supercritical pitchfork bifurca-

tion [169, 170], which possesses two stable possible equilibrium states [171] and whose initial growth rate can be predicted by linear stability analysis [142]. An early theoretical work addressed Oldroyd-B flows in a simplified, unbounded cross-slot geometry through linear stability analysis, where disturbances were predicted to occur above a critical Wi [172].

Moreover, numerical studies suggested that above the critical level of elasticity necessary for the onset of the asymmetric flow behaviour, the bifurcated state is more stable than the symmetric one, where less energy is comparatively needed to maintain the asymmetric pattern [72, 137]. For the same geometry, further numerical studies have been carried out, using more complex and realistic viscoelastic models, taking into account the finite extensibility of polymer molecules: the FENE-P [72] and FENE-CR [72, 173] closures. Recently, Wilson [174] pointed out that the physical mechanism behind the emergence of this bifurcation remains an important mathematical open problem in the field of non-Newtonian fluid mechanics.

Additionally, a steady asymmetric bifurcation presenting a spiral-vortex structure was identified experimentally in a three-dimensional cross-slot [175] and posteriorly detected in numerical flow simulations adopting various elastic fluid models [176]; this 3D instability was later found to improve heat transfer between the two inlet streams [23]. Nonetheless, asymmetric bifurcations in the cross-slot do not show up exclusively for non-Newtonian fluid flows. Poole et al. [177] discovered inertia-driven symmetry breaking for a Newtonian fluid flow, in which the asymmetries display different properties when compared to those produced by viscoelastic effects, like an uncentred stagnation point and a distinct plane of symmetry.

3.1.2 The time-dependent instability

The second (and less documented) cross-slot instability corresponds to an unsteady transition. Xi and Graham [73] provided numerical evidence that, for a two-dimensional, highly dilute FENE-P fluid flow, it occurs via a supercritical Hopf bifurcation; by taking into account deviations in velocity, pressure and stress fields, a mechanism relying on the role of stress gradients and the existence of a stagnation point at the centre of the setup was also proposed [73].

The onset of a time-dependent instability has also been found by Afonso et al. [178] in a slightly modified geometry: a three-dimensional, six-arm cross-slot. For this setup, the authors associated the mechanism of the transition with large hoop stresses that develop in geometries with curved streamlines. Oscillatory solutions also appear in other extensional flows, like the flow of a viscoelastic fluid driven by a simple periodic background force in a four-roll mill device [8].

3.2 Regime of elastic turbulence

Above a critical Weissenberg number, meaning for elasticity larger than a threshold, purely elastic instabilities can lead to the appearance of disordered flows corresponding to the dynamical regime known as elastic turbulence [6, 9]. As shown in the seminal work of Groisman and Steinberg [9], where a swirling flow between counter-rotating parallel disks was considered (from which two snapshots can be seen in Fig. 3.4), and in subsequent ones also employing different geometries [1, 7], such flows are reminiscent of the turbulent ones occurring in Newtonian fluids [179]. In particular, they are characterised by a whole range of active scales, irregular temporal behaviour, growth of flow resistance by a factor up to twenty and enhanced mixing properties [1].

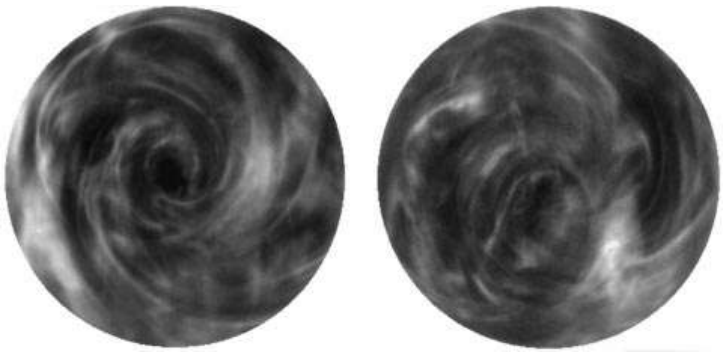

Figure 3.4 – Snapshots of the flow field in the elastic turbulence regime in a swirling flow between two parallel disks (extracted from [9]).

Interestingly, however, the spectrum of velocity fluctuations displays power-law behaviours, in both the temporal ($E(f) \sim f^{-\delta}$) and spatial ($E(k) \sim k^{-\delta}$) domains, with an exponent $\delta \gtrsim 3$, corresponding to a smooth flow essentially dominated by the largest spatial scales (see Fig. 3.5). It is worth to remark that such experimental findings are supported by theoretical predictions based on a simplified uniaxial model of viscoelastic fluid dynamics in the absence of walls and in homogeneous isotropic conditions [180].

Elastic turbulent flows have demonstrated an outstanding potential for practical applications in *e.g.* industrial processes. Besides the straightforward pertinence for accelerating fluid mixing [1, 12, 17], significant enhancement in the intensity of heat transfer (up to ~ 4 times, compared to an equivalent state without the development of the phenomenon) has been reported when fluid flows undergo this dynamical regime [22, 24]. By performing experimental studies in an adapted rheometrical device, Poole et al. [181] showed that elastic turbulent flows are capable of generating emulsification of immiscible viscous fluids. Moreover, Mitchell et al. [182] recently reported that elastic turbulence arising in a fully complex three-dimensional structure directly enhanced the efficiency of oil recovery in a porous medium.

More recently, the elasticity-driven transition to turbulent-like states was experimentally investigated in cross-slot devices of different aspect ratio (vertical size over channel

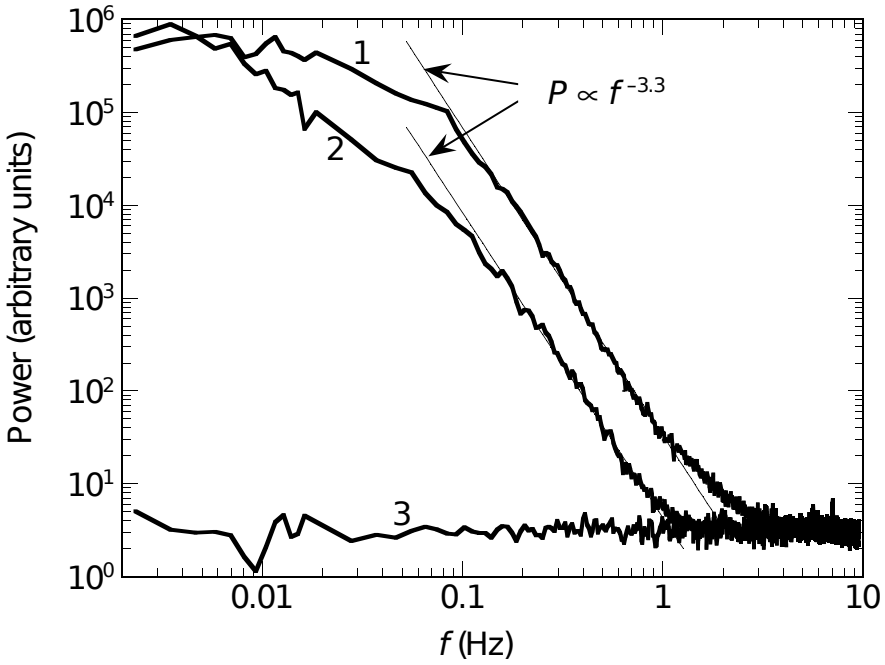

Figure 3.5 – Power spectra in the frequency domain (denoted here as P) of velocity fluctuations displaying a power-law decay with exponent $\delta > 3$ (extracted from [1]).

width), for more and less concentrated polymer solutions [20]. Independently of the aspect ratio, it was found that the more concentrated solution undergoes a transition to unsteady flows that become progressively more irregular when the Weissenberg number is increased. The power spectra of velocity fluctuations, obtained from single-point time series of the streamwise component (with respect to the laminar mean flow) measured in the outlet channel at midway from the lateral walls (both in the horizontal and vertical directions), were characterised by the presence of marked peaks (a fundamental frequency plus some harmonics), and by a power-law behaviour of exponent δ larger than 3, at small and large Wi values, respectively. In particular, for the smaller aspect ratio, continuous spectra and features typical of elastic turbulence were observed when $Wi \gtrsim 25$. For the more dilute solution, although the phenomenology of the time-dependent transition was similar, the chaotic flow observed at high Wi did not show similar spectral properties.

3.3 Effects of the variation of flow parameters

By analysing viscoelastic fluid flows in a cross-slot geometry, several physical and geometrical parameters can play more or less significant roles in the resulting flow state.

Starting with the Reynolds number, it has been repeatedly reported that differences between creeping conditions (inertialess flow) and very low Reynolds simulations are

negligible. Effects of inertia start to be relevant in the form of a stabilising mechanism for unitary values of this dimensionless parameter, for which the onset of the asymmetric instability is delayed and its strength is attenuated [136]. Instead, one parameter whose variation can produce remarkable effects on the flow configuration is the concentration of polymers, which has a decisive destabilising effect on the flow (as reported in an experimental study by Sousa et al. [159]). The maximum extensibility of the polymer chains present in the fluid flow also affects the onset of purely elastic instabilities, with the critical Wi associated to the bifurcation tending to decrease as maximum extensibility increases, for fixed values of β [72]. When investigating how the extensibility of polymer molecules present in the solution influences flow regimes, a non-linear elasticity model must be used for the numerical simulations, like the FENE family of models (see Subsection 1.3.2).

Furthermore, two main geometrical parameters analysed by recent studies are the aspect ratio (in 3D models) and the sharpness of internal cross-slot corners, which have been identified as having a stabilising and marginal effects on the bifurcation instability, respectively [72, 136]. Cruz et al. [137] also identified a slight decrease in the necessary flow energy to drive the cross-slot flow through the asymmetric pattern, when the corners are rounded with a radius of curvature of 5% of the channels' width.

To summarise, we report in Tab. 3.1 a synthetic review of past works in the literature concerning the study of purely elastic instabilities, by employing experimental, numerical and theoretical techniques. The dimensionality of the setup along with the type of instability investigated (first or second one) are also provided in Tab. 3.1.

Method	Publication	Fluid model	Dimension	Instability
Theoretical	Lagnado et al. [172]	Oldroyd-B	2D	1
Experimental	Arratia et al. [158]	–	3D	1
Numerical	Poole et al. [136]	UCM	2D	1
Numerical	Xi and Graham [73]	FENE-P	2D	2
Numerical	Rocha et al. [72]	FENE	2D	1
Numerical	Afonso et al. [178]	UCM	3D	1 & 2
Numerical	Cruz et al. [137]	Multiple	2D	1
Experimental	Haward et al. [162]	–	3D	1 & 2
Experimental	Dubash et al. [183]	–	3D	1 & 2
Experimental	Sousa et al. [159]	–	3D	1 & 2
Numerical	Junior et al. [113]	Oldroyd-B	2D	1
Numerical	Cruz et al. [184]	UCM & sPTT	3D	1 & 2
Experimental	Sousa et al. [20]	–	3D	2

Table 3.1 – Summary of recent works on purely elastic instabilities in the cross-slot geometry.

Chapter 4

OpenFOAM® solver and simulation settings

4.1 OpenFOAM®

OpenFOAM® [139] (acronym for **Open** Source **F**ield **O**peration **A**nd **M**anipulation) is an open-source CFD software that operates by means of different executables, known as *applications*. These applications use packaged functionalities contained within a collection of approximately one hundred libraries; all applications can be divided in two main groups: *solvers*, that are each conceived to solve specific (or a group of) problems in continuum mechanics; and *utilities*, mainly designed to handle pre- and post-processing tasks involving data manipulation and algebraic calculations. Figure 4.1 represents an overview of the structure of the OpenFOAM® libraries.

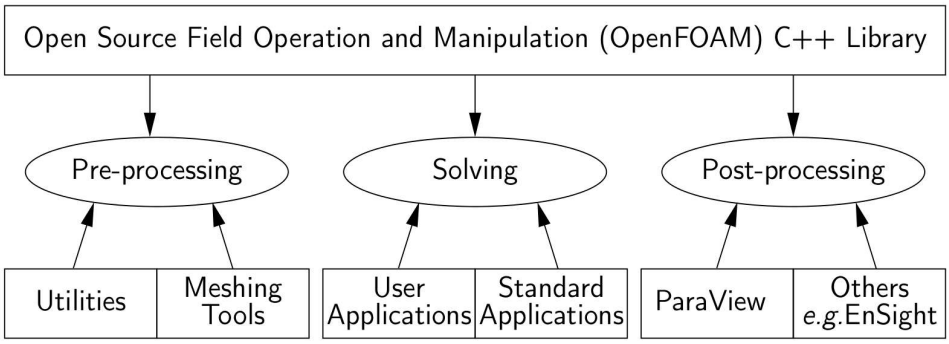

Figure 4.1 – Overview of OpenFOAM® structure (extracted from OpenFOAM® user guide, version 7).

The primary programming language of OpenFOAM® is *C++*, which was chosen on account of its object-oriented features like inheritance, template class, operator overloading and virtual classes, highly recommended for practical science and engineering numerical applications. Since its launching, OpenFOAM® has been extensively used for

scientific research in diversified fields, ranging from heat and mass transfer analyses (*e.g.* [185]) to the solution of the Maxwell's equations of electromagnetism (*e.g.* [186]). Among some of the noteworthy features of this toolbox, one can cite its ability to handle general unstructured polyhedral meshes and perform parallel calculations.

4.1.1 rheoTool® solver – special features

rheoTool® is a solver developed in the OpenFOAM® framework and based on a previous viscoelastic solver known as *viscoelasticFluidFoam* [187], which can be found in the extended version of OpenFOAM®. The latter solver already includes some of the most known viscoelastic constitutive models, such as Oldroyd-B, Giesekus and FENE. Both solvers employ a finite-volume discretisation based on pressure-correction solution techniques, which takes into account their natural conservative properties, generally recommended for most fluid dynamics problems [121, 138]. rheoTool® was launched with the premise of having special numerical features that could make previous *viscoelasticFluidFoam* solver more robust and stable, in the intention of making available to the general public such implemented tools. We resume below some of these features (for the 1.0 version of the code). All the details about each one of the features in this initial version of rheoTool® can be found in the work of Pimenta and Alves [138].

- The log-conformation representation approach (see Subsection 4.2.1) is available for all viscoelastic models, and the square-root method (see Section 2.3) is included for the Oldroyd-B model. These mathematical approaches are employed to control the numerical instabilities appearing at high Wi values.

- The pressure-velocity coupling is reinforced: the PISO [188] algorithm implemented in the *viscoelasticFluidFoam* solver is replaced by the SIMPLEC [189] algorithm, delivering more stability for transient simulations.

- Higher stability for viscoelastic fluid flows is provided by a new stress-velocity coupling formulation.

- A powerful high-resolution discretisation scheme (HRS) for the treatment of advection is implemented: the Convergent and Universally Bounded Interpolation Scheme for the Treatment of Advection (CUBISTA), devised by Alves et al. [190].

- A normalised variable approach for the HRS is incorporated into the code, in which some contribution of the discretised advective term is computed implicitly and the other part is treated explicitly. This technique is known as *deferred correction*.

4.2 Cross-slot geometry and boundary conditions

4.2.1 Governing equations

Firstly, we recall the physical equations that will now be integrated by means of the OpenFOAM® toolbox. To make sure that no effects of fluid inertia are present in our two-dimensional model, we remove the non-linear term from Eq. 1.8. So, the velocity field $\boldsymbol{u}(\boldsymbol{x},t) = (u_x(\boldsymbol{x},t), u_y(\boldsymbol{x},t))$ at position $\boldsymbol{x} = (x, y)$ and time t evolves according to the momentum conservation equation

$$\rho\frac{\partial \boldsymbol{u}}{\partial t} = \boldsymbol{\nabla}\cdot(\eta_s\,\boldsymbol{\nabla}\boldsymbol{u}) + \boldsymbol{\nabla}\cdot\boldsymbol{\tau} - \boldsymbol{\nabla}p\,, \tag{4.1}$$

and the incompressibility condition $\boldsymbol{\nabla}\cdot\boldsymbol{u} = 0$.

We adopt the Oldroyd-B model to describe the dynamics of the viscoelastic fluid, whose evolution equation is displayed in Eq. 1.9. We decided to employ here the LCR of the extra-stress equation (introduced in Subsection 1.4.2), essentially because it is included in the rheoTool® solver for many different fluid models; the square-root stabilising technique is also present in this numerical code, but available only for the Oldroyd-B constitutive model. Details on the LCR method are exposed below.

4.2.1.1 Log-conformation representation (LCR)

In addition to the square-root method, scrutinised in Section 2.3, another mathematical formulation that enables stable simulations of viscoelastic fluid flows at high Weissenberg numbers is the so-called *log-conformation representation*, presented by Fattal and Kupferman [35]. They suggested that the mechanism behind the computational instability when dealing with high elasticity levels was a poor polynomial approximation (by the numerical schemes) of the steep exponential growth experienced by the stress tensor, generated by a combination of deformation and advection. To overcome that, a stabilisation formulation was proposed, in which the constitutive equation displayed in Eq. 1.11 is reformulated in terms of the logarithm of the conformation tensor $\boldsymbol{\Theta} = log\,\boldsymbol{c}$. The final form of the Oldroyd-B constitutive equation following the LCR is:

$$\frac{\partial \boldsymbol{\Theta}}{\partial t} + \boldsymbol{u}\cdot\nabla\boldsymbol{\Theta} = (\boldsymbol{\Omega}\boldsymbol{\Theta} - \boldsymbol{\Theta}\boldsymbol{\Omega}) + 2\boldsymbol{\Psi} + \frac{1}{\lambda}\left(e^{-\boldsymbol{\Theta}} - \boldsymbol{I}\right), \tag{4.2}$$

where the tensors $\boldsymbol{\Psi}$ and $\boldsymbol{\Omega}$ form a decomposition of the velocity gradient $\boldsymbol{\nabla}\boldsymbol{u}$. The tensor $\boldsymbol{\Psi}$ is a symmetric, traceless tensor, while tensor $\boldsymbol{\Omega}$ is asymmetric; they generate pure strain and pure rotation, respectively [36].

4.2.2 Simulation numerical settings

We describe here our cross-slot setup, consisting of two bisecting channels of identical width d, with opposing inlets (here, along the x–direction) and outlets (along the y–direction), shown schematically in Fig. 4.2. Similarly to the reference studies with this geometry, here we set a length-to-width ratio of 10 : 1 for each of the four "arms", which was previously shown to be enough to ensure a fully developed flow away from the inlet in a channel [127]. The idea of somehow assimilating a cross-slot arm to a channel is equally found in previous works (see *e.g.* [177]). We also depict in Fig. 4.2 the positions where most of the time series were recorded: probe 1 (entrance, green), probe 2 (centre, red) and probe 3 (exit, blue).

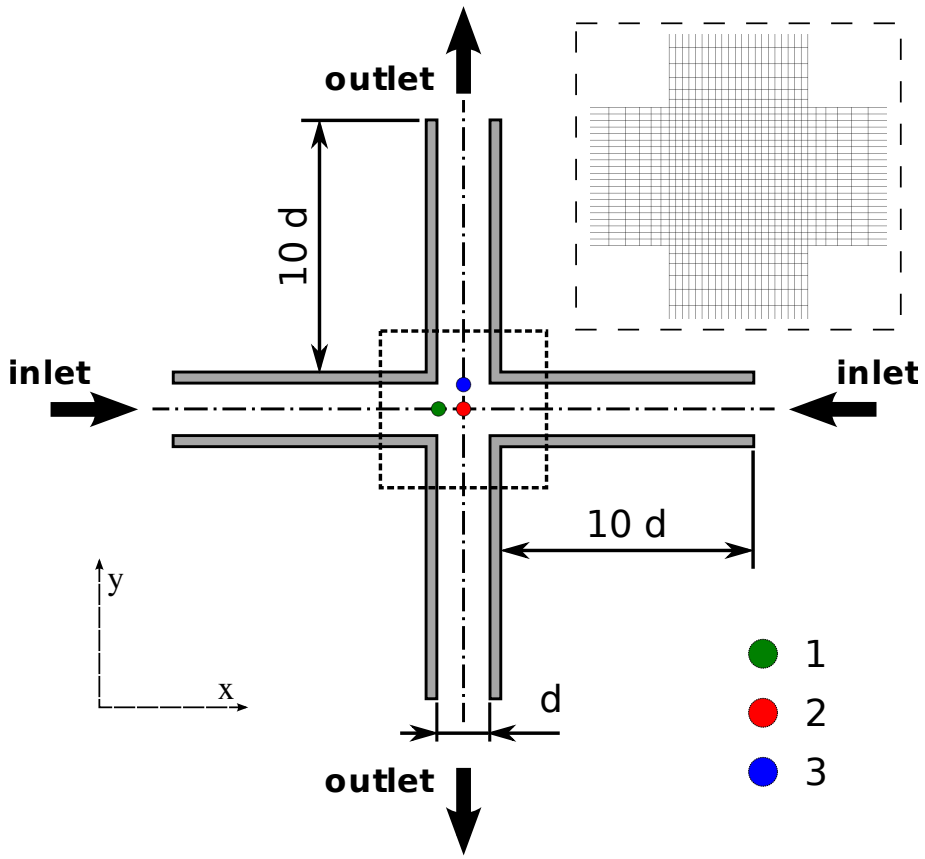

Figure 4.2 – Schematic of the cross-slot geometry. The dotted square is the area where the analyses were conducted, with the three dots indicating our main probes. The upper right dashed square shows a magnified view of this area and provides an illustration of a mesh refining towards the centre of the setup – here, the $M20$ mesh (see Tab. 4.1); note that the meshes used in the simulations were at least twice finer in each direction than $M20$ mesh.

The global mesh adopted for the numerical integration is composed of four blocks, each of which corresponding to an arm, with increased density of grid points when approaching the centre of the system, plus a central square with the smallest and uniform grid size. The mesh refinement towards the centre in each arm is realised via a

geometric progression relation with specific stretching factors, defined as:

$$\begin{cases} \Delta x_i = f_s \cdot \Delta x_{i-1} & \text{in } x\text{–direction} \\ \Delta y_i = f_s \cdot \Delta y_{i-1} & \text{in } y\text{–direction} \end{cases} . \tag{4.3}$$

The stretching factor f_s is determined maintaining a geometric progression for the mesh length, starting from the first cell near to the inlet or outlet boundary and finishing with the first cell in the central square. Equation 4.4 is used to implicitly calculate this index (see Appendix C for details on its derivation),

$$\frac{1 - {f_s}^N}{1 - f_s} = A_r \cdot N \cdot {f_s}^N , \tag{4.4}$$

where A_r represents the arm length-to-width aspect ratio and N is the number of cells in the central square region, which matches the number of elements in the cross-slot arm, in the direction of refinement.

The reference mesh configuration adopted for the results exposed in Chapter 5 (unless otherwise stated) is highlighted in Tab. 4.1 and includes a total of 12801 computational cells, corresponding to 51×51 cells in the central square, a minimal grid spacing $\Delta x_{min} = \Delta y_{min} \approx 0.02\,d$ in that same region and $f_s = 0.931$. In order to verify the robustness of our results, some calculations, and particularly those related to the instabilities thresholds, were repeated with multiple mesh sizes, including more refined meshes. The results were qualitatively independent of the mesh refinement and only slight differences in the values of the critical parameters were found (this topic will be more extensively addressed in Chapter 5).

The main parameters for all the meshes considered in this work are presented in Tab. 4.1, including the designation of the mesh, number of cells in the central square (along the x– and y–directions) and the total number of cells in the computational domain. For each case, an odd number of cells in the central square and along the arms width is adopted, allowing the direct calculation of the variables in the cross-slot centrelines. Two other parameters are also provided in Tab. 4.1: the approximate minimum cell size (identical in both directions, normalised by the width d and represented by Δx_{min} and Δy_{min}) as well as the stretching factors f_s. Note that the mesh is not refined in the direction normal to the walls.

A uniform velocity profile of amplitude U_b is applied at both inlets, where a homogeneous Neumann (zero gradient) boundary condition is specified for the pressure field, whereas polymeric extra-stresses are set to zero. At the outlets, a homogeneous Dirichlet (zero value) boundary condition is imposed for pressure, as well as zero-gradient ones for velocity and extra-stress fields. At the walls, a no-slip condition ($\boldsymbol{u} = \boldsymbol{0}$) is applied to the velocity field and a linear extrapolation technique is adopted for the extra-stresses [138]. The velocity and stress initial conditions correspond to no flow.

Cross-slot computational meshes

Mesh	N_x x N_y (cent. sq.)	f_s	Number of cells	$\Delta x_{min} = \Delta y_{min}$
$M20$	21×21	0.8395	2121	0.05
$M40$	41×41	0.9149	8241	0.025
$\boldsymbol{M50}$	$\mathbf{51 \times 51}$	**0.9311**	**12801**	**0.02**
$M60$	61×61	0.9422	18361	≈ 0.017
$M80$	81×81	0.9562	32481	≈ 0.013
$M100$	101×101	0.9647	50601	0.01
$M150$	151×151	0.9763	113401	≈ 0.007
$M200$	201×201	0.9821	201201	0.005

Table 4.1 – General parameters of cross-slot meshes.

Chapter 5

Numerical results on highly elastic cross-slot flows

A comprehensive numerical characterisation of viscoelastic inertialess fluid flows through a two-dimensional cross-slot is reported in this Chapter[1]. In our studies we integrate the equations displayed in Subsection 4.2.1 by means of the open-source numerical solver rheoTool® [138], which was developed in the framework of the OpenFOAM® CFD software [139]. This robust viscoelastic solver exhibits sophisticated and crucial features that allow satisfactory control of the numerical instabilities associated with large Weissenberg numbers (see Section 1.4). We remark that no polymer stress-diffusion is included (see Subsection 1.4.1 for details on that methodology).

The Weissenberg number $Wi = \lambda U_b/d$ was varied here by changing the fluid relaxation time λ only; the polymer concentration (inversely proportional to $\beta = \eta_s/\eta_t$) was set by choosing η_s and η_p such that their sum η_t is constant. As specified in Subsection 4.2.1, the Reynolds number $Re = \rho U_b d/\eta_t$ was kept fixed at $Re = 0$ for all the simulations in the present Chapter. However, we have checked that the results did not strongly depend on it by performing some calculations at $Re = 0.1$ (in simulations with the inertial term reinserted, retrieving Eq. 1.8).

5.1 Convergence of the numerical methods

In a preliminary step, we verify the order of accuracy of the numerical methods employed by the OpenFOAM® software, both in space and time. For this purpose, we define the benchmark variable Wi_0, that expresses a local Weissenberg number at the fixed location $\boldsymbol{x} = \boldsymbol{x}_*^{(2)}$, corresponding to the geometrical centre of the cross-slot

[1] Some parts of this Chapter are under revision for publication in *Europhysics Letters* (EPL), with co-authors G. Mompean and S. Berti [191]

(probe 2). The definition adopted here is the same as in the work of Cruz et al. [137] and is calculated using the strain rate $\dot{\varepsilon}_0$ at the stagnation point,

$$Wi_0 = \lambda\,\dot{\varepsilon}_0 = \lambda\sqrt{\left(\left.\frac{\partial u}{\partial x}\right|_0\right)^2 + \left.\frac{\partial u}{\partial y}\right|_0 \left.\frac{\partial v}{\partial x}\right|_0}. \tag{5.1}$$

We consider here a steady, laminar flow with $\beta = 1/9$ and $Wi = 0.1$, which was verified as corresponding to an elasticity level below critical Weissenberg for instabilities in this setup (as the flow in Fig. 5.4a). The order of spatial convergence for the HRS CUBISTA is then evaluated for the benchmark variable in Eq. 5.1, by calculating the relative error for multiple mesh sizes in comparison to a highly refined reference spacing, the $M200$ mesh. In Tab. 4.1, we can see some parameters for each grid considered. For finer spatial grids, we observe in Fig. 5.1 a convergence order of ≈ 2, which is the expected output for the discretisation scheme selected.

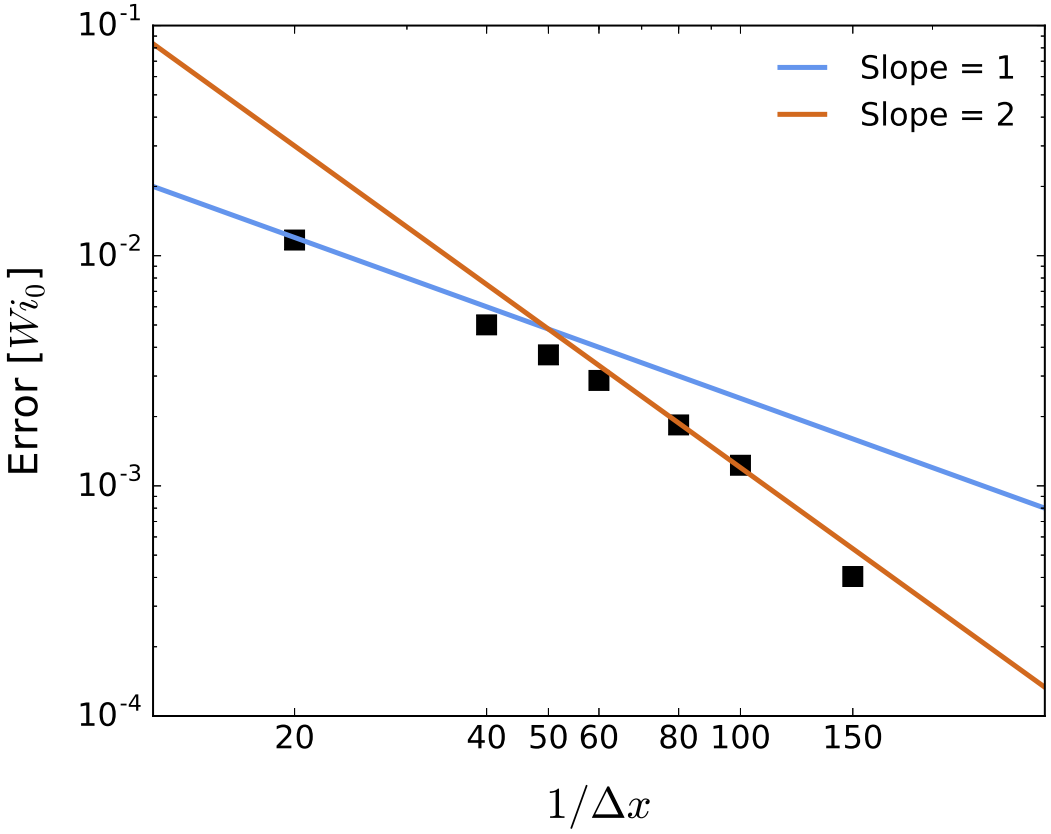

Figure 5.1 – Relative error in the calculation of the local Weissenberg number at the cross-slot centre vs inverse minimum grid spacing, for $\beta = 1/9$ and $Wi = 0.1$. The blue and brown solid lines are power-law curves, with logarithmic slopes equal to 1 and 2, respectively.

The order of temporal accuracy is equally investigated, using the same setup and similar flow parameters. We selected for this analysis a mesh with a substantial refinement ($M100$ mesh), so we can minimise the effects of the numerical errors due to the

spatial resolution while assessing the order of convergence of the time discretisation. A small dimensionless time step of $\Delta t = 10^{-6}$ is adopted as the reference for the calculation of the temporal relative error and we can remark in Fig. 5.2 a convergence order of ≈ 1 for the time discretisation scheme employed, the first-order (implicit) backward Euler scheme. Similar results were reported in the work of Pimenta and Alves [138] on the determination of the OpenFOAM® spatial and temporal accuracy, using different geometries and benchmark variables.

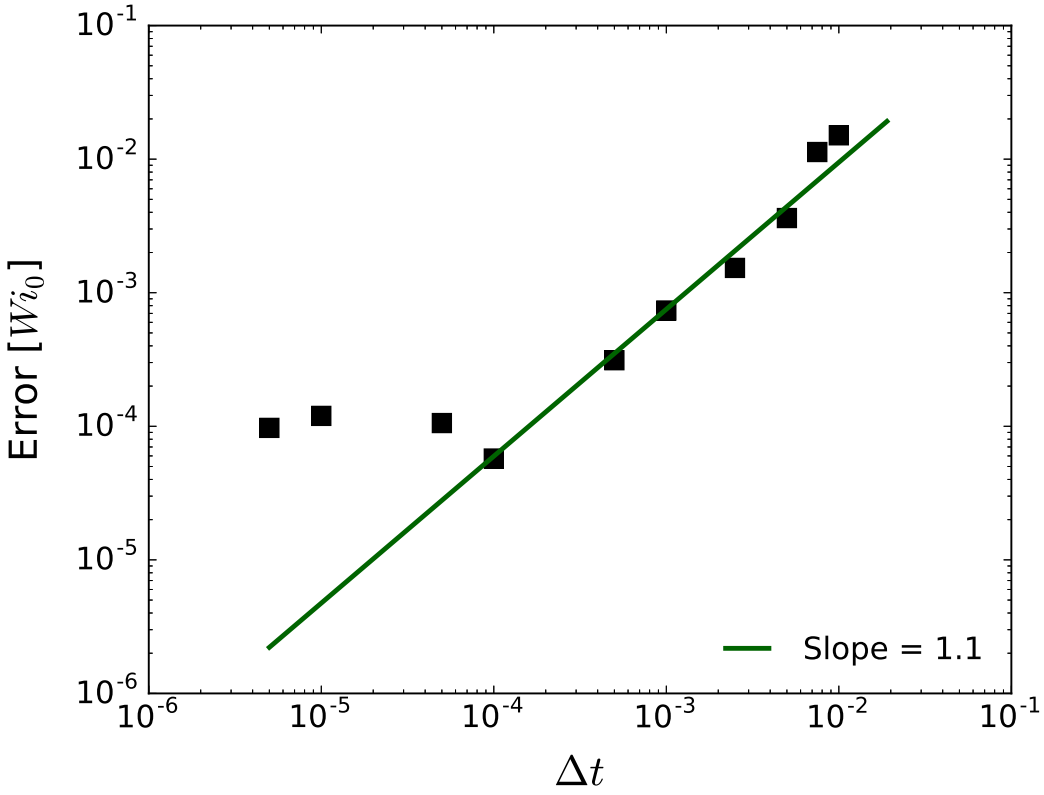

Figure 5.2 – Relative error in the calculation of Wi_0 vs the dimensionless time step Δt, for $\beta = 1/9$, $Wi = 0.1$ and $M100$ mesh. The green solid line is a power-law function with logarithmic slope equal to 1.1.

5.1.1 Time step evaluation

To identify possible issues related to the time step size, several analyses in that direction were carried out, though not exhaustively shown here. We investigated the influence of the time step not only for the low-elasticity, laminar flows already introduced, but also for the varied flow configurations presented later in this Chapter. The OpenFOAM® code adopts the definition of an appropriate dimensionless quantity for controlling time steps, the *Courant number* (C), as displayed in Eq. 5.2. In order to achieve numerical stability and temporal accuracy, the well-known CFL condition must be fulfilled, which states that a Courant number smaller than some value, for the entire domain, is required,

$$C = \frac{|\mathbf{u}|\,\Delta t}{\Delta x} \leq C_{max}\,, \tag{5.2}$$

where $|\mathbf{u}|$ represents the magnitude of the velocity through a given cell, Δt is the time step, Δx stands for the minimum cell size and C_{max} is the maximum allowed Courant number.

Typically, the maximum Courant number for an explicit time integration is $C_{max} = 1$, but several specifications in the numerical methods can modify this constant. For a result to be reliable, the steady flow conditions must be independent of the time step chosen and we attempted to verify this property for many different flow cases. We show one selected result in Fig. 5.3, *i.e.* the evolution in time of the magnitude of the velocity at the central stagnation point – as it should numerically approach zero – for four different C_{max} values. Note that indeed, the converged results for a steady-state flow do not depend on the CFL condition adopted.

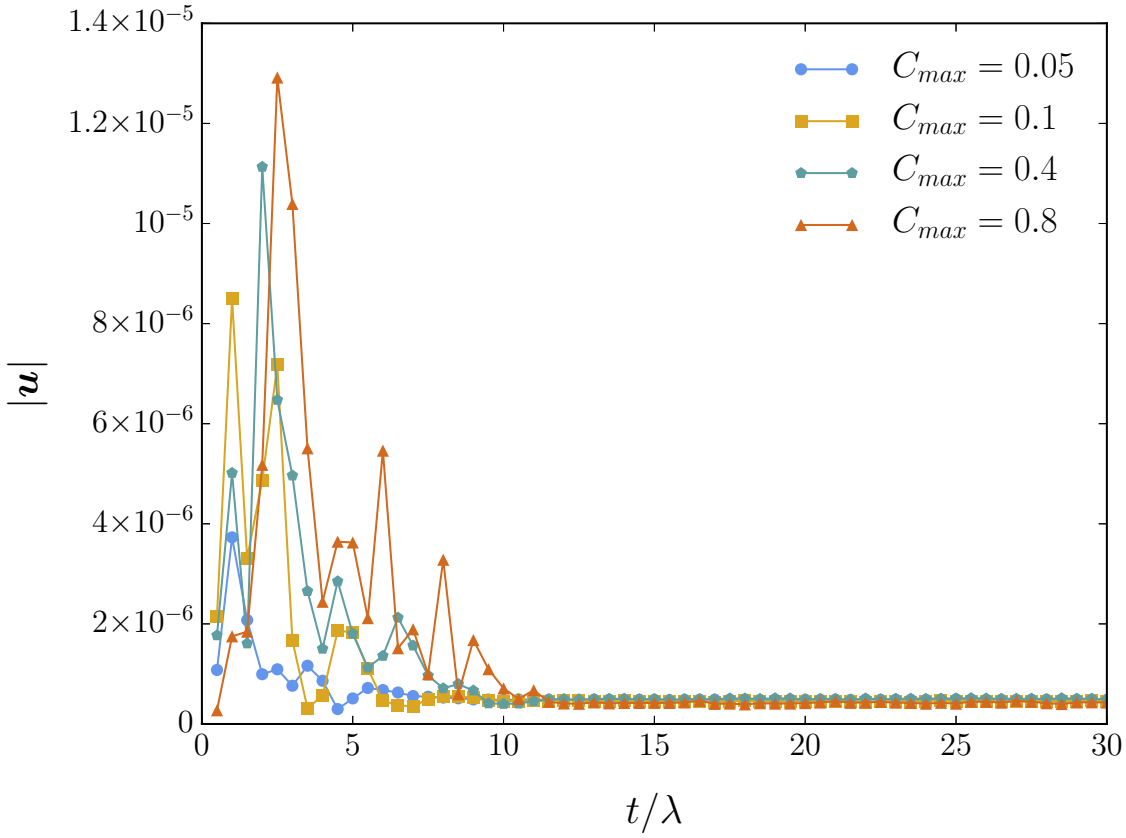

Figure 5.3 – Convergence of the velocity magnitude at the geometrical central point $|\boldsymbol{u}(\boldsymbol{x}_*^{(2)}, t)|$, for $C_{max} = 0.05, 0.1, 0.4, 0.8$, at $\beta = 8/9$ and $Wi = 2$.

Based on our findings, we decided to fix the CFL condition at $C_{max} = 0.1$ for all the results hereafter exposed, which revealed itself to be a good compromise between numerical accuracy and size of the simulations; time steps will thus change from case to case and be run-time variable, but in our studies they remained roughly at $\Delta t \sim 10^{-4}$.

5.2 First instability: an asymmetric bifurcation

When increasing the elasticity of the solution, while keeping the viscosity ratio fixed, in our numerical integrations, we observe a destabilisation of the flow, in agreement with previous studies reported in the literature for fixed β [136, 158]. The sequence of flow states that are selected strongly depends on the polymer concentration, however. We provide here a full picture of that dynamics, in the form of an original stability portrait of the system, as a function of both β and Wi. Let us preliminarily remark that below the onset of purely elastic instabilities, the flow coming from each of the inlets splits into two streams of equal flow rate, a symmetric state, at the outlets (see Fig. 5.4a).

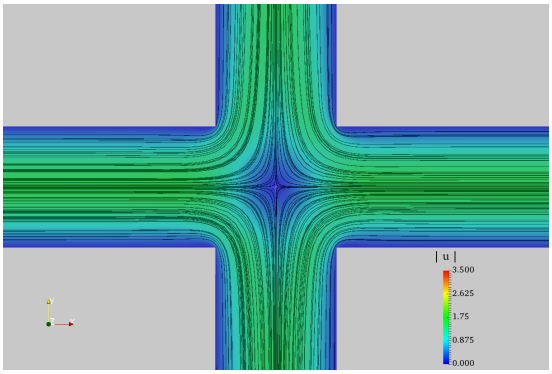

(a) $Wi = 0.35$

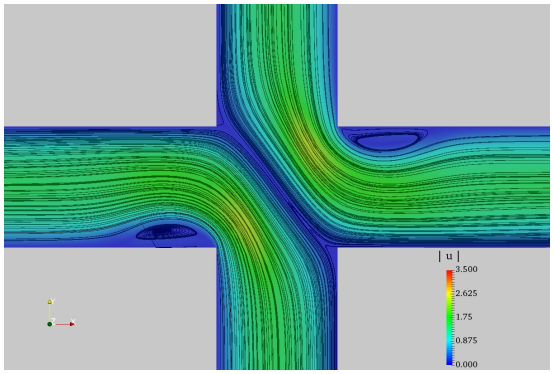

(b) $Wi = 1.48$

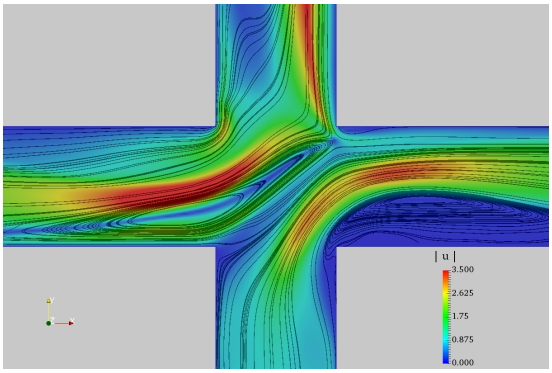

(c) $Wi = 10$

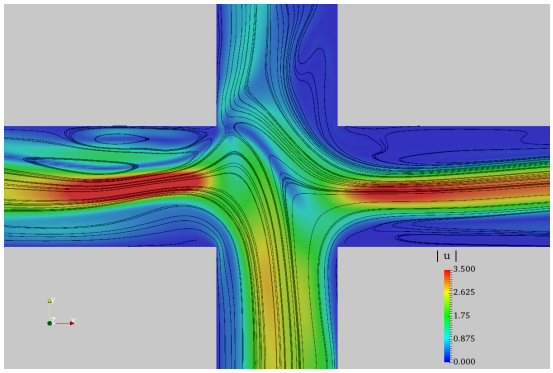

(d) $Wi = 20$

Figure 5.4 – Snapshots of the magnitude of the velocity field (colour) and flow streamlines (black lines) for $\beta = 1/9$. Increasing Wi, different regimes are observed: steady symmetric (a), steady asymmetric (b), unsteady disordered flow (c, d).

For concentrated solutions ($\beta \lesssim 0.56$), the flow first transitions to a steady asymmetric state (Fig. 5.4b, where $\beta = 1/9$) and it is possible to measure quantitatively the degree of the asymmetry as the bifurcation develops, for progressively higher Wi. An *asymmetric flow parameter* (Q_a) is proposed, in the same way as done by Poole et al. [136], following:

$$Q_a = 1 - \frac{2\,Q_{out}}{Q_{in}}, \tag{5.3}$$

where Q_{in} stands for the flow rate supplied to each inlet and Q_{out} is the flow rate exiting by a selected outflow arm. It expresses the amount of flow that takes an opposite direction from that it would take in a fully symmetric case. In Fig. 5.5, we plot the calculated value of Q_a for several Wi near the critical Weissenberg number for the transition between steady symmetric and asymmetric regimes; the curves have been drawn for viscosity ratios of $\beta = 1/9$ and $1/3$ and are mirrored with respect to the axis $Q_a = 0$, to indicate that both stable equilibrium states are considered. We confirmed that the evolution of Q_a with Wi, after the transition point, follows a square-root behaviour as in Eq. 5.4, which is compatible with a supercritical pitchfork bifurcation. Indeed, transitions via a pitchfork bifurcation are common in physical problems that present a symmetry [192].

$$Q_a \approx A\sqrt{Wi - Wi_c^{(\mathrm{I})}}, \tag{5.4}$$

where A stands for a scale parameter and $Wi_c^{(\mathrm{I})}$ is the critical Wi for such a steady instability. Fitting curves following Eq. 5.4 are included in Fig. 5.5 (dashed lines on both panels). The critical Weissenberg number – at which the bifurcation is at first observed – and the scaling parameter A can thus be determined by the curve fitting; our value of $Wi_c^{(\mathrm{I})}$ for $\beta = 1/9$ is in good agreement with that reported in a previous benchmark study [137] (relative difference of less than 5%).

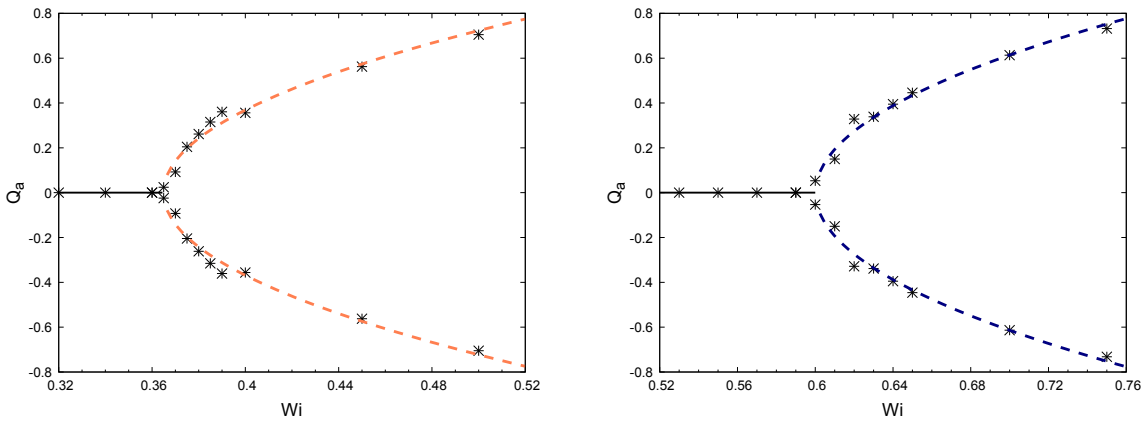

(a) $\beta = 1/9$ (b) $\beta = 1/3$

Figure 5.5 – Flow parameter Q_a vs Wi near the onset of steady asymmetric flow, for two different values of β, illustrating a supercritical pitchfork bifurcation in both cases; here $A \simeq 1.97$ and $Wi_c^{(\mathrm{I})} \simeq 0.36$ for $\beta = 1/9$; and $A \simeq 1.94$ and $Wi_c^{(\mathrm{I})} \simeq 0.60$ for $\beta = 1/3$.

The situation changes for more diluted solutions (*i.e.* when $\beta \gtrsim 0.56$). Indeed, in this case, the steady asymmetric flow regime does not set in and a direct change from steady symmetric to unsteady flow is observed. Remarkably, the same qualitative phenomenology is also found in experiments in micro-scale devices [159].

5.3 Second instability: time-dependent behaviour

Further increase of the flow elasticity, corresponding to higher Wi at fixed β, eventually leads to the onset of time-dependent behaviour. It arises initially as regular and periodic oscillations of the asymmetric flow pattern, which stays similar to that of Fig. 5.4b. We remind that, in the range of low β values, the former manifests as a second instability, when Wi is increased beyond a second threshold value close to 1.5; for $\beta \gtrsim 0.56$, however, it corresponds to the first and unique instability, which happens at progressively higher Wi.

Our analysis here is based on the measurement of time series of velocity and stress components at three different positions, marked as probe 1 ($\boldsymbol{x}_*^{(1)}$, entrance), probe 2 ($\boldsymbol{x}_*^{(2)}$, centre) and probe 3 ($\boldsymbol{x}_*^{(3)}$, exit) (see Fig. 4.2), over long durations corresponding to 1000λ. We note that an initial transient with a duration of 100λ was removed from every time series in the post-processing of the numerical results, to avoid taking into account irrelevant data for the statistics.

We report in Fig. 5.6 the onset of time-dependency, by presenting the behaviour of the magnitude of the velocity $|\boldsymbol{u}(\boldsymbol{x}_*^{(3)}, t)|$ at the exit probe, for two different β (representing a concentrated and a dilute solution). Remark that, for these temporal series, only a small subset of the data record is shown.

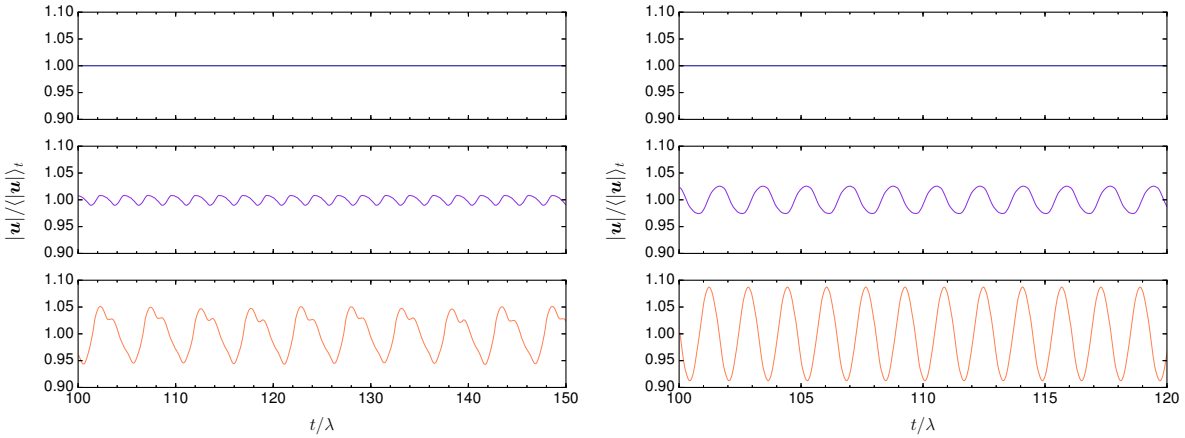

(a) $\beta = 1/9$ (b) $\beta = 2/3$

Figure 5.6 – Temporal evolution (small subset of the total data set, see text) of the magnitude of velocity at the outlet (probe 3), normalised by its time average over the whole time series, after the initial transient, for (a) $Wi = 0.3, 1.55, 1.7$ and (b) $Wi = 2, 2.5, 3$ (from top to bottom in each panel).

By measuring the amplitude and frequency of the time series of $|\boldsymbol{u}(\boldsymbol{x}_*^{(3)}, t)|$ at the fixed location $\boldsymbol{x}_*^{(3)}$ for Wi close to the onset of the unsteady regime and for different concentration values, we could assess that the second instability is a supercritical Hopf bifurcation (see Fig. 5.7, for $\beta = 1/9$ and $2/3$), as also suggested by Xi and Graham [73] using a FENE-P model at non-zero Re and larger β. Indeed, the velocity signal displays

a growth of its amplitude that is fairly well described by $(Wi - Wi_c^{(II)})^{1/2}$, with $Wi_c^{(II)}$ the critical Weissenberg number, and an approximately linear decrease of its frequency with Wi (close to the transition).

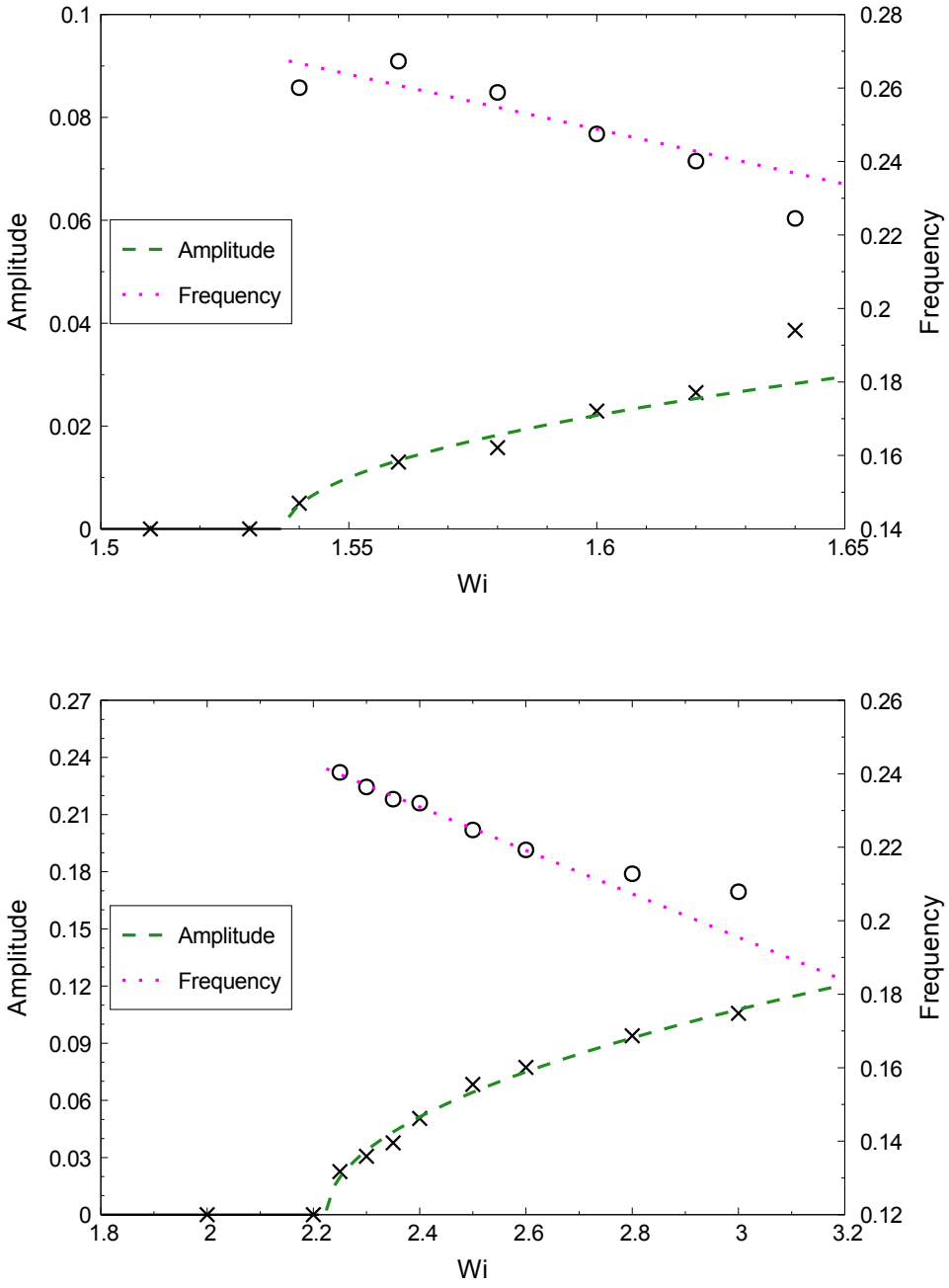

Figure 5.7 – Amplitude and frequency of the oscillations of $|\boldsymbol{u}(\boldsymbol{x}_*^{(3)}, t)|$ vs Wi at the onset of time-dependent flow, evidencing transitions via a supercritical Hopf bifurcation; here $Wi_c^{(II)} \simeq 1.54$, for $\beta = 1/9$ (top panel) and $Wi_c^{(II)} \simeq 2.22$, for $\beta = 2/3$ (bottom panel).

In the time-dependent regime, and particularly for low β, an increase of Wi eventually gives rise to spatially and temporally more complex flows akin to elastic turbulence ones. Two illustrative examples, at fixed time, are shown in Figs. 5.4c and 5.4d, for $\beta = 1/9$ and two different values of Wi.

5.4 Influence of polymer concentration on flow states

The complete stability portrait, obtained by spanning the (β, Wi) plane with a large number of simulations, is shown in Fig. 5.8, where the different point types correspond to the different dynamical regimes observed. The green squares, blue diamonds and red dots respectively correspond to steady symmetric, steady asymmetric and unsteady flow; here, we only show a limited subset of the results from the simulations performed.

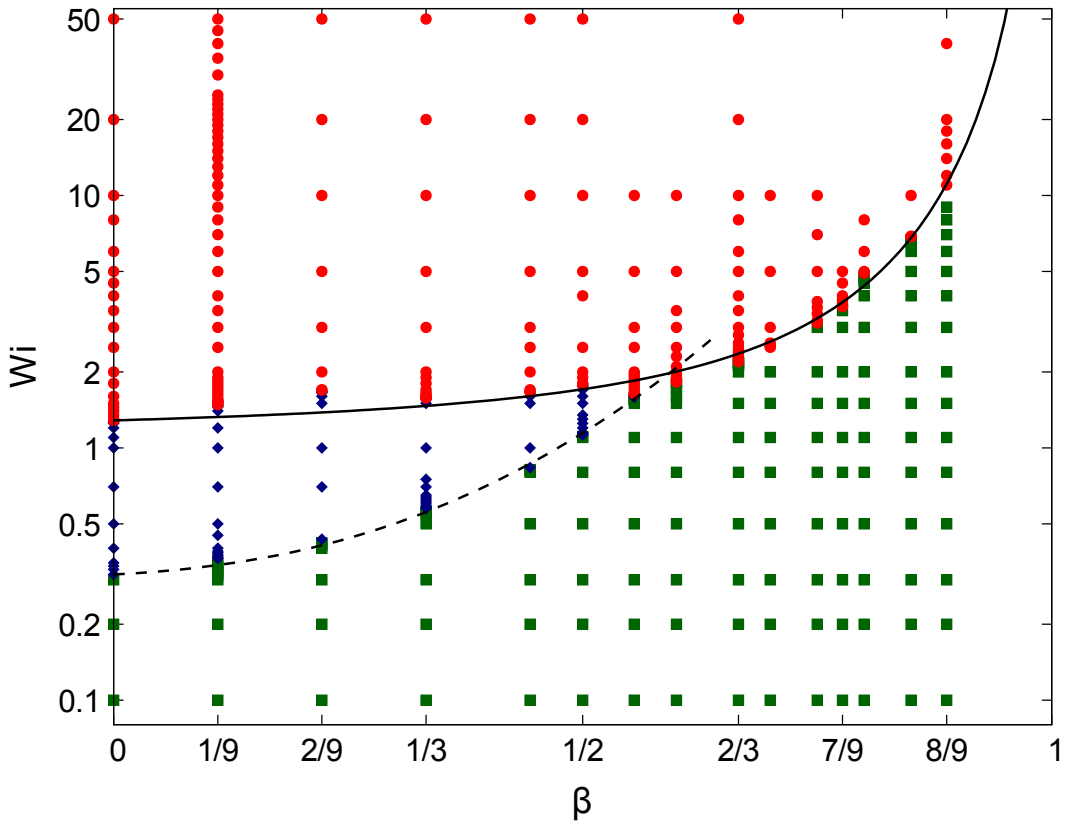

Figure 5.8 – Stability diagram in the (β, Wi) plane at $Re = 0$. The green squares, blue diamonds and red dots respectively correspond to steady symmetric, steady asymmetric and unsteady flow. Computations were performed in the $M50$ mesh. The dashed ($Wi_c^{(\mathrm{I})}$) and continuous ($Wi_c^{(\mathrm{II})}$) lines are fits using Eq. 5.5; here $a_0^{(\mathrm{I})} \simeq 2.75$, $a_{-1}^{(\mathrm{I})} \simeq -3.94$, $a_0^{(\mathrm{II})} \simeq 0.85$, $a_{-1}^{(\mathrm{II})} \simeq 0.05$.

Recalling the definitions of $Wi_c^{(\mathrm{I})}$ and $Wi_c^{(\mathrm{II})}$ as the critical Wi for the first and second cross-slot instabilities, we observe that they both lead to higher Wi_c with growing β, which is reasonable since increasing β corresponds to decreasing polymer concentration. The faster growth of $Wi_c^{(\mathrm{I})}(\beta)$ causes the shrinking of the region of steady asymmetric flow (see Fig. 5.8). Nevertheless, the determination of the functional dependencies $Wi_c^{(i)}(\beta)$ (with $i = \mathrm{I}, \mathrm{II}$) from stability analysis is not an easy task. This difficulty is due to the formation of a *birefringent strand* (*i.e.* a narrow and elongated band where polymers molecules are highly stretched, and which displays particular optical properties in

experiments [160]) and of a diverging base state associated with the infinite extensibility of polymers [161].

Since here we are mainly interested in characterising the boundaries, in the (β, Wi) plane, of the regions where elastic turbulence could be excited, we proceed heuristically, especially focusing on $Wi_c^{(\mathrm{II})}(\beta)$. In order to account for non-zero β effects, we conjecture that $Wi_c^{(\mathrm{II})}(\beta) = Wi_c^{(\mathrm{II})}(0) f(\beta)$, where $f(\beta)$ is a positive analytic function, except for $\beta \to 1$ where a divergence is expected, since the fluid becomes Newtonian and no purely elastic instability should occur; clearly $f(0) = 1$. Our numerical results suggest that the data are compatible with a Laurent expansion at second order around the point $\beta = 1$. Somehow more surprisingly, we find that the same functional shape can also be used to fit the $Wi_c^{(\mathrm{I})}(\beta)$ data, indicating that:

$$Wi_c^{(i)} = Wi_c^{(i)}(0)\left[a_0^{(i)} + \frac{a_{-1}^{(i)}}{1-\beta} + \frac{a_{-2}^{(i)}}{(1-\beta)^2}\right], \tag{5.5}$$

where $a_{-2}^{(i)} = 1 - a_0^{(i)} - a_{-1}^{(i)}$ using the constraint $f(0) = 1$, and $i = \mathrm{I}, \mathrm{II}$. According to Fig. 5.8, for $\beta = 0$ both instabilities arise and the critical Wi for the transitions can thus be directly determined. Indeed, we have $Wi_c^{(\mathrm{I,II})}(0) = (0.315, 1.285) \pm 0.005$. Further details on the dynamics of the instabilities for zero-viscosity-ratio flows are given in Section 5.6.

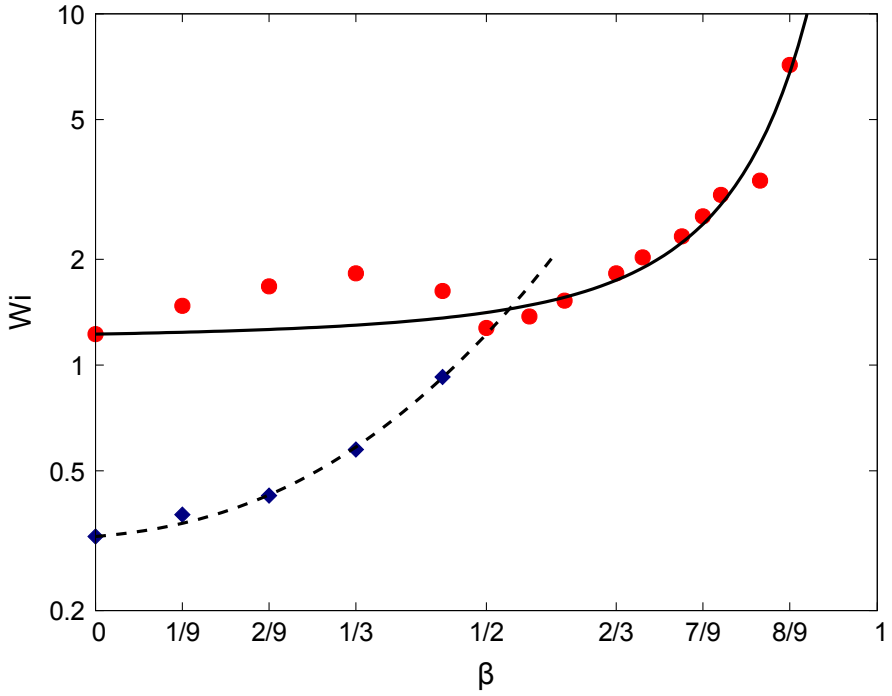

Figure 5.9 – Stability diagram in the (β, Wi) plane for a mesh twice as refined ($M100$ mesh). For this diagram, the blue diamonds and red dots now represent the critical Wi for the transitions to steady asymmetric and unsteady flow, respectively. The dashed ($Wi_c^{(\mathrm{I})}$) and continuous ($Wi_c^{(\mathrm{II})}$) lines are fits using the same Eq. 5.5; here $a_0^{(\mathrm{I})} \simeq 2.90$, $a_{-1}^{(\mathrm{I})} \simeq -4.23$, $a_0^{(\mathrm{II})} \simeq 0.97$, $a_{-1}^{(\mathrm{II})} \simeq -0.03$.

In Fig. 5.8 we report a comparison between fits with function 5.5 (dashed and continuous lines for $i = \mathrm{I}, \mathrm{II}$, respectively) and the numerical data; the agreement is rather good for both instability types, confirming our conjecture.

To conclude this discussion, we mention that in our calculations with a grid two times more refined (for which a similar stability diagram is depicted in Fig. 5.9) or at $Re = 0.1$ (not shown here), we did not observe any qualitative difference in the dynamical regimes occurring for different values of β and Wi. We report a slight quantitative deviation of the functional dependency of $Wi_c^{(\mathrm{II})}$ on β (regarding our conjecture, explicitly stated by Eq. 5.5), for concentrated polymer solutions in simulations with the highly refined $M100$ mesh. We suggest that the relatively short duration of our simulations, due to their prohibitive size for such a mesh refinement level, might be the source of the discrepancy. Fully addressing this question, however, requires deeper analyses.

5.5 Transition to the regime of elastic turbulence

We now consider the transition to turbulent-like flow. In the following, we will present the results of the analysis performed adopting the $M50$ mesh for increasing Wi, at a fixed $\beta = 1/9$. Notwithstanding some quantitative differences, the phenomenology holds similar in the whole range ($\beta \lesssim 0.56$) of concentrated solutions, including for UCM ($\beta = 0$, whose results are addressed in Section 5.6). In the case of more diluted solutions, although we observed some hints of the onset of irregular flow, we could not reach a fully developed regime and we cannot conclude about the emergence of elastic turbulence. Notice that for such large values of β, the critical Weissenberg number $Wi_c^{(\mathrm{II})}$ grows very rapidly, making the simulations more and more delicate.

As for the experiments reported in the work of Sousa et al. [20], we choose to mainly focus on the axial component $u_y(\boldsymbol{x}_*^{(3)}, t)$ at the exit probe, whose behaviour is presented in Fig. 5.10 for several values of Wi. Again, only a subset of the complete time series is displayed here.

The spectra of $u_y(\boldsymbol{x}_*^{(3)}, t)$ are shown in Fig. 5.11. All those corresponding to the developed regime are averages over 10 spectra computed from consecutive subintervals (of duration 100λ) of the velocity time series obtained for a given value of Wi (after the initial transient).

For $Wi \gtrsim Wi_c^{(\mathrm{II})}$, time-dependency manifests in the form of regular oscillations with a single frequency close to $0.4/\lambda$ (see top panel in Fig. 5.10 and inset of Fig. 5.11). At slightly higher Weissenberg number ($Wi = 3$, second panel from the top in Fig. 5.10) the flow is still periodic but it is now characterised by more discrete frequencies; correspondingly, the spectrum shows several distinct peaks associated with a fundamental frequency and some harmonics (inset of Fig. 5.11). The occurrence of a transitional periodic regime was also reported in different setups [14, 193]. Above $Wi \approx 5$, the flow

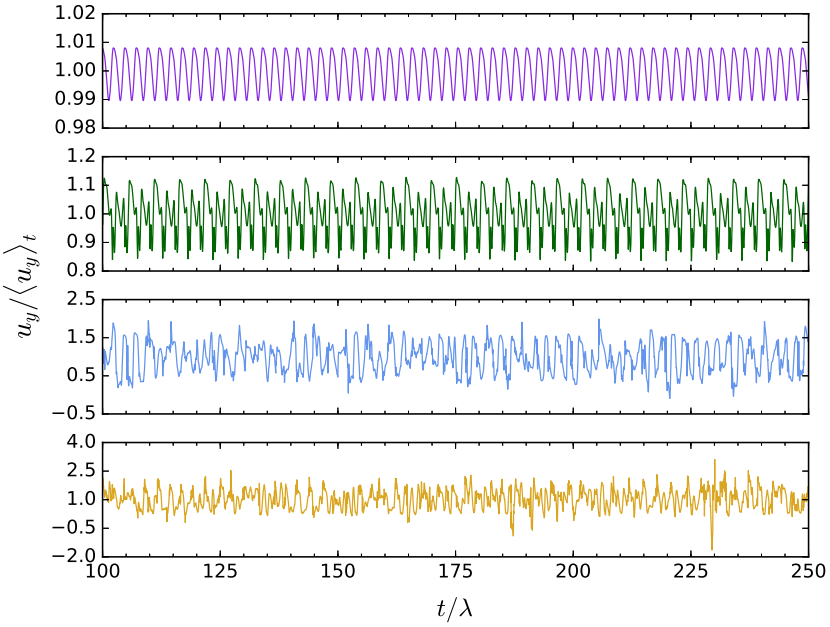

Figure 5.10 – Temporal evolution (subset of the total data set) of the y–component of velocity at the outlet, normalised by its time average over the whole time series, after the initial transient, for $\beta = 1/9$ and $Wi = 1.55, 3, 6, 12$ (from top to bottom).

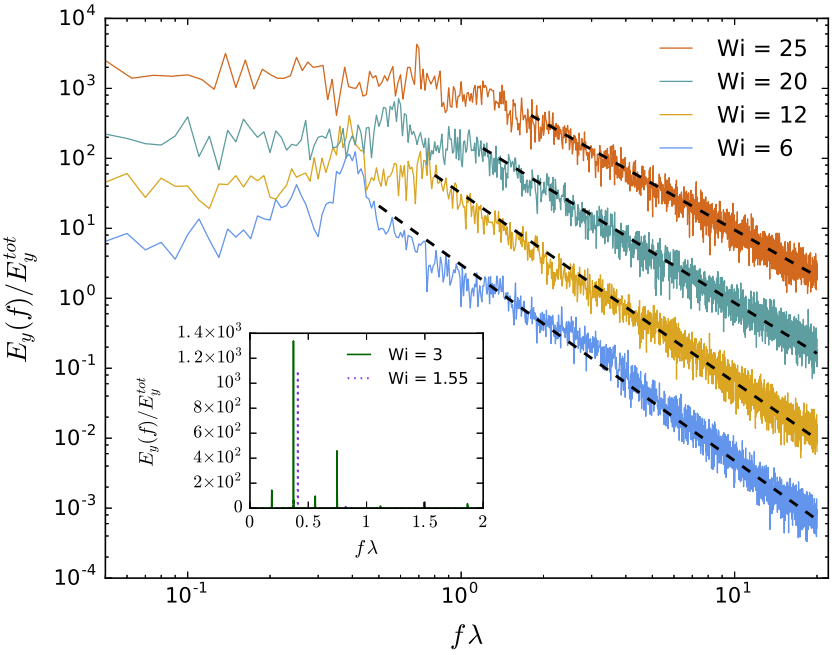

Figure 5.11 – Temporal spectra of fluctuations of the axial velocity component at the outlet $u_y(\boldsymbol{x}_*^{(3)}, t)$, normalised by their integral E_y^{tot} in the elastic turbulence regime for different values of Wi and $\beta = 1/9$; the curves have been vertically shifted to ease readability. The dashed black curves correspond to $E_y(f) \sim f^{-\delta}$, the exponents are $\delta \simeq (2.8, 2.7, 2.4, 2.2) \pm 0.4$ for $Wi = 6, 12, 20, 25$, respectively. Inset: spectra of fluctuations of $u_y(\boldsymbol{x}_*^{(3)}, t)$ in the unsteady flow regime at lower elasticity levels. For $Wi = 1.55$, *i.e.* just above the critical value $Wi_c^{(\mathrm{II})}$, the spectrum displays a single frequency peak; at larger $Wi = 3$ more discrete frequencies are present.

loses periodicity and the velocity spectra become continuous. Indeed, starting from $5 \lesssim Wi \lesssim 10$ they result to be quite well described by a power-law function (Fig. 5.11).

When elasticity is increased in the range $11 \lesssim Wi \lesssim 25$, the faster fluctuating behaviour of the flow is accompanied by quite wide and irregular oscillations, over longer durations. The flow now loses its spatial asymmetry to alternatively select the outlet in the positive/negative y–direction. Such a phenomenon has a strong impact on the statistics of the transversal velocity component $u_x(\boldsymbol{x}_*^{(3)}, t)$ at the outlet, whose fluctuations are accompanied by irregular jumps between two mean values of opposite sign, thus complicating their analysis.

We report qualitatively similar erratic jumps for the wall-normal velocity component $u_y(\boldsymbol{x}_*^{(1)}, t)$ at the inlet, whose behaviour is displayed in Fig. 5.12, for increasing Wi. Starting at $Wi \approx 11$ (top panel in Fig. 5.12), these irregular shifts of flow direction become more frequent with increasing elasticity. Eventually, around $20 \lesssim Wi \lesssim 25$, the two-state system ceases and the prior unsteady behaviour is re-established, featuring faster fluctuations only.

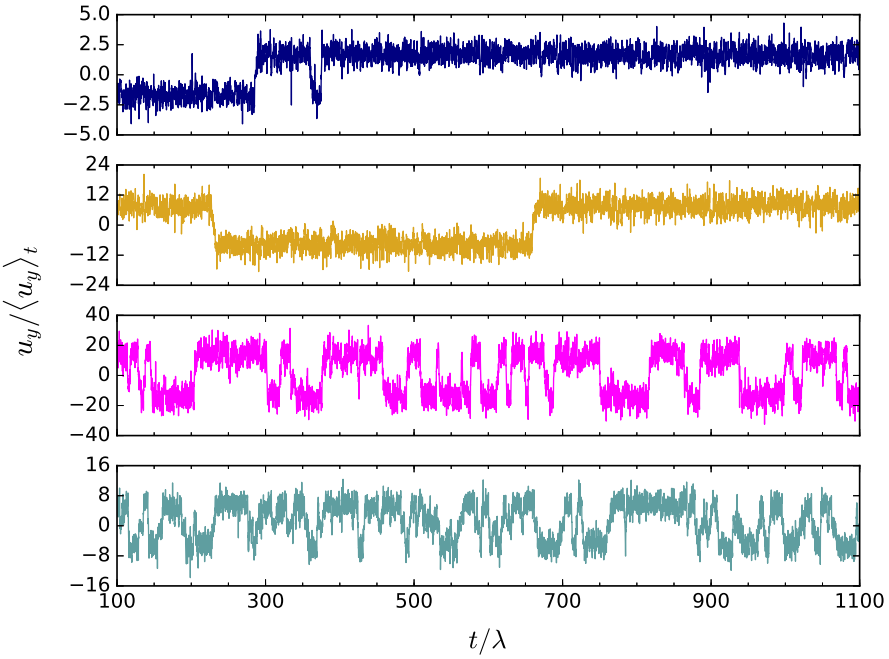

Figure 5.12 – Temporal evolution (full data set) of the y–component of velocity at the inlet probe, normalised by its time average over the whole time series, after the initial transient (represented by the $\langle\rangle_t$ operator), for $\beta = 1/9$ and $Wi = 11, 12, 15, 20$ (from top to bottom).

In the turbulent-like regime ($Wi \gtrsim 5$), the spectrum of velocity fluctuations displays a power-law behaviour $E_y(f) \sim f^{-\delta}$ beyond a frequency that, as in experimental studies [20], slightly increases with Wi. The absolute value of the spectral exponent is found to be in the range $2 \lesssim \delta \lesssim 3$ and shows some tendency to decrease at higher Wi; the latter feature is also detected in experiments [20, 167]. In particular, we find

$\delta \simeq (2.8, 2.7, 2.4, 2.2) \pm 0.4$ for $Wi = 6, 12, 20, 25$, respectively. The spectra are thus overall less steep than those previously found in experiments [9, 20] and those theoretically predicted assuming homogeneity and isotropy [180]. However, they bear an interesting similarity with those obtained in two-dimensional numerical simulations, without artificial polymer-stress diffusion, of Oldroyd-B model in the presence of a cellular forcing generating distinct regions of strain and vorticity [34].

A possible reason for the difference with the prediction of Fouxon and Lebedev [180] is the lack of the statistical symmetries assumed by the theory in the present case. Indeed, our flow is neither homogeneous (due to the presence of the walls, but also of the high-strain region close to the centre of the setup), nor fully isotropic, as we typically observe that $u_y^{rms} > u_x^{rms}$ for the root-mean-square (rms) velocity components (see Fig. 5.13 and its upper left inset, for a comparison at the exit probe). Moreover, it is shown in the upper right inset of Fig. 5.13 that the turbulent intensity $u^{rms}/\overline{u}$, here defined as the ratio of the rms to the mean value of the full velocity modulus $u \equiv |\boldsymbol{u}|$ (with the overbar denoting a temporal average), can quite easily exceed 0.5, and be as high as ≈ 0.8 in conjunction with the temporal oscillations of the spatial asymmetry of the flow.

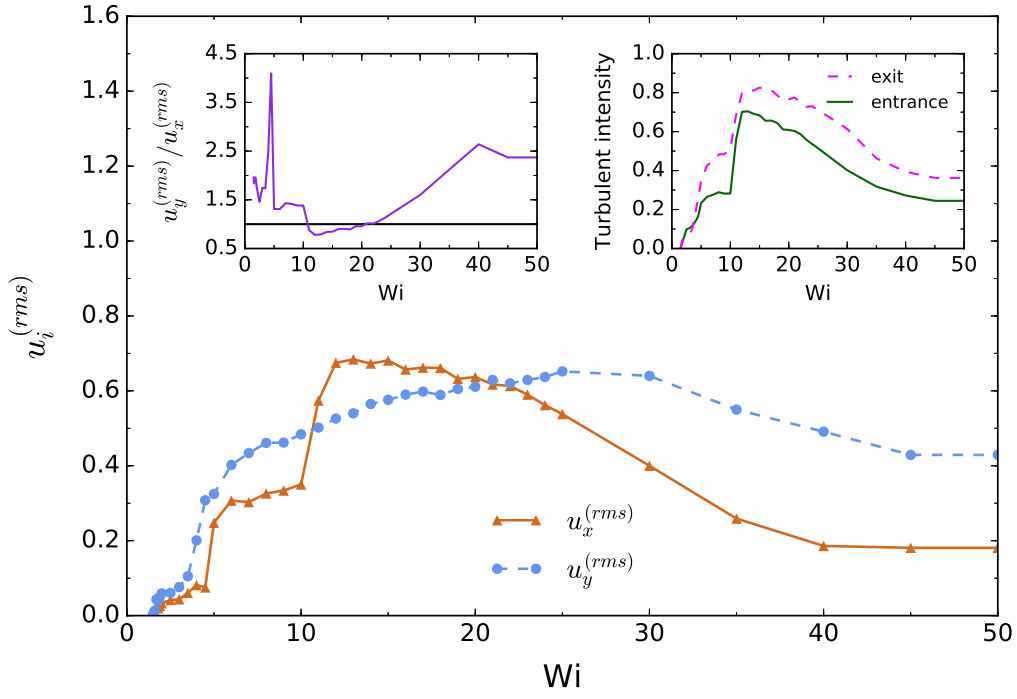

Figure 5.13 – Root-mean-square (rms) of both velocity components, $u_x(\boldsymbol{x}_*^{(3)}, t)$ (brown triangles) and $u_y(\boldsymbol{x}_*^{(3)}, t)$ (blue dots), at the outlet vs Wi. Left inset: Ratio of the rms of the axial to the transversal component of the velocity vs Wi. Right inset: Turbulent intensity (see text for its definition) vs Wi, for the exit (dashed magenta line) and entrance (solid green line) probes. Here we consider 38 different Wi from 1.5 to 50, for $\beta = 1/9$. We remark that general quantitative results for $Wi > 25$ should be taken with caution, as they may depend on the length of the inlet/outlet channels.

Therefore, the validity of Taylor's hypothesis [194, 195], allowing to convert spectra from the frequency to the wavenumber domain, appears questionable. It might be the case that its refined version could be applied, as in the work of Burghelea et al. [196], but addressing this question requires further investigations. Finally, although previous numerical studies in two dimensions have revealed that the spectral exponent of elastic turbulence seems to be quite insensitive to the space dimensionality [21, 96, 197], we cannot exclude that the 2D nature of our flow has an impact.

To further characterise the statistical properties of our elastic turbulent flows, we computed the probability density functions (pdf's) of the fluctuations of the velocities $u_{x,y}(\boldsymbol{x}_*^{(3)}, t)$, as well as of the local accelerations $\partial_t u_{x,y}(\boldsymbol{x}_*^{(3)}, t)$, obtained from the temporal signals at probe 3. The results are presented in Figs. 5.14 and 5.16, where all variables are rescaled with the corresponding standard deviation σ. The statistics of u_y fluctuations weakly deviate from a Gaussian behaviour, with small negative skewness for large enough Wi (Fig. 5.14a). Some deviation from Gaussianity was previously reported experimentally in elastic-turbulent flows [18].

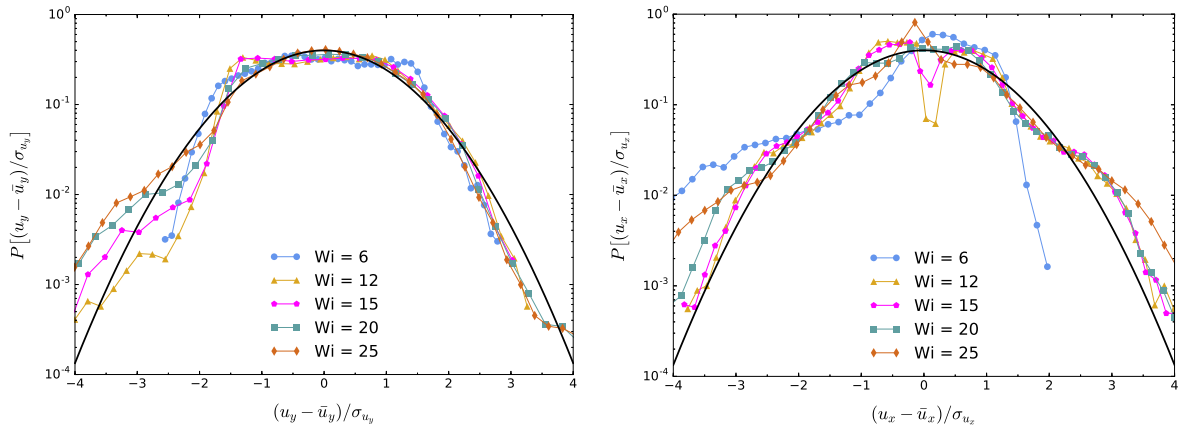

(a) (b)

Figure 5.14 – (a) Probability density functions of normalised velocity fluctuations $u_y' = (u_y - \overline{u_y})/\sigma_{u_y}$, where $u_y \equiv u_y(\boldsymbol{x}_*^{(3)}, t)$, the overbar denotes the temporal average and σ the standard deviation, for different values of Wi and $\beta = 1/9$; (b) pdf's of the same quantity along x–direction. In both panels the solid black lines are standard Gaussian pdf's.

The flow-asymmetry alternation events introduced before and developing for $11 \lesssim Wi \lesssim 25$ impact the pdf's of the fluctuations of the transversal velocity components at probes 1 and 3. Bimodal shapes are visible in Fig. 5.14b (in that range of elasticities) for $u_x(\boldsymbol{x}_*^{(3)}, t)$, though even more pronounced for the component $u_y(\boldsymbol{x}_*^{(1)}, t)$, shown in Fig. 5.15.

The statistics of fluctuations of the accelerations are remarkably less dependent on the Weissenberg number, the component of velocity and also the probe location,

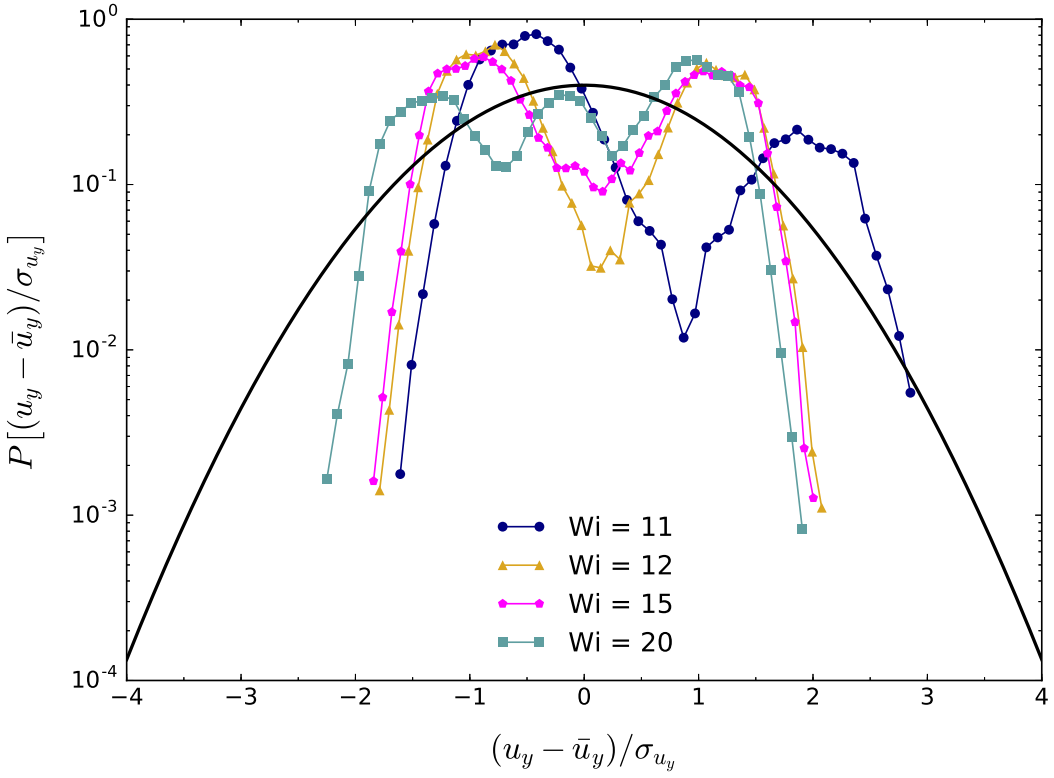

Figure 5.15 – Probability density functions of normalised velocity fluctuations $u'_y = (u_y - \overline{u_y})/\sigma_{u_y}$, where $u_y \equiv u_y(\boldsymbol{x}_*^{(1)}, t)$, the overbar denotes the temporal average and σ the standard deviation, for different values of Wi and $\beta = 1/9$.

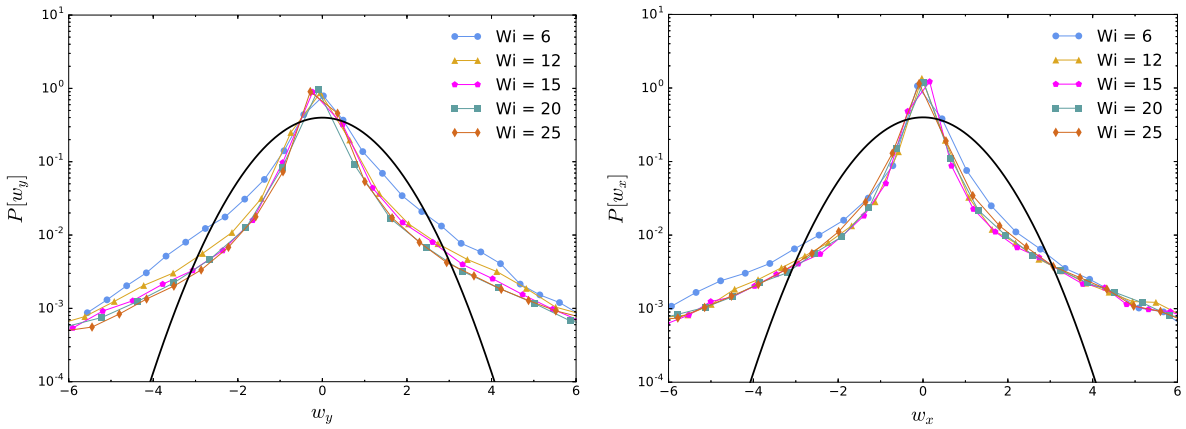

(a) (b)

Figure 5.16 – (a) Probability density functions of normalised temporal increments of velocity fluctuations $w_y = (\partial_t u_y - \overline{\partial_t u_y})/\sigma_{\partial_t u_y}$, where $u_y \equiv u_y(\boldsymbol{x}_*^{(3)}, t)$, the overbar denotes the temporal average and σ the standard deviation, for different values of Wi and $\beta = 1/9$; (b) pdf's of the same quantity along x–direction. In both panels the solid black lines are standard Gaussian pdf's.

suggesting a faster (with Wi) onset of scaling properties at small scales. As it can be seen in Fig. 5.16, the corresponding pdf's display high tails that are indicative of non-Gaussian statistics, as is typical in turbulent flows [198, 199] and as observed in elastic turbulence experiments [13] and random 3D flow of polymer solutions [200].

We conclude this Section by presenting some results concerning polymeric extra-stresses. In Fig. 5.17 we show a steep enhancement (with Wi) of the stretching of polymer molecules, represented by the time-averaged trace of the conformation tensor $\boldsymbol{c}$, as measured for probes 1 and 3. Furthermore, it was observed that the viscometric function N_1 pronouncedly decays in the stagnation point, for increasing Wi, after the onset of the time-dependency and up to $Wi \approx 10$ (see inset of Fig. 5.17); we recall that N_1 represents the first normal stress difference and, in order to be positive, is defined here as

$$N_1 = \tau_{yy} - \tau_{xx}, \tag{5.6}$$

where τ_{xx} and τ_{yy} are the two non-zero normal components of the extra-stress tensor $\boldsymbol{\tau}$.

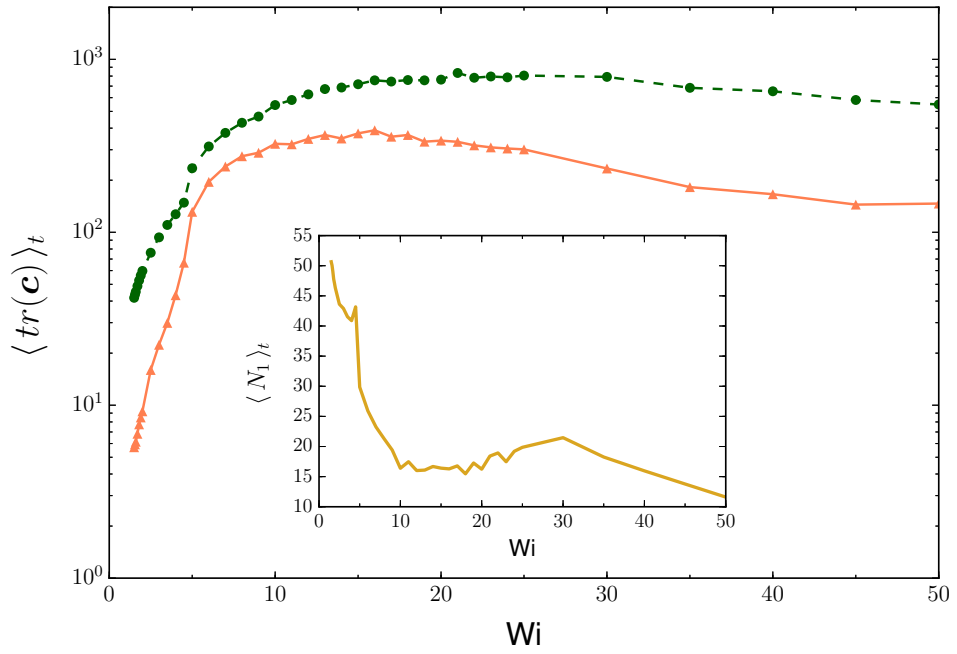

Figure 5.17 – Temporal average of $tr(\boldsymbol{c})$ vs Wi at fixed locations $\boldsymbol{x}_*^{(1)}$ (orange triangles) and $\boldsymbol{x}_*^{(3)}$ (green dots). Inset: Time-averaged first normal stress difference N_1 vs Wi at the fixed location $\boldsymbol{x}_*^{(2)}$; here we consider 38 different Wi from 1.5 to 50, for $\beta = 1/9$. Note that quantitative results for $Wi > 25$ should be taken with caution, as they may depend on the length of the inlet/outlet channels.

We report also a saturation of the polymer elongation and stresses far beyond $Wi_c^{(II)}$, in both cases occurring at about the same level of elasticity, *i.e.* at $Wi \approx 10$, for $\beta = 1/9$ (see Fig. 5.17 and its inset).

5.6 Comments on the UCM constitutive model

We remark that in the limit $\beta \to 0$ of the Oldroyd-B model, one recovers the upper-convected Maxwell (UCM) model, accounting for the dynamics of very concentrated solutions [45]. The turbulent-like features identified in Oldroyd-B cross-slot flows were detected for this even-simpler constitutive model likewise.

We based our analysis here on the measurement of time series of both velocity components at the fixed location $\boldsymbol{x}_*^{(3)}$ (exit probe), over long durations corresponding to 1000λ and again in the $M50$ mesh. We note that an initial transient with a duration of 100λ was removed from every simulation.

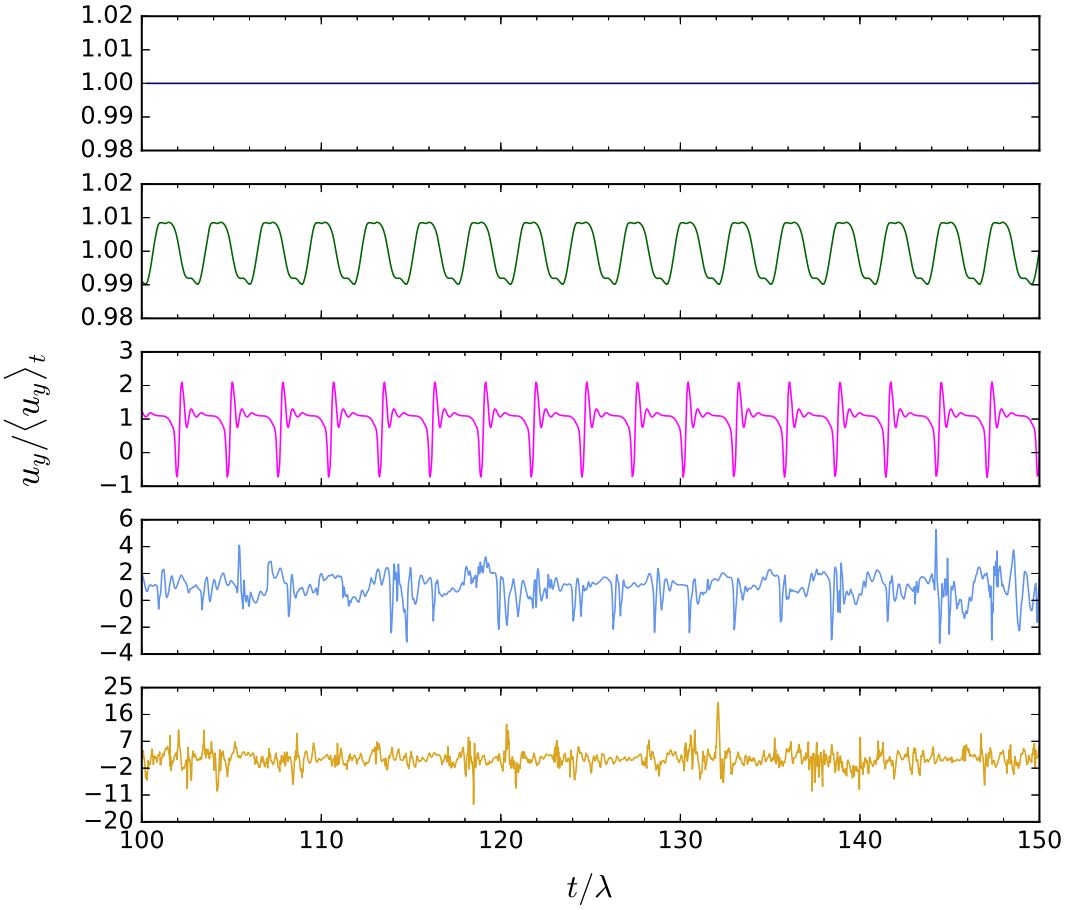

Figure 5.18 – Temporal evolution (subset of the total data set) of the y–component of velocity at the outlet, normalised by its time average over the whole time series, after the initial transient, for the UCM model and $Wi = 0.3, 1.3, 2.5, 5, 10$ (from top to bottom).

Firstly, we should recall that both purely elastic flow instabilities arise for this model (see Section 5.4 and specially Fig. 5.8, for $\beta = 0$). By exploring a wide range of elasticities, through small increments in Wi, the critical Weissenberg number values for the transitions could be established as $Wi_c^{(\mathrm{I})} \simeq 0.315 \pm 0.005$ (a relative difference of $\simeq 1\%$ compared to a previous benchmark work [137]), and $Wi_c^{(\mathrm{II})} \simeq 1.285 \pm 0.005$. We

depict in Fig. 5.18 the onset of unsteadiness and subsequent irregular flow for UCM model, by reporting the behaviour of the velocity axial component $u_y(\boldsymbol{x}_*^{(3)}, t)$ at the fixed location $\boldsymbol{x}_*^{(3)}$, for increasing Wi. Remark that only a subset of the data record is shown.

The spectra of $u_y(\boldsymbol{x}_*^{(3)}, t)$ are shown in Fig. 5.19. All those corresponding to the developed regime are averages over 10 spectra computed from consecutive subintervals (of duration 100λ) of the velocity time series obtained for a given value of Wi (after the initial transient). Reproducing qualitatively the onset of unsteady behaviour encountered for Oldroyd-B fluids (for $\beta > 0$), time-dependency initially manifests in the form of periodic, single-frequency oscillations, with some harmonics emerging as Wi increases (see inset of Fig. 5.19).

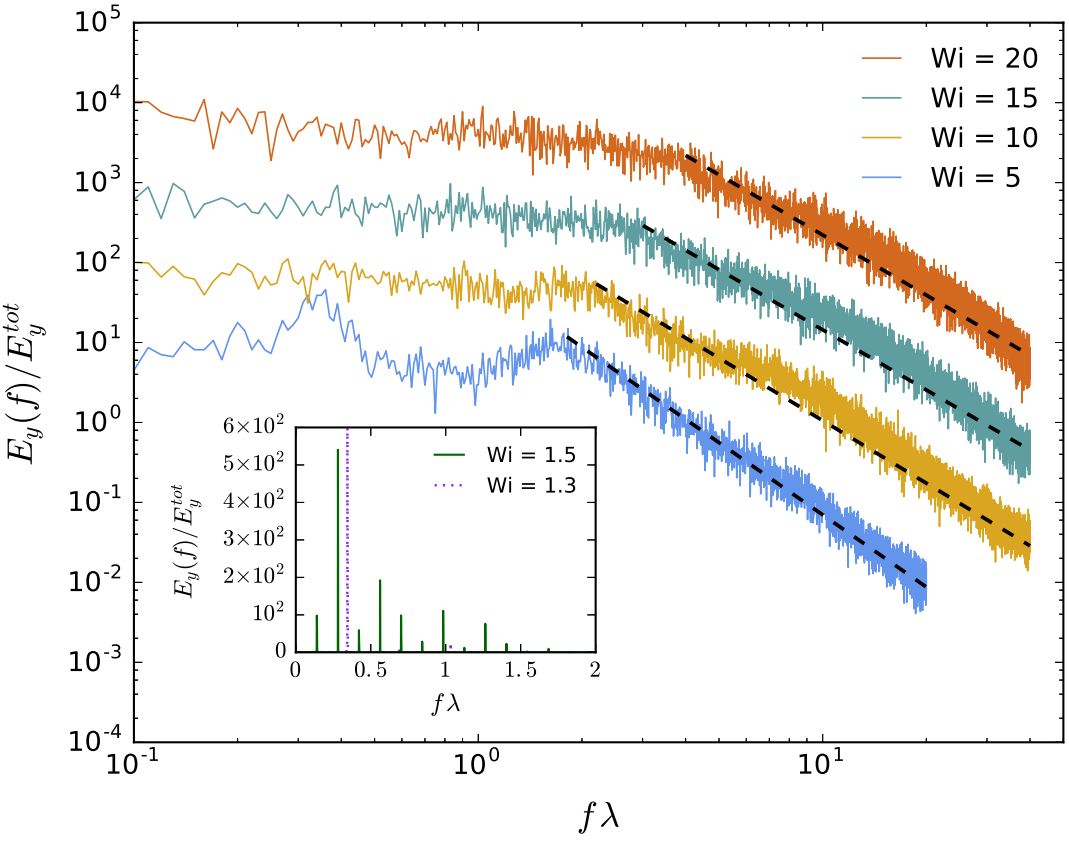

Figure 5.19 – Temporal spectra of fluctuations of the velocity component $u_y(\boldsymbol{x}_*^{(3)}, t)$ at the outlet, normalised by their integral E_y^{tot} in the elastic turbulence regime for the UCM model and different values of Wi; the curves have been vertically shifted to ease readability. The dashed black curves correspond to $E_y(f) \sim f^{-\delta}$, the exponents are $\delta \simeq (3.0, 2.6, 2.5, 2.5) \pm 0.4$ for $Wi = 5, 10, 15, 20$, respectively. Inset: spectra of fluctuations of $u_y(\boldsymbol{x}_*^{(3)}, t)$ in the unsteady flow regime at $Wi = 1.3$ (dotted purple curve) and $Wi = 1.5$ (solid green curve).

Above $Wi \approx 5$, the flow loses periodicity and the velocity spectra become continuous, being quite well described by a power-law function $E_y(f) \sim f^{-\delta}$ beyond a frequency that slightly increases with Wi (Fig. 5.19), and starting at higher frequencies, compared

to the flows of more diluted solutions. Here we find $\delta \simeq (3.0, 2.6, 2.5, 2.5) \pm 0.4$ for $Wi = 5, 10, 15, 20$, respectively. It is worth noting that the logarithmic slopes shown in Fig. 5.19 for $Wi \gtrsim 10$ should be considered with caution, as they represent an average behaviour over a frequency range, from which some deviation is noticeable.

To characterise statistically the UCM chaotic flows as elastic turbulent ones, we calculated the probability density functions (pdf's) of the fluctuations of the velocities $u_{x,y}(\boldsymbol{x}_*^{(3)}, t)$, as well as of the local accelerations $\partial_t u_{x,y}(\boldsymbol{x}_*^{(3)}, t)$, obtained from the temporal signals at probe 3. The results are presented in Figs. 5.20 and 5.21, where all variables are rescaled with the corresponding standard deviation σ. The statistics of u_y fluctuations are quite close to Gaussian for $Wi \geq 5$, while those of u_x are less so (inset of Fig. 5.20). Notice that for the UCM model, a two-state system develops likewise. We can see in the inset of Fig. 5.20 that the direction shifts of the flow-asymmetry impact the pdf of the fluctuations of the transversal velocity component $u_x(\boldsymbol{x}_*^{(3)}, t)$, for $Wi = 5$, in which bimodality sets in. The statistics of fluctuations of the accelerations in both directions are, once again, quite less dependent on the Weissenberg number. The corresponding pdf's (Fig. 5.21) display high tails that are indicative of non-Gaussian statistics, a typical feature in turbulent flows.

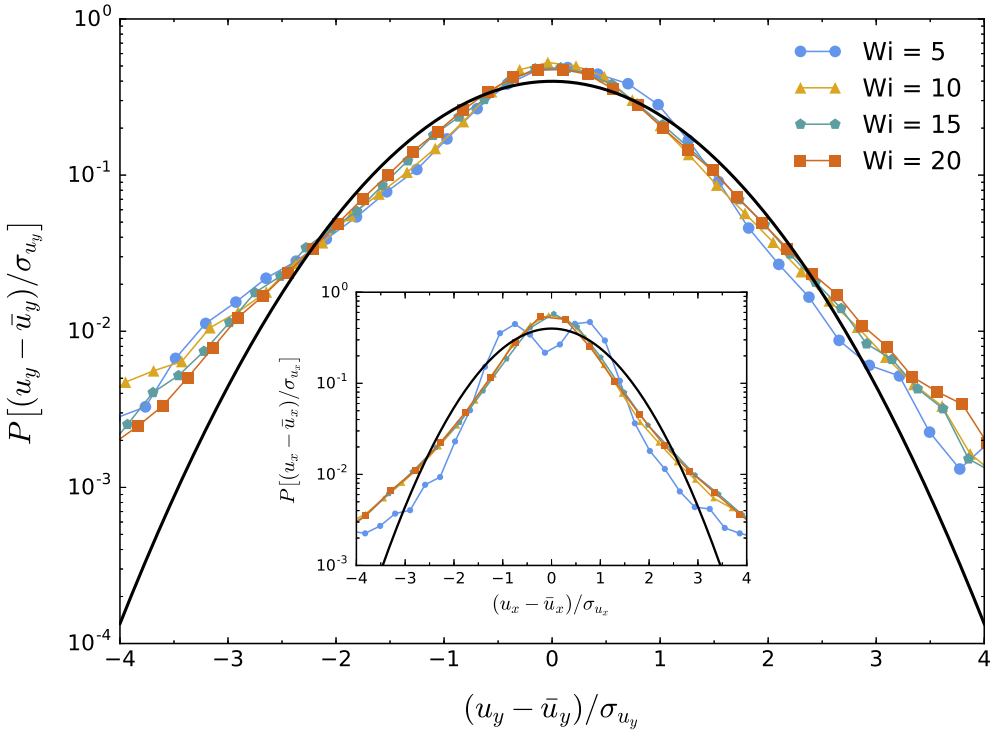

Figure 5.20 – Probability density functions of normalised velocity fluctuations $u_y' = (u_y - \overline{u_y})/\sigma_{u_y}$, where $u_y \equiv u_y(\boldsymbol{x}_*^{(3)}, t)$, the overbar denotes the temporal average and σ the standard deviation, for different values of Wi and following UCM constitutive equation. Inset: pdf's of the same quantity along x–direction. In both panels the solid black lines are standard Gaussian pdf's.

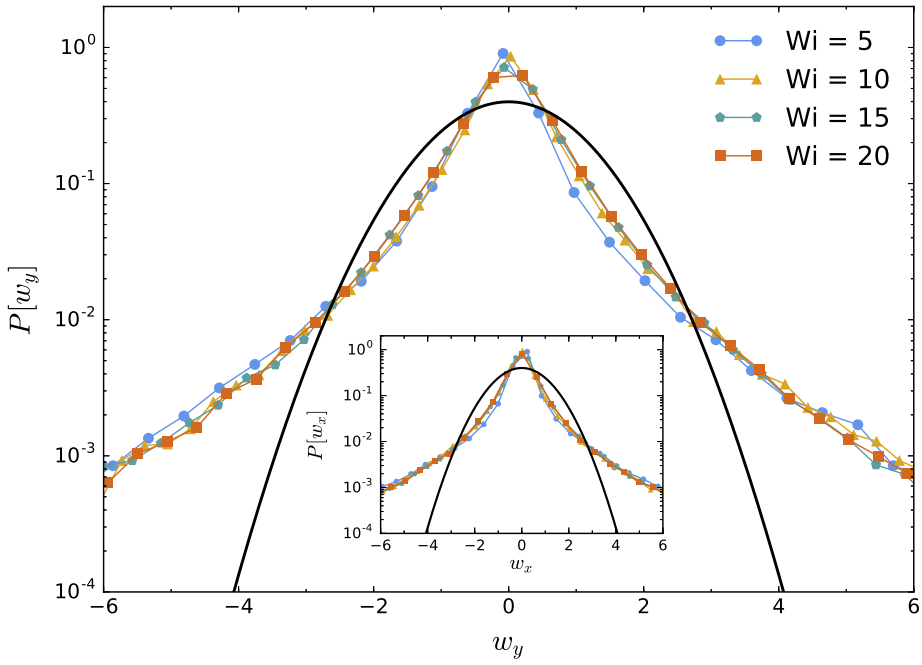

Figure 5.21 – Probability density functions of temporal increments of the normalised velocity fluctuations $w_y = (\partial_t u_y - \overline{\partial_t u_y})/\sigma_{\partial_t u_y}$, where $u_y \equiv u_y(\boldsymbol{x}_*^{(3)}, t)$, the overbar denotes the temporal average and σ the standard deviation, for different values of Wi and following UCM constitutive equation. Inset: pdf's of the same quantity along x–direction. In both panels the solid black lines are standard Gaussian pdf's.

We conclude this Section by pointing out that preliminary results on cross-slot flows, adopting another viscoelastic model (FENE-P) are reported in Appendix E.

5.7 Mixing properties of the turbulent-like flows

In the introductory Chapter, we stressed the relevance of fluid mixing as the main motivation (from the point of view of practical applications) for the present thesis. In this Section we report preliminary results about mixing enhancement in the turbulent-like flows at high Wi.

We considered for this study simple *Lagrangian tracers*, which are ideal inertialess particles that are driven by the flow without being subject to any hydrodynamical or external forces. In other words, Lagrangian tracers behave as fluid parcels (having indeed the same density as the carrying fluid) and move according to:

$$\dot{\boldsymbol{x}}_L(t) = \boldsymbol{u}_L(t) = \boldsymbol{u}(\boldsymbol{x}, t), \tag{5.7}$$

where $\boldsymbol{x}_L$ and $\boldsymbol{u}_L$ are the instantaneous position and velocity of the Lagrangian particle and $\boldsymbol{u}$ is the fluid velocity vector at the particle position.

By means of a C++ algorithm, developed as a run-time processing function in the framework of OpenFOAM®, we seeded the flow with a few hundred of these Lagrangian tracers in small areas near both cross-slot inlets, in an attempt to simulate pointlike particle injections, with different colors for each arm.

Appropriate initial and boundary conditions should be described for the Lagrangian tracers dynamics. After an initial transient of the flow simulations, corresponding to a duration of 100λ, Lagrangian tracers were randomly discharged in two square areas of length $0.5d$, placed symmetrically with respect to the central $y-$axis: black tracers near the left inlet and white ones close to the opposite entry. In Fig. 5.22, we show a schematic of the initial and final conditions for the particles. The former evolved following Eq. 5.7, subjected to a reflective boundary condition at the walls and an exit condition at a distance of $0.5d$ from both outlets. A systematic validation of the code algorithm was performed in an initial phase of the work and some details of this process are reported in Appendix D.

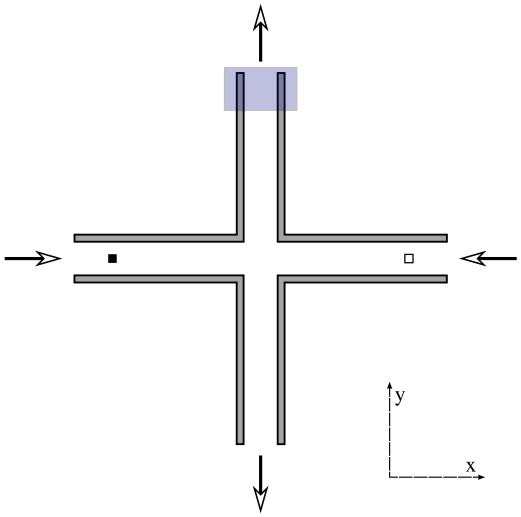

Figure 5.22 – Schematic of the cross-slot, showing the initial position of each group of particles (black tracers near the left inlet and white ones close to the opposite entry). The shaded square area near the upper outlet is the zone displayed in Figs. 5.23 and 5.24.

Time-dependent, viscoelastic flow regimes were considered, following the Oldroyd-B model (with $\beta = 1/9$) and the UCM model, with the Reynolds number fixed at $Re = 0$ in all cases. We compared the effectiveness of mixing the Lagrangian tracers between the unsteady fluid flows after the onset of elastic-turbulent features and simple laminar flows at the same viscosity ratio β. The final distribution of the particles near the upper outlet is shown in Figs. 5.23 (for the Oldroyd-B model) and 5.24 (for the UCM model). For both models, the top panel refers to the laminar flow, displaying a total absence of mixing. However, when a higher-Wi flow, undergoing the elastic turbulence regime is considered (bottom panel in both cases), a noticeable tracer mixing is observed.

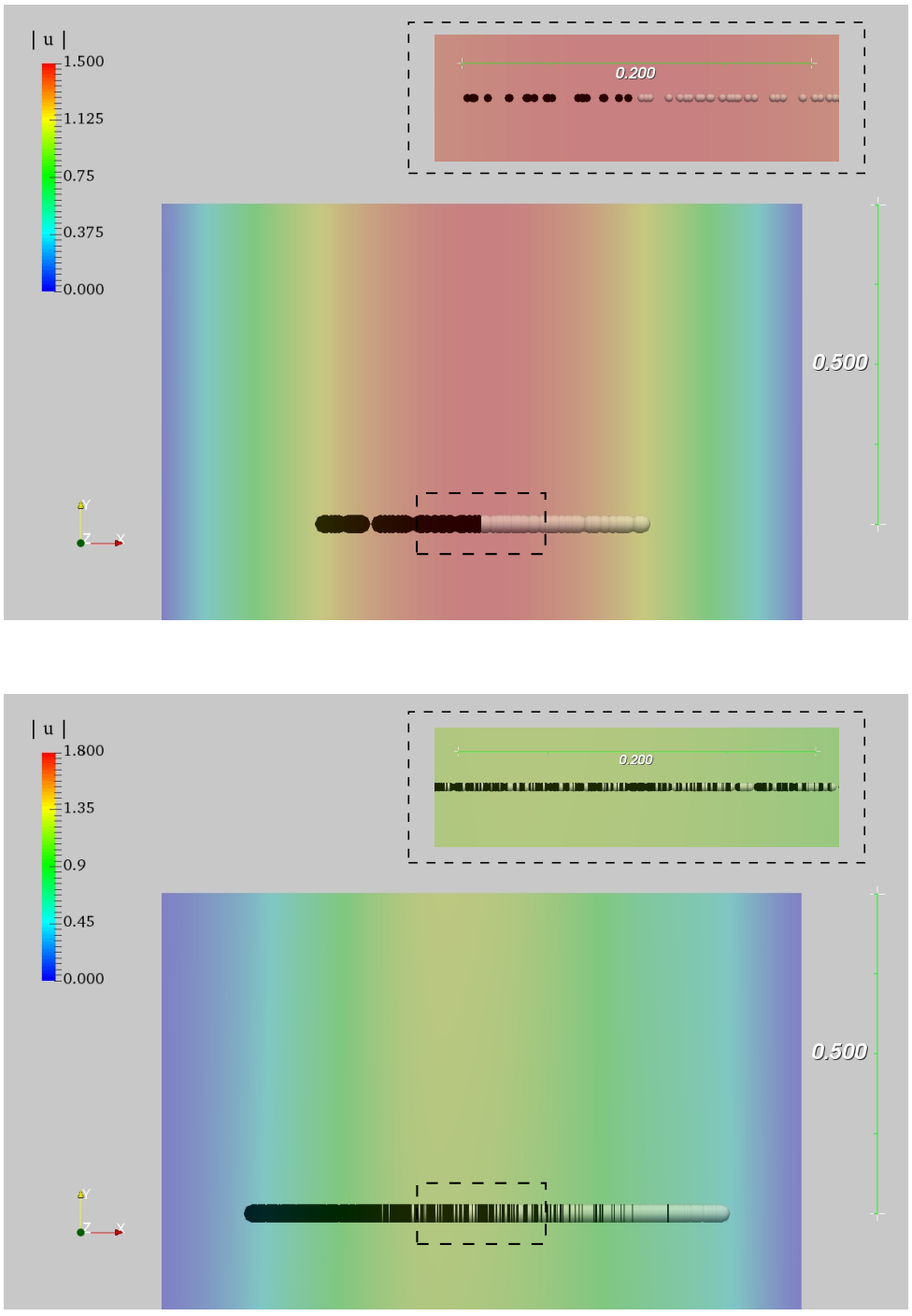

Figure 5.23 – Final distribution of hundreds of Lagrangian tracers (depicted here as coloured circles), near the upper outlet, for a laminar flow ($Wi = 0.3$, top panel) and an elastic-turbulent flow ($Wi = 25$, bottom panel). Tracers have been placed near the left inlet (black particles) and right inlet (white particles). A magnified view around the central y–axis is presented in the upper right corner. The lengths displayed are normalised by the cross-slot width d. Here, the Oldroyd-B model is adopted and $\beta = 1/9$.

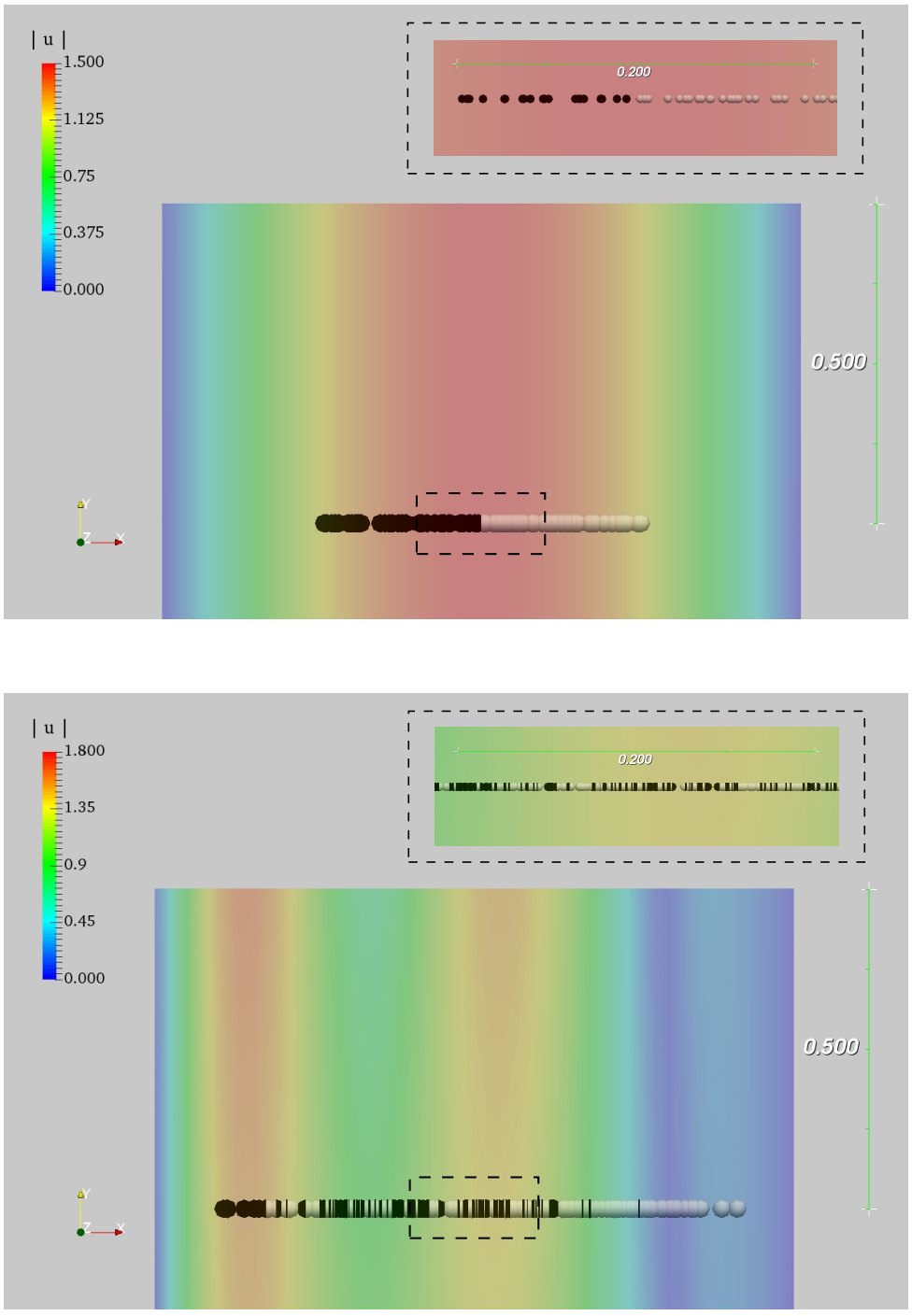

Figure 5.24 – Final distribution of hundreds of Lagrangian tracers (depicted here as coloured circles) near the upper outlet, for a laminar flow ($Wi = 0.3$, top panel) and an elastic-turbulent flow ($Wi = 10$, bottom panel). Tracers have been placed near the left inlet (black particles) and right inlet (white particles). A magnified view around the central y–axis is presented in the upper right corner. The lengths displayed are normalised by the cross-slot width d. Here, the UCM model (equivalent to Oldroyd-B, $\beta \to 0$) is adopted.

5.8 Concluding remarks

An extensive numerical study has been performed in a two-dimensional cross-slot geometry, for inertialess flows of viscoelastic fluids. For this setup, we detected two instabilities: a first one leading to a steady bifurcated flow and a second one driving the onset of time-dependent flow. While the first one, in agreement with experimental findings [159], is only present for rather concentrated solutions (including the limiting case $\beta \to 0$, equivalent to the UCM model), the second one, less documented, manifests for all viscosity ratios $\beta < 1$.

Similarly to what was done in previous studies [72, 136, 137], an asymmetric flow parameter was adopted to quantitatively express the excess flow rate in a stream as the bifurcation develops with increasing Wi, for a fixed β. It allowed us to provide numerical evidence that the cross-slot asymmetric instability is compatible with a supercritical pitchfork bifurcation. Moreover, for quite concentrated solutions (including the UCM limit), we found that the second instability corresponds to a supercritical Hopf bifurcation, which is somehow compatible with what was previously suggested in numerical work based on dilute 2D FENE-P flows [73].

We explored the transition to turbulent-like flow by means of simulations at progressively larger Weissenberg number above the critical value for the second (time-dependent) transition, for quite concentrated solutions ($\beta = 1/9$ and $\beta = 0$). For both fluid models considered, the flow lost periodicity and the velocity spectra became continuous above $Wi \approx 5$. Indeed, starting from $5 \lesssim Wi \lesssim 10$ they resulted to be quite well described by a power-law function, whose spectral exponent was found to be in the range $2 \lesssim \delta \lesssim 3$ and showed some tendency to decrease at higher Wi; the latter feature was also detected in experiments [20, 167].

To further characterise the statistical properties of our elastic turbulent flows, we computed the probability density functions (pdf's) of the fluctuations of velocity components and local accelerations, obtained from time series recorded at particular probe locations (typically at the outlet/inlet). The statistics of fluctuations of the axial component were found to be close to Gaussian for large enough Wi and those of fluctuations of the accelerations showed minimal dependency on the Weissenberg number (and the probe location), suggesting a faster (with Wi) onset of scaling properties at small scales.

Aiming at a preliminary analysis of the mixing properties of the cross-slot flows at significant levels of elasticity, we tracked an ensemble of Lagrangian tracers, initially released in two separated populations at the inlets. Both fluid models were, once again, considered and a complete absence of particle mixing was found before the onset of elastic turbulence. However, at sufficiently high Wi (corresponding to turbulent-like dynamics), a noticeable homogenisation of the spatial distribution of particles (from the two initial populations) was detected at the outlet, for Oldroyd-B and UCM models.

General conclusions

The underlying aspects of the numerical simulation of highly elastic viscoelastic fluid flows have been addressed in this thesis in two distinct contexts.

In the first part of the thesis, we reported a comprehensive scrutiny of a finite-volume-based viscoelastic solver, which was intended to be applied for simulating fluid flows at high elasticity levels in complex geometries. However, due to numerical divergence caused by the challenging high-Weissenberg number problem [29, 30], a solution was required in order to attain high enough elasticity levels. This led us to implement a stabilising mathematical tool in the numerical scheme, the square-root factorisation of the extra-stress evolution equation [102].

We validated the mathematical factorisation implemented and provided numerical evidence of the beneficial effect (in terms of increased stability) of the square-root decomposition of the extra-stress in this finite-volume-based implementation of the governing equations in a 2D channel. Even if the formulation proved itself as a powerful technique to increase numerical stability, it could not enable stable simulations in the planar channel for flows above an elasticity level corresponding to $Wi \gtrsim 5$. Furthermore, numerical simulations were performed using the square-root factorisation in a two-dimensional cross-slot geometry [135] and numerical divergence was again reported beyond certain limits of elasticity. These limits of stable computation were found to be around $Wi \approx 0.1$, *i.e.* at least one order of magnitude smaller than the required Wi to numerically explore time-dependent instabilities in the cross-slot geometry, according to previous studies from the literature, in similar setups [136, 137].

We inferred that complementary advanced numerical tools (other than a factorisation of the extra-stress equation) must be present in that in-house viscoelastic flow solver in order to investigate the interesting phenomena that arise at higher levels of elasticity, which concluded the first part of this document.

In the second part of the thesis, we adopted the open-source OpenFOAM® CFD software to investigate numerically the dynamics of Oldroyd-B fluids in a 2D cross-slot geometry for broad ranges of the Weissenberg number and the polymer concentration (including the UCM limit) at $Re = 0$, focusing on the possibility to obtain elastic turbulence states.

By spanning the (β, Wi) plane with a large number of simulations, we could obtain a full picture of the cross-slot instabilities, in the form of a novel stability portrait of the system. We then provided a characterisation of the dependence of the critical Weissenberg number for the time-dependent transition $Wi_c^{(II)}$ on the viscosity ratio β. Albeit derived heuristically, this expression allows to quantitatively delimit the regions $Wi > Wi_c^{(II)}(\beta)$ of the parameter space where elastic turbulence may be excited.

We explored the transition to turbulent-like flow by means of simulations at progressively larger Weissenberg number above the critical value $Wi_c^{(II)}$, for quite concentrated solutions ($\beta = 1/9$ and the UCM case $\beta = 0$). Close to the onset of the second instability the flow was found to display regular oscillations in time, while at larger elasticities its dynamics appeared more and more irregular with increasing Wi. To quantitatively study the transition we examined time series of the fluid velocity at a fixed point located at the beginning of one of the outlet channels and far from the walls, and the associated frequency spectra. The latter have a discrete character, showing distinct peaks, for $Wi \gtrsim Wi_c^{(II)}$, while they subsequently become continuous when $Wi > 5$, approximately, pointing to the emergence of elastic turbulence.

In such a large-elasticity range, the spectra display a power-law behaviour beyond a frequency that moderately increases with Wi, as also observed in experiments [20]. The spectral exponent δ was found to decrease with Wi, another feature that is common to experimental findings [20, 167]. However, we obtain values in the range $2 < \delta < 3$ (and not far from $\delta = 2.5$), somehow smaller than those measured in experiments and the theoretical prediction for homogeneous isotropic elastic turbulence [180]. While we cannot exclude that the 2D nature of our flow has an impact on this result, we remark that the statistical symmetries assumed in the theory clearly do not hold for our cross-slot geometry. It should also be noted that similarly energetic spectra at small scales have been recently detected in numerical simulations of 2D Oldroyd-B cellular flows [34], sharing with our setup both the presence of regions of intense strain and the absence of artificial polymer-stress diffusion.

We further analysed the statistics of fluctuations of velocities and of their temporal increments (local accelerations) for $Wi > 5$. Those of the axial velocity components are close to Gaussian for all Wi values in the developed regime, those of the transversal ones have a similar behaviour but they also exhibit a bimodal pdf for $10 < Wi < 20$, which reflects the important alternations of the spatial flow asymmetry occurring in this range of Weissenberg numbers. The pdf's of both components of the local accelerations, instead, definitely deviate from Gaussianity and are characterised by high tails, a typical feature of turbulent flows. Such a phenomenology is in agreement with that observed in previous experimental investigations (see *e.g.* the work of Burghelea et al. [13]).

We tracked an ensemble of synthetic Lagrangian tracers (initially distributed in well separated populations) inside our cross-slot setup in order to provide a (preliminary)

characterisation of the mixing effectiveness of the elastic-turbulent flows. We reported a perceptible mixing of tracer particles (for both Oldroyd-B and UCM fluid models) when the Lagrangian particles were advected in a flow featuring turbulent-like behaviour. Furthermore, we noticed that the mixing of tracer particles was more pronounced for the zero-viscosity ratio solution (equivalent to UCM fluid) in comparison to the $\beta = 1/9$ one, even if a smaller Weissenberg number was adopted for the former.

In summary, we have shown the possibility to numerically reproduce the different dynamical regimes of polymer solutions that are experimentally observed in cross-slot devices, using simple viscoelastic fluid models (Oldroyd-B and UCM). In particular, this approach allowed us to obtain turbulent-like states bearing some resemblance with elastic turbulence for what concerns most of the statistical features considered. Some quantitative differences have also been put in evidence, which calls for further theoretical and numerical developments.

Future prospects

We propose miscellaneous paths that would be interesting to explore as an extension of the work developed in this thesis.

- To provide a more precise comparison with experimental studies, three-dimensional flows should be simulated in the cross-slot geometry.
- A complex and intriguing turbulent-like two-state system was observed and described in Section 5.5; a deep understanding of the origin and statistical properties of that dynamics is currently lacking.
- Only a preliminary inquiry on the mixing properties of the elastic-turbulent cross-slot flows was carried out. Further and deeper developments are needed, as *e.g.* more quantitative measurement using Lagrangian tracers or an inspection of the Eulerian dynamics of particles, through a passive scalar transport analysis.
- To explore the effects of polymer non-linear elasticity, more complex viscoelastic fluid models could be considered, like different closures of the FENE family of models (see Subsection 1.3.2).

Bibliography

[1] A. Groisman and V. Steinberg. "Efficient mixing at low Reynolds numbers using polymer additives". In: *Nature* 410 (2001), pp. 905–908 (cit. on pp. 1, 48, 49).

[2] T. H. Solomon and I. Mezić. "Uniform resonant chaotic mixing in fluid flows". In: *Nature* 425 (2003), pp. 376–380 (cit. on p. 1).

[3] N.-T. Nguyen and Z. Wu. "Micromixers - a review". In: *Journal of Micromechanics and microengineering* 15 (2005), R1–R16 (cit. on p. 1).

[4] C.-Y. Lee, C.-L. Chang, Y.-N. Wang, and L.-M. Fu. "Microfluidic mixing: a review". In: *International Journal of Molecular Sciences* 12 (2011), pp. 3263–3287 (cit. on p. 1).

[5] A. D. Stroock, S. K. W. Dertinger, A. Ajdari, I. Mezić, H. A. Stone, and G. M. Whitesides. "Chaotic mixer for microchannels". In: *Science* 295 (2002), pp. 647–651 (cit. on p. 1).

[6] G. V. Vinogradov and V. N. Manin. "An experimental study of elastic turbulence". In: *Kolloid-Zeitschrift und Zeitschrift für Polymere* 201.2 (1965), pp. 93–98 (cit. on pp. 1, 11, 48).

[7] A. Groisman and V. Steinberg. "Elastic turbulence in curvilinear flows of polymer solutions". In: *New Journal of Physics* 6 (2004), pp. 29–48 (cit. on pp. 1, 48).

[8] B. Thomases and M. Shelley. "Transition to mixing and oscillations in a Stokesian viscoelastic flow". In: *Physical Review Letters* 103 (2009), pp. 094501-1–094501-4 (cit. on pp. 1, 2, 47).

[9] A. Groisman and V. Steinberg. "Elastic turbulence in a polymer solution flow". In: *Nature* 405 (2000), pp. 53–55 (cit. on pp. 1, 11, 43, 48, 72).

[10] P. G. De Gennes. "Coil-stretch transition of dilute flexible polymers under ultrahigh velocity gradients". In: *Journal of Chemical Physics* 60.12 (1974), pp. 5030–5042 (cit. on p. 1).

[11] R. G. Larson and J. J. Magda. "Coil-stretch transitions in mixed shear and extensional flows of dilute polymer solutions". In: *Macromolecules* 22 (1989), pp. 3004–3010 (cit. on p. 1).

[12] T. Burghelea, E. Segre, I. Bar-Joseph, A. Groisman, and V. Steinberg. "Chaotic flow and efficient mixing in a microchannel with a polymer solution". In: *Physical Review E* 69 (2004), pp. 066305-1–066305-8 (cit. on pp. 1, 48).

[13] T. Burghelea, E. Segre, and V. Steinberg. "Elastic turbulence in von Karman swirling flow between two disks". In: *Physics of Fluids* 19 (2007), pp. 053104-1–053104-26 (cit. on pp. 1, 75, 86).

[14] S. Berti and G. Boffetta. "Elastic waves and transition to elastic turbulence in a two-dimensional viscoelastic Kolmogorov flow". In: *Physical Review E* 82 (2010), pp. 036314-1–036314-10 (cit. on pp. 1, 69).

[15] Y. Jun and V. Steinberg. "Elastic turbulence in a curvilinear channel flow". In: *Physical Review E* 84 (2011), pp. 056325-1–066305-13 (cit. on p. 1).

[16] M. Grilli, A. Vázquez-Quesada, and M. Ellero. "Transition to turbulence and mixing in a viscoelastic fluid flowing inside a channel with a periodic array of cylindrical obstacles". In: *Physical Review Letters* 110 (2013), pp. 174501-1–174501-5 (cit. on p. 1).

[17] H.-N. Zhang, F.-C. Li, Y. Cao, T. Kunugi, and B. Yu. "Direct numerical simulation of elastic turbulence and its mixing-enhancement effect in a straight channel flow". In: *Chinese Physics B* 22.2 (2013), pp. 024703-1–024703-8 (cit. on pp. 1, 48).

[18] B. Qin and P. E. Arratia. "Characterizing elastic turbulence in channel flows at low Reynolds number". In: *Physical Review Fluids* 2 (2017), pp. 083302-1–083302-9 (cit. on pp. 1, 73).

[19] A. Souliès, J. Aubril, C. Castelain, and T. Burghelea. "Characterisation of elastic turbulence in a serpentine micro-channel". In: *Physics of Fluids* 29 (2017), pp. 083102-1–083102-21 (cit. on p. 1).

[20] P. C. Sousa, F. T. Pinho, and M. A. Alves. "Purely-elastic flow instabilities and elastic turbulence in microfluidic cross-slot devices". In: *Soft Matter* 14 (2018), pp. 1344–1354 (cit. on pp. 1, 49, 51, 69, 71, 72, 83, 86).

[21] R. van Buel, C. Schaaf, and H. Stark. "Elastic turbulence in two-dimensional Taylor-Couette flows". In: *Europhysics Letters* 124 (2018), pp. 14001-1–14001-7 (cit. on pp. 1, 73).

[22] B. Traore, C. Castelain, and T. Burghelea. "Efficient heat transfer in a regime of elastic turbulence". In: *Journal of Non-Newtonian Fluid Mechanics* 223 (2015), pp. 62–76 (cit. on pp. 1, 43, 48).

[23] W. M. Abed, A. F. Domingues, R. J. Poole, and D. J. C. Dennis. "Heat transfer enhancement in a cross-slot micro-geometry". In: *International Journal of Thermal Sciences* 121 (2017), pp. 249–265 (cit. on pp. 1, 47).

[24] W. M. Abed, R. D. Whalley, D. J. C. Dennis, and R. J. Poole. "Experimental investigation of the impact of elastic turbulence on heat transfer in a serpentine channel". In: *Journal of Non-Newtonian Fluid Mechanics* 231 (2016), pp. 68–78 (cit. on pp. 1, 48).

[25] D.-Y. Li, X.-B. Li, H.-N. Zhang, F.-C. Li, S. Qian, and S. W. Joo. "Efficient heat transfer enhancement by elastic turbulence with polymer solution in a curved microchannel". In: *Microfluid Nanofluidics* 21.10 (2017), pp. 1–13 (cit. on p. 1).

[26] D. Samanta, Y. Dubief, M. Holzner, C. Schäfer, A. N. Morozov, C. Wagner, and B. Hof. "Elasto-inertial turbulence". In: *Proceedings of the National Academy of Sciences of the United States of America* 110.26 (2013), pp. 10557–10562 (cit. on p. 2).

[27] V. Steinberg. "Elastic stresses in random flow of a dilute polymer solution and the turbulent drag reduction problem". In: *Comptes Rendus Physique* 10 (2009), pp. 728–739 (cit. on p. 2).

[28] R. G. Owens and T. N. Phillips. *Computational Rheology*. London: Imperial College Press, 2002 (cit. on p. 2).

[29] M. J. Crochet and K. Walters. "Numerical methods in non-Newtonian fluid mechanics". In: *Annual Review of Fluid Mechanics* 15 (1983), pp. 241–260 (cit. on pp. 2, 17, 85).

[30] R. Keunings. "On the high Weissenberg number problem". In: *Journal of Non-Newtonian Fluid Mechanics* 20 (1986), pp. 209–226 (cit. on pp. 2, 17, 85).

[31] F. Dupret and J. M. Marchal. "Loss of evolution in the flow of viscoelastic fluids". In: *Journal of Non-Newtonian Fluid Mechanics* 20 (1986), pp. 143–171 (cit. on pp. 2, 17).

[32] R. Sureshkumar and A. N. Beris. "Effect of artificial stress diffusivity on the stability of numerical calculations and the flow dynamics of time-dependent viscoelastic flows". In: *Journal of Non-Newtonian Fluid Mechanics* 60 (1995), pp. 53–80 (cit. on pp. 3, 18).

[33] T. Min, J. Y. Yoo, and H. Choi. "Effect of spatial discretization schemes on numerical solutions of viscoelastic fluid flows". In: *Journal of Non-Newtonian Fluid Mechanics* 100 (2001), pp. 27–47 (cit. on pp. 3, 19).

[34] A. Gupta and D. Vincenzi. "Effect of polymer-stress diffusion in the numerical simulation of elastic turbulence". In: *Journal of Fluid Mechanics* 870 (2019), pp. 405–418 (cit. on pp. 3, 18, 19, 72, 86).

[35] R. Fattal and R. Kupferman. "Constitutive laws for the matrix-logarithm of the conformation tensor". In: *Journal of Non-Newtonian Fluid Mechanics* 123 (2004), pp. 281–285 (cit. on pp. 3, 20, 55).

[36] R. Fattal and R. Kupferman. "Time-dependent simulation of viscoelastic flows at high Weissenberg number using the log-conformation representation". In: *Journal of Non-Newtonian Fluid Mechanics* 126 (2005), pp. 23–37 (cit. on pp. 3, 40, 55).

[37] F. J. Galindo-Rosales, M. A. Alves, and M. S. N. Oliveira. "Microdevices for extensional rheometry of low viscosity elastic liquids: a review". In: *Microfluid Nanofluidics* 14 (2013), pp. 1–19 (cit. on p. 3).

[38] J. F. M. Schoonen, F. H. M. Swartjes, G. W. M. Peters, F. P. T. Baaijens, and H. E. H. Meijer. "A 3D numerical/experimental study on a stagnation flow of a polyisobutylene solution". In: *Journal of Non-Newtonian Fluid Mechanics* 79 (1998), pp. 529–561 (cit. on p. 3).

[39] G. W. M. Peters, J. F. M. Schoonen, F. P. T. Baaijens, and H. E. H. Meijer. "On the performance of enhanced constitutive models for polymer melts in a cross-slot flow". In: *Journal of Non-Newtonian Fluid Mechanics* 82 (1999), pp. 387–427 (cit. on p. 3).

[40] O. Darrigol. *Worlds of Flow*. New York: Oxford University Press, 2005 (cit. on p. 9).

[41] C. L. Fefferman. *Existence and smoothness of the Navier-Stokes equation*. In: The Millenium Prize problems. Clay Mathematics Institute, 2006, pp. 57–67 (cit. on p. 10).

[42] P. J. Flory. *Principles of Polymer Chemistry*. New York: Cornell University Press, 1953 (cit. on p. 10).

[43] T. T. Perkins, D. E. Smith, and S. Chu. "Single polymer dynamics in an elongational flow". In: *Science* 276 (1997), pp. 2016–2021 (cit. on p. 10).

[44] D. E. Smith, H. P. Babcock, and S. Chu. "Single-polymer dynamics in steady shear flow". In: *Science* 283 (1999), pp. 1724–1727 (cit. on p. 10).

[45] R. B. Bird, R. C. Armstrong, and O. Hassager. *Dynamics of Polymeric Liquids*. Vol. 1. Fluid Mechanics. New York: John Wiley & Sons, 1987 (cit. on pp. 11, 12, 76).

[46] J. G. Oldroyd. "Non-Newtonian effects in steady motion of some idealized elastico-viscous liquids". In: *Proceedings of the Royal Society of London A* 245 (1958), pp. 278–297 (cit. on p. 11).

[47] R. B. Bird and C. F. Curtiss. "Fascinating polymeric liquids". In: *Physics Today* 38 (1984), pp. 36–43 (cit. on p. 11).

[48] F. H. Garner and A. H. Nissan. "Rheological properties of high-viscosity solutions of long molecules". In: *Nature* 158 (1946), pp. 634–635 (cit. on p. 11).

[49] K. Weissenberg. "A continuum theory of rheological phenomena". In: *Nature* 159 (1947), pp. 310–311 (cit. on p. 11).

[50] J. L. Lumley. "Drag reduction in turbulent flow by polymer additives". In: *Journal of Polymer Science: Macromolecular Reviews* 7 (1973), pp. 263–290 (cit. on p. 11).

[51] K. Walters. "Overview of macroscopic viscoelastic flow". In: *Viscoelasticity and Rheology*. Madison, Wisconsin: Academic Press, 1985. Chap. 3, pp. 47–79 (cit. on p. 11).

[52] D. Rajagopalan, R. C. Armstrong, and R. A. Brown. "Finite element methods for calculation of steady, viscoelastic flow using constitutive equations with a Newtonian viscosity". In: *Journal of Non-Newtonian Fluid Mechanics* 36 (1990), pp. 159–192 (cit. on pp. 12, 19).

[53] J. L. White and A. B. Metzner. "Development of constitutive equations for polymeric melts and solutions". In: *Journal of Applied Polymer Science* 7 (1963), pp. 1867–1889 (cit. on p. 12).

[54] N. Phan-Thien and R. I. Tanner. "A new constitutive equation derived from network theory". In: *Journal of Non-Newtonian Fluid Mechanics* 2 (1977), pp. 353–365 (cit. on p. 12).

[55] N. Phan-Thien. "A nonlinear network viscoelastic model". In: *Journal of Rheology* 22 (1978), pp. 259–283 (cit. on p. 12).

[56] H. Giesekus. "A simple constitutive equation for polymer fluids based on the concept of deformation-dependent tensorial mobility". In: *Journal of Non-Newtonian Fluid Mechanics* 11 (1982), pp. 69–109 (cit. on p. 12).

[57] R. B. Bird, C. F. Curtiss, R. C. Armstrong, and O. Hassager. *Dynamics of Polymeric Liquids*. Vol. 2. Kinetic Theory. New York: John Wiley & Sons, 1987 (cit. on pp. 12–14, 18).

[58] J. C. Maxwell. "On the dynamical theory of gases". In: *Philosophical Transactions of the Royal Society of London A* 157 (1867), pp. 49–88 (cit. on p. 12).

[59] J. G. Oldroyd. "On the formulation of rheological equations of state". In: *Proceedings of the Royal Society of London A* 200 (1950), pp. 523–541 (cit. on pp. 12, 13).

[60] M. S. Green and A. V. Tobolsky. "A new approach to the theory of relaxing polymeric media". In: *Journal of Chemical Physics* 14.2 (1946), pp. 80–92 (cit. on p. 12).

[61] M. Renardy. "A comment on smoothness of viscoelastic stresses". In: *Journal of Non-Newtonian Fluid Mechanics* 138 (2006), pp. 204–205 (cit. on p. 13).

[62] B. Thomases and M. Shelley. "Emergence of singular structures in Oldroyd-B fluids". In: *Physics of Fluids* 19 (2007), pp. 103103-1–103103-12 (cit. on p. 13).

[63] H. R. Warner Jr. "Kinetic theory and rheology of dilute suspensions of finitely extendible dumbbells". In: *Industrial & Engineering Chemistry Fundamentals* 11.3 (1972), pp. 379–387 (cit. on p. 14).

[64] A. Peterlin. "Hydrodynamics of macromolecules in a velocity field with longitudinal gradient". In: *Journal of Polymer Science Part B: Polymer Letters* 4 (1966), pp. 287–291 (cit. on p. 14).

[65] M. D. Chilcott and J. M. Rallison. "Creeping flow of dilute polymer solutions past cylinders and spheres". In: *Journal of Non-Newtonian Fluid Mechanics* 29 (1988), pp. 381–432 (cit. on pp. 14, 15).

[66] G. Lielens, P. Halin, I. Jaumain, R. Keunings, and V. Legat. "New closure approximations for the kinetic theory of finitely extensible dumbbells". In: *Journal of Non-Newtonian Fluid Mechanics* 76 (1998), pp. 249–279 (cit. on pp. 14, 15).

[67] G. Lielens, R. Keunings, and V. Legat. "The FENE-L and FENE-LS closure approximations to the kinetic theory of finitely extensible dumbbells". In: *Journal of Non-Newtonian Fluid Mechanics* 87 (1999), pp. 179–196 (cit. on pp. 14, 15).

[68] J. Remmelgas, P. Singh, and L. G. Leal. "Computational studies of nonlinear elastic dumbbell models of Boger fluids in a cross-slot flow". In: *Journal of Non-Newtonian Fluid Mechanics* 88 (1999), pp. 31–61 (cit. on pp. 14, 15, 45).

[69] A. J. Szeri. "A deformation tensor model for nonlinear rheology of FENE polymer solutions". In: *Journal of Non-Newtonian Fluid Mechanics* 92 (2000), pp. 1–25 (cit. on p. 14).

[70] P. Ilg, I. V. Karlin, and H. C. Öttinger. "Canonical distribution functions in polymer dynamics. (I). Dilute solutions of flexible polymers". In: *Physica A: Statistical Mechanics and its Applications* 315 (2002), pp. 367–385 (cit. on p. 14).

[71] R. B. Bird, P. J. Dotson, and N. L. Johnson. "Polymer solution rheology based on a finitely extensible bead-spring chain model". In: *Journal of Non-Newtonian Fluid Mechanics* 7 (1980), pp. 213–235 (cit. on pp. 14, 15).

[72] G. N. Rocha, R. J. Poole, M. A. Alves, and P. J. Oliveira. "On extensibility effects in the cross-slot flow bifurcation". In: *Journal of Non-Newtonian Fluid Mechanics* 156 (2009), pp. 58–69 (cit. on pp. 15, 45, 47, 50, 51, 83).

[73] L. Xi and M. D. Graham. "A mechanism for oscillatory instability in viscoelastic cross-slot flow". In: *Journal of Fluid Mechanics* 622 (2009), pp. 145–165 (cit. on pp. 15, 47, 51, 65, 83).

[74] O. Reynolds. "An experimental investigation of the circumstances which determine whether the motion of water shall be direct or sinuous, and of the law of resistance in parallel channels". In: *Proceedings of the Royal Society of London A* 35 (1883), pp. 84–99 (cit. on p. 16).

[75] M. Reiner. "The Deborah number". In: *Physics Today* 17.1 (1964), p. 62 (cit. on p. 16).

[76] J. L. White. "Dynamics of viscoelastic fluids, melt fracture, and the rheology of fiber spinning". In: *Journal of Applied Polymer Science* 8 (1964), pp. 2339–2357 (cit. on p. 16).

[77] R. J. Poole. "The Deborah and Weissenberg numbers". In: *The British Society of Rheology, Rheology Bulletin* 53.2 (2012), pp. 32–39 (cit. on p. 16).

[78] J. M. Dealy. "Weissenberg and Deborah numbers - Their definition and use". In: *Society of Rheology, Rheology Bulletin* 79.2 (2010), pp. 14–18 (cit. on p. 16).

[79] J. H. Ferziger and M. Perić. *Computational Methods for Fluid Dynamics*. 2nd ed. Berlin: Springer, 1999 (cit. on pp. 17, 27).

[80] J. M. Rallison and E. J. Hinch. "Do we understand the physics in the constitutive equation?" In: *Journal of Non-Newtonian Fluid Mechanics* 29 (1988), pp. 37–55 (cit. on p. 17).

[81] K. Walters and M. F. Webster. "The distinctive CFD challenges of computational rheology". In: *International Journal for Numerical Methods in Fluids* 43 (2003), pp. 577–596 (cit. on p. 17).

[82] R. Keunings. "Simulation of viscoelastic fluid flow". In: *Fundamentals of Computer Modeling for Polymer Processing*. Ed. by C. L. Tucker III. Munich: Carl Hanser Verlag, 1989. Chap. 9, pp. 403–469 (cit. on p. 17).

[83] D. Joseph. *Fluid Dynamics of Viscoelastic Liquids*. New York: Springer-Verlag, 1990 (cit. on p. 17).

[84] I. M. Rutkevich. "Some general properties of the equations of viscoelastic incompressible fluid dynamics". In: *Journal of Applied Mathematics and Mechanics* 33.1 (1969), pp. 30–39 (cit. on p. 17).

[85] I. M. Rutkevich. "The propagation of small perturbations in a viscoelastic fluid". In: *Journal of Applied Mathematics and Mechanics* 34.1 (1970), pp. 35–50 (cit. on p. 17).

[86] D. D. Joseph, M. Renardy, and J.-C. Saut. "Hyperbolicity and change of type in the flow of viscoelastic fluids". In: *Archive for Rational Mechanics and Analysis* 87.3 (1985), pp. 213–251 (cit. on p. 17).

[87] D. D. Joseph and J. C. Saut. "Change of type and loss of evolution in the flow of viscoelastic fluids". In: *Journal of Non-Newtonian Fluid Mechanics* 20 (1986), pp. 117–141 (cit. on p. 17).

[88] M. A. Hulsen. "A sufficient condition for a positive definite configuration tensor in differential models". In: *Journal of Non-Newtonian Fluid Mechanics* 38 (1990), pp. 93–100 (cit. on p. 17).

[89] J. van der Zanden and M. Hulsen. "Mathematical and physical requirements for successful computations with viscoelastic fluid models". In: *Journal of Non-Newtonian Fluid Mechanics* 29 (1988), pp. 93–117 (cit. on p. 17).

[90] Y. Kwon and A. I. Leonov. "Stability constraints in the formulation of viscoelastic constitutive equations". In: *Journal of Non-Newtonian Fluid Mechanics* 58 (1995), pp. 25–46 (cit. on p. 17).

[91] A. W. El-Kareh and L. G. Leal. "Existence of solutions for all Deborah numbers for a non-Newtonian model modified to include diffusion". In: *Journal of Non-Newtonian Fluid Mechanics* 33 (1989), pp. 257–287 (cit. on p. 18).

[92] T. Vaithianathan, A. Robert, J. G. Brasseur, and L. R. Collins. "An improved algorithm for simulating three-dimensional viscoelastic turbulence". In: *Journal of Non-Newtonian Fluid Mechanics* 140 (2006), pp. 3–22 (cit. on p. 18).

[93] B. Thomases. "An analysis of the effect of stress diffusion on the dynamics of creeping viscoelastic flow". In: *Journal of Non-Newtonian Fluid Mechanics* 166 (2011), pp. 1221–1228 (cit. on p. 18).

[94] R. Sureshkumar, A. N. Beris, and R. A. Handler. "Direct numerical simulation of the turbulent channel flow of a polymer solution". In: *Physics of Fluids* 9.3 (1997), pp. 743–755 (cit. on p. 18).

[95] C. D. Dimitropoulos, R. Sureshkumar, and A. N. Beris. "Direct numerical simulation of viscoelastic turbulent channel flow exhibiting drag reduction: effect of the variation of rheological parameters". In: *Journal of Non-Newtonian Fluid Mechanics* 79 (1998), pp. 433–468 (cit. on p. 18).

[96] S. Berti, A. Bistagnino, G. Boffetta, A. Celani, and S. Musacchio. "Two-dimensional elastic turbulence". In: *Physical Review E* 77 (2008), pp. 055306-1–055306-4 (cit. on pp. 18, 43, 73).

[97] H. Garg, E. Calzavarini, G. Mompean, and S. Berti. "Particle-laden two-dimensional elastic turbulence". In: *The European Physical Journal E* 41.115 (2018), pp. 1–11 (cit. on p. 18).

[98] R. C. King, M. R. Apelian, R. C. Armstrong, and R. A. Brown. "Numerically stable finite element techniques for viscoelastic calculations in smooth and singular geometries". In: *Journal of Non-Newtonian Fluid Mechanics* 29 (1988), pp. 147–216 (cit. on p. 19).

[99] M. A. Mendelson, P.-W. Yeh, R. A. Brown, and R. C. Armstrong. "Approximation error in finite element calculation of viscoelastic fluid flows". In: *Journal of Non-Newtonian Fluid Mechanics* 10 (1982), pp. 31–54 (cit. on p. 19).

[100] J. Sun, N. Phan-Thien, and R. I. Tanner. "An adaptive viscoelastic stress splitting scheme and its applications: AVSS/SI and AVSS/SUPG". In: *Journal of Non-Newtonian Fluid Mechanics* 65 (1996), pp. 75–91 (cit. on p. 19).

[101] L. J. Amoreira and P. J. Oliveira. "Comparison of different formulations for the numerical calculation of unsteady incompressible viscoelastic fluid flow". In: *Advances in Applied Mathematics and Mechanics* 2.4 (2010), pp. 483–502 (cit. on p. 19).

[102] N. Balci, B. Thomases, M. Renardy, and C. R. Doering. "Symmetric factorization of the conformation tensor in viscoelastic fluid models". In: *Journal of Non-Newtonian Fluid Mechanics* 166 (2011), pp. 546–553 (cit. on pp. 20, 21, 29, 30, 85).

[103] A. M. Afonso, F. T. Pinho, and M. A. Alves. "The *kernel-conformation* constitutive laws". In: *Journal of Non-Newtonian Fluid Mechanics* 167-168 (2012), pp. 30–37 (cit. on p. 20).

[104] K. D. Housiadas, L. Wang, and A. N. Beris. "A new method preserving the positive definiteness of a second order tensor variable in flow simulations with application to viscoelastic turbulence". In: *Computers & Fluids* 39 (2010), pp. 225–241 (cit. on p. 20).

[105] P. Saramito. "On a modified non-singular log-conformation formulation for Johnson-Segalman viscoelastic fluids". In: *Journal of Non-Newtonian Fluid Mechanics* 211 (2014), pp. 16–30 (cit. on p. 20).

[106] P. Knechtges, M. Behr, and S. Elgeti. "Fully-implicit log-conformation formulation of constitutive laws". In: *Journal of Non-Newtonian Fluid Mechanics* 214 (2014), pp. 78–87 (cit. on p. 20).

[107] R. Comminal, J. Spangenberg, and J. H. Hattel. "Robust simulations of viscoelastic flows at high Weissenberg numbers with the streamfunction/log-conformation formulation". In: *Journal of Non-Newtonian Fluid Mechanics* 223 (2015), pp. 37–61 (cit. on p. 20).

[108] I. Hameduddin, C. Meneveau, T. A. Zaki, and D. F. Gayme. "Geometric decomposition of the conformation tensor in viscoelastic turbulence". In: *Journal of Fluid Mechanics* 842 (2018), pp. 395–427 (cit. on p. 20).

[109] M. A. Hulsen, R. Fattal, and R. Kupferman. "Flow of viscoelastic fluids past a cylinder at high Weissenberg number: Stabilized simulations using matrix logarithms". In: *Journal of Non-Newtonian Fluid Mechanics* 127 (2005), pp. 27–39 (cit. on p. 20).

[110] A. Afonso, P. J. Oliveira, F. T. Pinho, and M. A. Alves. "The log-conformation tensor approach in the finite-volume method framework". In: *Journal of Non-Newtonian Fluid Mechanics* 157 (2009), pp. 55–65 (cit. on p. 20).

[111] X. Chen, H. Marschall, M. Schäfer, and D. Bothe. "A comparison of stabilisation approaches for finite-volume simulation of viscoelastic fluid flow". In: *International Journal of Computational Fluid Dynamics* 27.6-7 (2013), pp. 229–250 (cit. on pp. 20, 29, 38).

[112] F. Habla, M. W. Tan, J. Haßlberger, and O. Hinrichsen. "Numerical simulation of the viscoelastic flow in a three-dimensional lid-driven cavity using the log-conformation reformulation in OpenFOAM®". In: *Journal of Non-Newtonian Fluid Mechanics* 212 (2014), pp. 47–62 (cit. on p. 20).

[113] I. L. Palhares Junior, C. M. Oishi, A. M. Afonso, and M. A. Alves. "Numerical study of the square-root conformation tensor formulation for confined and free-surface viscoelastic fluid flows". In: *Advanced Modeling and Simulation in Engineering Sciences* 3.2 (2016), pp. 1–23 (cit. on pp. 20, 51).

[114] R. S. Martins. "Numerical simulation of turbulent viscoelastic fluid flows: Flow classification and preservation of positive-definiteness of the conformation tensor". PhD thesis. France: Université Lille 1 - Sciences et Technologies, 2016 (cit. on p. 20).

[115] G. Mompean. "Modélisation des écoulements turbulents avec transferts thermiques en convection mixte". PhD thesis. France: École Centrale de Lyon, 1989 (cit. on p. 21).

[116] G. Mompean and M. Deville. "Unsteady finite volume simulation of Oldroyd-B fluid through a three-dimensional planar contraction". In: *Journal of Non-Newtonian Fluid Mechanics* 72 (1997), pp. 253–279 (cit. on pp. 21, 22).

[117] Y. Na and J. Y. Yoo. "A finite volume technique to simulate the flow of a viscoelastic fluid". In: *Computational Mechanics* 8 (1991), pp. 43–55 (cit. on p. 22).

[118] P. J. Oliveira, F. T. Pinho, and G. A. Pinto. "Numerical simulation of non-linear elastic flows with a general collocated finite-volume method". In: *Journal of Non-Newtonian Fluid Mechanics* 79 (1998), pp. 1–43 (cit. on p. 24).

[119] B. P. Leonard. "A stable and accurate convective modelling procedure based on quadratic upstream interpolation". In: *Computer Methods in Applied Mechanics and Engineering* 19 (1979), pp. 59–98 (cit. on pp. 24, 25).

[120] R. Courant, K. Friedrichs, and H. Lewy. "Über die partiellen Differenzengleichungen der mathematischen Physik". In: *Mathematische Annalen* 100.1 (1928), pp. 32–74 (cit. on p. 26).

[121] V. S. Patankar. *Numerical Heat Transfer and Fluid Flow*. New York: Hemisphere Publishing, 1980 (cit. on pp. 26, 54).

[122] P. G. Ciarlet, R. Glowinski, J. L. Lions, and J. Xu. *Numerical Methods for Non-Newtonian Fluids: Special Volume*. Volume XVI of Handbook of Numerical Analysis. Elsevier Science, 1990 (cit. on p. 27).

[123] C. W. Hirt, B. D. Nichols, and N. C. Romero. *SOLA - A numerical solution algorithm for transient fluid flows*. Los Alamos Scientific Laboratory report LA-5852. 1975 (cit. on p. 27).

[124] F. H. Harlow, J. P. Shannon, and J. E. Welch. "Liquid waves by computer". In: *Science* 149 (1965), pp. 1092–1093 (cit. on p. 27).

[125] F. H. Harlow and J. E. Welch. "Numerical calculation of time-dependent viscous incompressible flow of fluid with free surface". In: *Physics of Fluids* 8 (1965), pp. 2182–2189 (cit. on p. 27).

[126] A. A. Amsden and F. H. Harlow. "A simplified MAC technique for incompressible fluid flow calculations". In: *Journal of Computational Physics* 6 (1970), pp. 322–325 (cit. on p. 27).

[127] F. Durst, S. Ray, B. Ünsal, and O. A. Bayoumi. "The development lengths of laminar pipe and channel flows". In: *Journal of Fluids Engineering* 127.6 (2005), pp. 1154–1160 (cit. on pp. 31, 56).

[128] D. O. A. Cruz, F. T. Pinho, and P. J. Oliveira. "Analytical solutions for fully developed laminar flow of some viscoelastic liquids with a Newtonian solvent contribution". In: *Journal of Non-Newtonian Fluid Mechanics* 132 (2005), pp. 28–35 (cit. on p. 32).

[129] A. S. R. Duarte, A. I. P. Miranda, and P. J. Oliveira. "Numerical and analytical modeling of unsteady viscoelastic flows: The start-up and pulsating test case problems". In: *Journal of Non-Newtonian Fluid Mechanics* 154 (2008), pp. 153–169 (cit. on p. 33).

[130] V. Dallas, J. C. Vassilicos, and G. F. Hewitt. "Strong polymer-turbulence interactions in viscoelastic turbulent channel flow". In: *Physical Review E* 82 (2010), pp. 066303-1–066303-19 (cit. on p. 35).

[131] J. H. Ferziger. "A note on numerical accuracy". In: *International Journal for Numerical Methods in Fluids* 8 (1988), pp. 995–996 (cit. on p. 35).

[132] T. C. Ho and M. M. Denn. "Stability of plane Poiseuille flow of a highly elastic liquid". In: *Journal of Non-Newtonian Fluid Mechanics* 3 (1977), pp. 179–195 (cit. on p. 38).

[133] A. N. Morozov and W. van Saarloos. "An introductory essay on subcritical instabilities and the transition to turbulence in visco-elastic parallel shear flows". In: *Physics Reports* 447 (2007), pp. 112–143 (cit. on p. 38).

[134] L. Pan, A. Morozov, C. Wagner, and P. E. Arratia. "Nonlinear elastic instability in channel flows at low Reynolds numbers". In: *Physical Review Letters* 110 (2013), pp. 174502-1–174502-5 (cit. on p. 38).

[135] D. O. Canossi, R. Martins, and G. Mompean. "Numerical simulation of viscoelastic fluid flows in a planar cross-slot geometry". In: *Proceedings of the 16th Brazilian Congress of Thermal Sciences and Engineering*. Vitória, Espírito Santo, 2016 (cit. on pp. 40, 85).

[136] R. J. Poole, M. A. Alves, and P. J. Oliveira. "Purely elastic flow asymmetries". In: *Physical Review Letters* 99 (2007), pp. 164503-1–164503-4 (cit. on pp. 40, 45, 46, 50, 51, 63, 83, 85).

[137] F. A. Cruz, R. J. Poole, A. M. Afonso, F. T. Pinho, P. J. Oliveira, and M. A. Alves. "A new viscoelastic benchmark flow: Stationary bifurcation in a cross-slot". In: *Journal of Non-Newtonian Fluid Mechanics* 214 (2014), pp. 57–68 (cit. on pp. 40, 45, 47, 50, 51, 60, 64, 76, 83, 85).

[138] F. Pimenta and M. A. Alves. "Stabilization of an open-source finite-volume solver for viscoelastic fluid flows". In: *Journal of Non-Newtonian Fluid Mechanics* 239 (2017), pp. 85–104 (cit. on pp. 40, 54, 57, 59, 61).

[139] H. G. Weller, G. Tabor, H. Jasak, and C. Fureby. "A tensorial approach to computational continuum mechanics using object-oriented techniques". In: *Computers in Physics* 12.6 (1998), pp. 620–631 (cit. on pp. 40, 53, 59).

[140] E. S. G. Shaqfeh. "Purely elastic instabilities in viscometric flows". In: *Annual Review of Fluid Mechanics* 28 (1996), pp. 129–185 (cit. on p. 43).

[141] X.-B. Li, F.-C. Li, W.-H. Cai, H.-N. Zhang, and J.-C. Yang. "Very-low-*Re* chaotic motions of viscoelastic fluid and its unique applications in microfluidic devices: A review". In: *Experimental Thermal and Fluid Science* 39 (2012), pp. 1–16 (cit. on p. 43).

[142] R. G. Larson. "Instabilities in viscoelastic flows". In: *Rheologica Acta* 31 (1992), pp. 213–263 (cit. on pp. 43, 47).

[143] H. Giesekus. "Zur Stabilität von Strömungen viskoelastischer Flüssigkeiten". In: *Rheologica Acta* 5.3 (1966), pp. 239–252 (cit. on p. 43).

[144] S. J. Muller, R. G. Larson, and E. S. G. Shaqfeh. "A purely elastic transition in Taylor-Couette flow". In: *Rheologica Acta* 28 (1989), pp. 499–503 (cit. on p. 43).

[145] J. Zilz, R. J. Poole, M. A. Alves, D. Bartolo, B. Levaché, and A. Lindner. "Geometric scaling of a purely elastic flow instability in serpentine channels". In: *Journal of Fluid Mechanics* 712 (2012), pp. 203–218 (cit. on p. 43).

[146] F. J. Galindo-Rosales, L. Campo-Deaño, P. C. Sousa, V. M. Ribeiro, M. S. N. Oliveira, M. A. Alves, and F. T. Pinho. "Viscoelastic instabilities in micro-scale flows". In: *Experimental Thermal and Fluid Science* 59 (2014), pp. 128–139 (cit. on p. 43).

[147] G. H. McKinley, W. P. Raiford, R. A. Brown, and R. C. Armstrong. "Nonlinear dynamics of viscoelastic flow in axisymmetric abrupt contractions". In: *Journal of Fluid Mechanics* 223 (1991), pp. 411–456 (cit. on p. 43).

[148] P. Pakdel and G. H. McKinley. "Elastic instability and curved streamlines". In: *Physical Review Letters* 77.12 (1996), pp. 2459–2462 (cit. on p. 43).

[149] R. J. Poole. "Three-dimensional viscoelastic instabilities in microchannels". In: *Journal of Fluid Mechanics* 870 (2019), pp. 1–4 (cit. on pp. 43, 44).

[150] G. H. McKinley, P. Pakdel, and A. Öztekin. "Rheological and geometric scaling of purely elastic flow instabilities". In: *Journal of Non-Newtonian Fluid Mechanics* 67 (1996), pp. 19–47 (cit. on p. 43).

[151] T. M. Squires and S. R. Quake. "Microfluidics: Fluid physics at the nanoliter scale". In: *Reviews of Modern Physics* 77.3 (2005), pp. 977–1026 (cit. on p. 44).

[152] J. Soulages, M. S. N. Oliveira, P. C. Sousa, M. A. Alves, and G. H. McKinley. "Investigating the stability of viscoelastic stagnation flows in T-shaped microchannels". In: *Journal of Non-Newtonian Fluid Mechanics* 163 (2009), pp. 9–24 (cit. on p. 44).

[153] R. Dylla-Spears, J. E. Townsend, L. Jen-Jacobson, L. L. Sohn, and S. J. Muller. "Single-molecule sequence detection *via* microfluidic planar extensional flow at a stagnation point". In: *Lab on a Chip* 10 (2010), pp. 1543–1549 (cit. on p. 44).

[154] J. A. Odell and S. P. Carrington. "Extensional flow oscillatory rheometry". In: *Journal of Non-Newtonian Fluid Mechanics* 137 (2006), pp. 110–120 (cit. on pp. 44, 45).

[155] S. J. Haward. "Buckling instabilities in dilute polymer solution elastic strands". In: *Rheologica Acta* 49 (2010), pp. 1219–1225 (cit. on p. 45).

[156] S. J. Haward, J. A. Odell, M. Berry, and T. Hall. "Extensional rheology of human saliva". In: *Rheologica Acta* 50 (2011), pp. 869–879 (cit. on p. 45).

[157] O. Scrivener, C. Berner, R. Cressely, R. Hocquart, R. Sellin, and N. S. Vlachos. "Dynamical behaviour of drag-reducing polymer solutions". In: *Journal of Non-Newtonian Fluid Mechanics* 5 (1979), pp. 475–495 (cit. on p. 45).

[158] P. E. Arratia, C. C. Thomas, J. Diorio, and J. P. Gollub. "Elastic instabilities of polymer solutions in cross-channel flow". In: *Physical Review Letters* 96 (2006), pp. 144502-1–144502-4 (cit. on pp. 45, 46, 51, 63).

[159] P. C. Sousa, F. T. Pinho, and M. A. Alves. "Purely elastic flow instabilities in microscale cross-slot devices". In: *Soft Matter* 11 (2015), pp. 8856–8862 (cit. on pp. 45, 50, 51, 64, 83).

[160] O. G. Harlen, J. M. Rallison, and M. D. Chilcott. "High-Deborah-number flows of dilute polymer solutions". In: *Journal of Non-Newtonian Fluid Mechanics* 34 (1990), pp. 319–349 (cit. on pp. 45, 68).

[161] P. Becherer, A. N. Morozov, and W. van Saarloos. "Scaling of singular structures in extensional flow of dilute polymer solutions". In: *Journal of Non-Newtonian Fluid Mechanics* 153 (2008), pp. 183–190 (cit. on pp. 45, 68).

[162] S. J. Haward, T. J. Ober, M. S. N. Oliveira, M. A. Alves, and G. H. McKinley. "Extensional rheology and elastic instabilities of a wormlike micellar solution in a microfluidic cross-slot device". In: *Soft Matter* 8 (2012), pp. 536–555 (cit. on pp. 45, 51).

[163] D. O. A. Cruz and F. T. Pinho. "Analytical solution of steady 2D wall-free extensional flows of UCM fluids". In: *Journal of Non-Newtonian Fluid Mechanics* 223 (2015), pp. 157–164 (cit. on p. 45).

[164] S. T. Chaffin and J. M. Rees. "Viscoelastic Hele-Shaw flow in a cross-slot geometry". In: *European Journal of Mechanics - B/Fluids* 68 (2018), pp. 45–54 (cit. on p. 45).

[165] H. S. Hele-Shaw. "The flow of water". In: *Nature* 58 (1898), pp. 34–36 (cit. on p. 45).

[166] M. S. N. Oliveira, F. T. Pinho, R. J. Poole, P. J. Oliveira, and M. A. Alves. "Purely elastic flow asymmetries in flow-focusing devices". In: *Journal of Non-Newtonian Fluid Mechanics* 160 (2009), pp. 31–39 (cit. on p. 46).

[167] A. Varshney, E. Afik, Y. Kaplan, and V. Steinberg. "Oscillatory elastic instabilities in an extensional viscoelastic flow". In: *Soft Matter* 12 (2016), pp. 2186–2191 (cit. on pp. 46, 71, 83, 86).

[168] K. Gardner, E. R. Pike, M. J. Miles, A. Keller, and K. Tanaka. "Photon-correlation velocimetry of polystyrene solutions in extensional flow fields". In: *Polymer* 23.10 (1982), pp. 1435–1442 (cit. on p. 46).

[169] J. D. Crawford and E. Knobloch. "Symmetry and symmetry-breaking bifurcations in fluid dynamics". In: *Annual Review of Fluid Mechanics* 23 (1991), pp. 341–387 (cit. on p. 47).

[170] M. C. Cross and P. C. Hohenberg. "Pattern formation outside of equilibrium". In: *Reviews of Modern Physics* 65.3 (1993), pp. 851–1123 (cit. on p. 47).

[171] A. Groisman, M. Enzelberger, and S. R. Quake. "Microfluidic memory and control devices". In: *Science* 300 (2003), pp. 955–958 (cit. on p. 47).

[172] R. R. Lagnado, N. Phan-Thien, and L. G. Leal. "The stability of two-dimensional linear flows of an Oldroyd-type fluid". In: *Journal of Non-Newtonian Fluid Mechanics* 18 (1985), pp. 25–59 (cit. on pp. 47, 51).

[173] G. S. Paulo, C. M. Oishi, M. F. Tomé, M. A. Alves, and F. T. Pinho. "Numerical solution of the FENE-CR model in complex flows". In: *Journal of Non-Newtonian Fluid Mechanics* 204 (2014), pp. 50–61 (cit. on p. 47).

[174] H. J. Wilson. "Open mathematical problems regarding non-Newtonian fluids". In: *Nonlinearity* 25.3 (2012), R45–R51 (cit. on p. 47).

[175] S. J. Haward, R. J. Poole, M. A. Alves, P. J. Oliveira, N. Goldenfeld, and A. Q. Shen. "Tricritical spiral vortex instability in cross-slot flow". In: *Physical Review E* 93 (2016), pp. 031101-1–031101-5 (cit. on p. 47).

[176] K. Zografos, N. Burshtein, A. Q. Shen, S. J. Haward, and R. J. Poole. "Elastic modifications of an inertial instability in a 3D cross-slot". In: *Journal of Non-Newtonian Fluid Mechanics* 262 (2018), pp. 12–24 (cit. on p. 47).

[177] R. J. Poole, G. N. Rocha, and P. J. Oliveira. "A symmetry-breaking inertial bifurcation in a cross-slot flow". In: *Computers & Fluids* 93 (2014), pp. 91–99 (cit. on pp. 47, 56).

[178] A. M. Afonso, M. A. Alves, and F. T. Pinho. "Purely elastic instabilities in three-dimensional cross-slot geometries". In: *Journal of Non-Newtonian Fluid Mechanics* 165 (2010), pp. 743–751 (cit. on pp. 47, 51).

[179] R. G. Larson. "Turbulence without inertia". In: *Nature* 405 (2000), pp. 27–28 (cit. on p. 48).

[180] A. Fouxon and V. Lebedev. "Spectra of turbulence in dilute polymer solutions". In: *Physics of Fluids* 15.7 (2003), pp. 2060–2072 (cit. on pp. 48, 72, 86).

[181] R. J. Poole, B. Budhiraja, A. R. Cain, and P. A. Scott. "Emulsification using elastic turbulence". In: *Journal of Non-Newtonian Fluid Mechanics* 177–178 (2012), pp. 15–18 (cit. on p. 48).

[182] J. Mitchell, K. Lyons, A. M. Howe, and A. Clarke. "Viscoelastic polymer flows and elastic turbulence in three-dimensional porous structures". In: *Soft Matter* 12 (2016), pp. 460–468 (cit. on p. 48).

[183] N. Dubash, P. Cheung, and A. Q. Shen. "Elastic instabilities in a microfluidic cross-slot flow of wormlike micellar solutions". In: *Soft Matter* 8 (2012), pp. 5847–5856 (cit. on p. 51).

[184] F. A. Cruz, R. J. Poole, A. M. Afonso, F. T. Pinho, P. J. Oliveira, and M. A. Alves. "Influence of channel aspect ratio on the onset of purely-elastic flow instabilities in three-dimensional planar cross-slots". In: *Journal of Non-Newtonian Fluid Mechanics* 227 (2016), pp. 65–79 (cit. on p. 51).

[185] A. Limane, H. Fellouah, and N. Galanis. "Simulation of airflow with heat and mass transfer in an indoor swimming pool by OpenFOAM". In: *International Journal of Heat and Mass Transfer* 109 (2017), pp. 862–878 (cit. on p. 54).

[186] P. Beckstein, V. Galindo, and V. Vukčević. "Efficient solution of 3D electromagnetic eddy-current problems within the finite volume framework of *OpenFOAM*". In: *Journal of Computational Physics* 344 (2017), pp. 623–646 (cit. on p. 54).

[187] J. L. Favero, A. R. Secchi, N. S. M. Cardozo, and H. Jasak. "Viscoelastic flow analysis using the software OpenFOAM and differential constitutive equations". In: *Journal of Non-Newtonian Fluid Mechanics* 165 (2010), pp. 1625–1636 (cit. on p. 54).

[188] R. I. Issa. "Solution of the implicitly discretised fluid flow equations by operator-splitting". In: *Journal of Computational Physics* 62 (1985), pp. 40–65 (cit. on p. 54).

[189] J. P. van Doormall and G. D. Raithby. "Enhancements of the SIMPLE method for predicting incompressible fluid flows". In: *Numerical Heat Transfer* 7 (1984), pp. 147–163 (cit. on p. 54).

[190] M. A. Alves, P. J. Oliveira, and F. T. Pinho. "A convergent and universally bounded interpolation scheme for the treatment of advection". In: *International Journal for Numerical Methods in Fluids* 41 (2003), pp. 47–75 (cit. on p. 54).

[191] D. O. Canossi, G. Mompean, and S. Berti. "Elastic turbulence in two-dimensional cross-slot viscoelastic flows". *Submitted to Europhysics Letters (2019)* (cit. on p. 59).

[192] S. H. Strogatz. *Nonlinear Dynamics and Chaos*. Westview Press, 2000 (cit. on p. 64).

[193] B. A. Schiamberg, L. T. Shereda, H. Hu, and R. G. Larson. "Transitional pathway to elastic turbulence in torsional, parallel-plate flow of a polymer solution". In: *Journal of Fluid Mechanics* 554 (2006), pp. 191–216 (cit. on p. 69).

[194] G. I. Taylor. "The spectrum of turbulence". In: *Proceedings of the Royal Society of London A* 164 (1938), pp. 476–490 (cit. on p. 73).

[195] U. Frisch. *Turbulence: The legacy of A. N. Kolmogorov*. Cambridge: Cambridge University Press, 1995 (cit. on p. 73).

[196] T. Burghelea, E. Segre, and V. Steinberg. "Validity of the Taylor hypothesis in a random spatially smooth flow". In: *Physics of Fluids* 17 (2005), pp. 103101-1–103101-8 (cit. on p. 73).

[197] E. L. C. "VI" M. Plan, A. Gupta, D. Vincenzi, and J. D. Gibbon. "Lyapunov dimension of elastic turbulence". In: *Journal of Fluid Mechanics* 822.R4 (2017), R4-1–R4-12 (cit. on p. 73).

[198] J. Jiménez. "Algebraic probability density tails in decaying isotropic two-dimensional turbulence". In: *Journal of Fluid Mechanics* 313 (1996), pp. 223–240 (cit. on p. 75).

[199] K. R. Sreenivasan and R. A. Antonia. "The phenomenology of small-scale turbulence". In: *Annual Review of Fluid Mechanics* 29 (1997), pp. 435–472 (cit. on p. 75).

[200] A. Groisman and V. Steinberg. "Stretching of polymers in a random three-dimensional flow". In: *Physical Review Letters* 86.5 (2001), pp. 934–937 (cit. on p. 75).

Appendix A

Step-by-step algorithm for the Gilcart solver

This Appendix provides a detailed description of the algorithm for solving the discretised equations inside the finite-volume-based Gilcart flow solver, concerning a few different formulations and constitutive models. The numerical methods adopted for discretising such equations are described in Sections 2.2 and 2.3.

A.1 Standard formulation

- **Step 1**: Initialise the simulation

The input file is read, main variables are allocated then initialised, the geometric mesh is created following instructions given in the input file and output files are assigned with initial printings.

- **Step 2**: Evaluation of flow quantities

First step inside the main temporal loop: physical quantities such as velocity gradients, rate-of-strain tensor and fluid parameters are calculated.

- **Step 3**: Evaluate the extra-stress tensor $\boldsymbol{\tau}$

Here, the solver evolves the constitutive equation for the polymeric extra-stress, following the fluid model chosen. For the Oldroyd-B model (see Subsection 1.3.1, for details), the equation to be discretised is:

$$\boldsymbol{\tau} + \lambda \left[\frac{\partial \boldsymbol{\tau}}{\partial t} + \boldsymbol{\nabla} \cdot (\boldsymbol{u}\boldsymbol{\tau}) - \boldsymbol{\nabla}\boldsymbol{u}^T \cdot \boldsymbol{\tau} - \boldsymbol{\tau} \cdot \boldsymbol{\nabla}\boldsymbol{u} \right] = \eta_p \dot{\boldsymbol{\gamma}}. \tag{A.1}$$

In this case, the tensor $\boldsymbol{\tau}^{(n+1)}$ is evaluated explicitly for each component, depending only on the previous time step values of $\boldsymbol{\tau}^{(n)}$ and $\boldsymbol{u}^{(n)}$.
For the FENE-P model (whose constitutive equations are shown in Subsection 1.3.2), we solve the evolution equation for the conformation tensor $\boldsymbol{c}^{(n+1)}$, by discretising the equation

$$\frac{D\boldsymbol{c}}{Dt} = \boldsymbol{c}\cdot\boldsymbol{\nabla u} + \boldsymbol{\nabla u}^T\cdot\boldsymbol{c} + \frac{1}{\lambda}\left[\boldsymbol{I} - \frac{\boldsymbol{c}}{1-\dfrac{tr(\boldsymbol{c})}{L^2}}\right], \tag{A.2}$$

for the components of $\boldsymbol{c}^{(n+1)}$, which will depend only on previous time step values of $\boldsymbol{c}^{(n)}$ and $\boldsymbol{u}^{(n)}$. Afterwards, we recover $\boldsymbol{\tau}^{(n+1)}$ from tensor $\boldsymbol{c}^{(n+1)}$, by using the relation

$$\boldsymbol{\tau} = \frac{\eta_p}{\lambda}\left[\frac{\boldsymbol{c}}{1-\dfrac{tr(\boldsymbol{c})}{L^2}} - \boldsymbol{I}\right]. \tag{A.3}$$

- **Step 4**: Calculate the global term $\boldsymbol{S}(\boldsymbol{u})$

Equation A.4 is evaluated for all three components of this function of the velocity field and extra-stress tensor,

$$\boldsymbol{S}(\boldsymbol{u}) = \frac{\boldsymbol{u}}{\Delta t} + \boldsymbol{\nabla}\cdot\left(\nu_0\,\boldsymbol{\nabla u} + \frac{1}{\rho}\boldsymbol{\tau} - \boldsymbol{uu}\right). \tag{A.4}$$

It is important to remark that for this equation, the velocity components and velocity gradients are evaluated at previous time step $\boldsymbol{u}^{(n)}$, but the extra-stress tensor values used have already been updated in the previous inner step to $\boldsymbol{\tau}^{(n+1)}$.

- **Step 5**: Solve the implicit equation for the pressure field

The numerical code sets and solves the linear system $\boldsymbol{A}\,p^{(n+1)} = \boldsymbol{B}^{(n)}$ (detailed in the final part of Subsection 2.2.2) for the unknown pressures at current time step.

- **Step 6**: Evaluate the velocity field $\boldsymbol{u}^{(n+1)}$

With the pressure field $p^{(n+1)}$ calculated in the previous inner step, the velocity field $\boldsymbol{u}^{(n+1)}$ is updated at the current time step, using Eq. A.5,

$$\boldsymbol{u}^{(n+1)} = \Delta t\left[S(\boldsymbol{u})^{(n)} - \frac{1}{\rho}\boldsymbol{\nabla}p^{(n+1)}\right]. \tag{A.5}$$

- **Step 7**: Advance in time

The algorithm then sets $n+1 \rightarrow n$ and repeats steps $2-7$ until numerical convergence is attained or another stopping criterion is met.

A.2 Square-root technique

Taking into account the code implementations detailed in Section 2.3, some intermediate procedures have to be executed between steps 2 and 3 of Section A.1.

- **Step 2.1**: Calculate the square-root tensor and numerically evolve it

Firstly, the conformation tensor $\boldsymbol{c}^{(n)}$ is retrieved from the extra-stress tensor calculated at previous time step, using Eq. 1.13, and its unique SPD square-root $\boldsymbol{b}^{(n)}$ is determined. This tensor then evolves following:

$$\left(\frac{\partial \boldsymbol{b}}{\partial t} + \boldsymbol{u}\cdot\boldsymbol{\nabla}\boldsymbol{b}\right) - \boldsymbol{b}\cdot\boldsymbol{\nabla}\boldsymbol{u} - \boldsymbol{a}\cdot\boldsymbol{b} + \frac{\boldsymbol{b}-\boldsymbol{b}^{-1}}{2\lambda} = 0\,. \tag{A.6}$$

- **Step 2.2**: Retrieve the extra-stresses tensor

In this second and final step, the tensors $\boldsymbol{c}^{(n+1)}$ and $\boldsymbol{\tau}^{(n+1)}$ are obtained directly from $\boldsymbol{b}^{(n+1)}$, using Eqs. 2.32 and 1.13, and the algorithm advances to step 3.

Appendix B

Analytical solution of the steady velocity field for a channel flow

In Subsection 2.4.2, we have displayed the analytical solution for the steady-state velocity field, for a plane channel geometry. In the present Appendix, we present the details of the solution. We rewrite here the momentum equation under fully developed flow conditions (Eq. 2.43) to be solved analytically,

$$\frac{\partial}{\partial y}\left(\eta_s \frac{\partial u}{\partial y} + \tau_{xy}\right) = \frac{\partial p}{\partial x}. \tag{B.1}$$

The shear component of the extra-stress tensor is directly recovered from the corresponding component of the Oldroyd-B constitutive equation presented in Eq. 1.9,

$$\tau_{xy} = \eta_p \frac{\partial u}{\partial y}. \tag{B.2}$$

Replacing Eq. B.2 into Eq. B.1 leads to

$$\frac{\partial^2 u}{\partial y^2} = \frac{1}{\eta_t}\frac{\partial p}{\partial x}, \tag{B.3}$$

where we recall that $\eta_t = \eta_s + \eta_p$.

From the wall-normal component of the Navier-Stokes equation, we can verify that the derivative $\partial p/\partial y = 0$, which implies that $p(x)$ is a function only of $x-$component and hence the gradient dp/dx is a parameter of the problem. Defining the channel superior and inferior boundaries at $+L$ and $-L$ (see Fig. 2.2), this differential equation can now be integrated twice, applying the no-slip condition at both walls:

$$u(-L) = 0, \qquad u(+L) = 0. \tag{B.4}$$

This operation yields the solution:

$$u(y) = \frac{1}{2\eta_t}\frac{\partial p}{\partial x}\left(y^2 - L^2\right). \tag{B.5}$$

The channel average velocity can be calculated by an integration over the channel cross section:

$$u_{avg} = \frac{1}{2L}\int_{-L}^{L} u(y)\,dy = \frac{-L^2}{3\eta_t}\frac{\partial p}{\partial x}. \tag{B.6}$$

We can thus express Eq. B.5 in terms of the average velocity defined by Eq. B.6, finally obtaining a closed-form solution in the form of a parabolic velocity profile, as we should expect for this problem:

$$u(y) = \frac{3}{2}\cdot u_{avg}\left[1 - \left(\frac{y}{L}\right)^2\right]. \tag{B.7}$$

Appendix C

Stretching factor for geometric meshes

In Subsection 4.2.2, general aspects of the computational mesh created for the cross-slot geometry were presented. We detail below the derivation procedure of the equation for the stretching factor, Eq. 4.4.

A general geometric progression (GP) with first term a_1 and ratio r has the sequence formation:

$$a_1, a_1 \cdot r, a_1 \cdot r^2, \ldots, a_1 \cdot r^{n-1}, a_1 \cdot r^n . \tag{C.1}$$

In order to find the n^{th} term of such geometric progression, defined here as a_n, we use the formula

$$a_n = a_1 \cdot r^{n-1} . \tag{C.2}$$

The n^{th} partial sum of the GP (S_n) is

$$S_n = \sum_{k=1}^{n} a_k = \frac{a_1 (1 - r^n)}{1 - r}, \qquad r \neq 1 . \tag{C.3}$$

In our analysis, we define the *stretching factor* we are looking for (f_s) as equivalent to r; the partial sum S_n represents the summation of the lengths of all mesh elements in the direction under consideration, coinciding with the arm length L_a.

To obtain a smooth transition to the neighbouring mesh configuration, we consider the first element of the contiguous mesh to be part of the same GP, as the a_{n+1} term. Here, such element belongs to the central square of the cross-slot geometry. Taking into account the uniform grid size in the central zone and Eq. C.2, we have:

$$a_{n+1} = \frac{d}{N} = a_1 \cdot {f_s}^N , \tag{C.4}$$

where d represents the arm width and N is the number of cells in the central square, which we set to be equal to the number of arm cells (n) in the refining direction. We recall that we used here $r = f_s$. Substituting Eq. C.4 in Eq. C.3 yields

$$L_a = \frac{d\left(1 - {f_s}^N\right)}{N \cdot {f_s}^N (1 - f_s)}, \tag{C.5}$$

identifying here that $S_n = L_a$. Defining the length-to-width aspect ratio for the cross-slot arm as

$$A_r = \frac{L_a}{d}, \tag{C.6}$$

and using Eq. C.5, the stretching factor f_s is the only positive solution of the non-linear algebraic equation

$$\frac{1 - {f_s}^N}{1 - f_s} = A_r \cdot N \cdot {f_s}^N. \tag{C.7}$$

Appendix D

Validation of the algorithm for Lagrangian tracers

We report here a validation of the algorithm used for advecting Lagrangian tracers, written in C++ language inside the OpenFOAM® code. This 2^{nd} order Runge-Kutta algorithm was employed to evaluate mixing properties of turbulent-like flows in Section 5.7.

We consider here a steady and laminar flow through our two-dimensional cross-slot, with $\beta = 1/9$ and $Wi = 0.1$, thus below the onset of purely elastic instabilities. After an initial transient corresponding to a duration of 100λ, we place four tracers in specific locations, represented in Fig. D.1 as $T_{(1,2,3,4)}$. Particles $T_{(1,2,3)}$ are placed in the same vertical axis $x = -5$ and at $y-$positions $y_{(1,2,3)} = (0.4, 0, -0.15)$; and particle T_4 is placed at the geometrical centre of the cross-slot ($x_4 = y_4 = 0$).

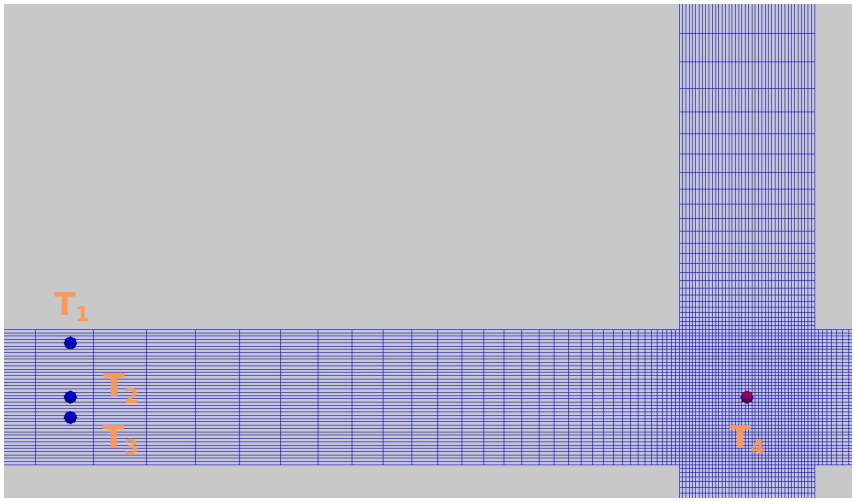

Figure D.1 – Initial position of Lagrangian tracers (see text) for performing a validation of the algorithm. $M50$ mesh was adopted here.

Tracers' path after their injection inside the flow are displayed in Figs. D.2 (normalised $x-$coordinate) and D.3 (normalised $y-$coordinate) for all four particles as a

function of non-dimensional time, with respective analytical solutions for validation purposes.

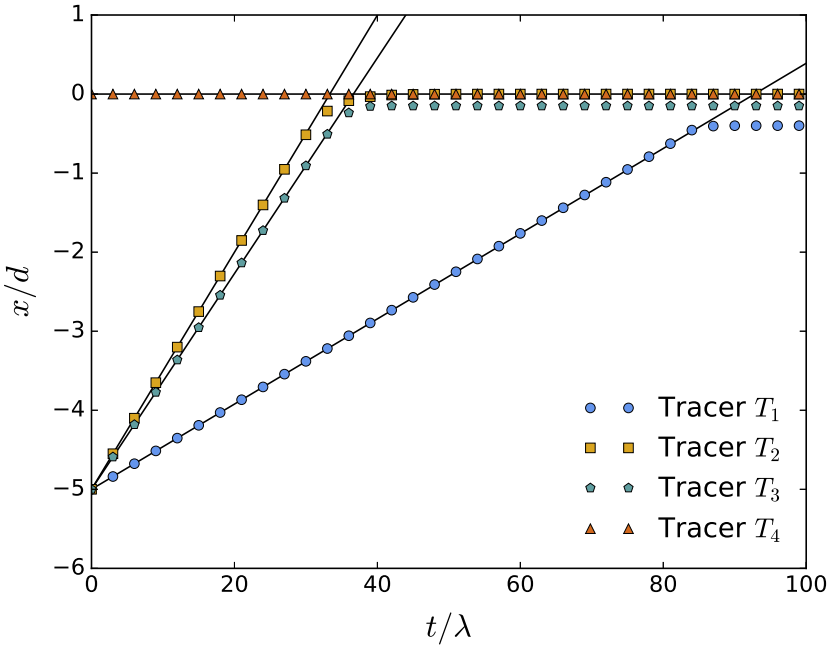

Figure D.2 – Temporal evolution of tracers' $x-$coordinate, for $\beta = 1/9$ and $Wi = 0.1$. The solid black lines are analytical curves for the particles' path in a laminar Oldroyd-B channel flow.

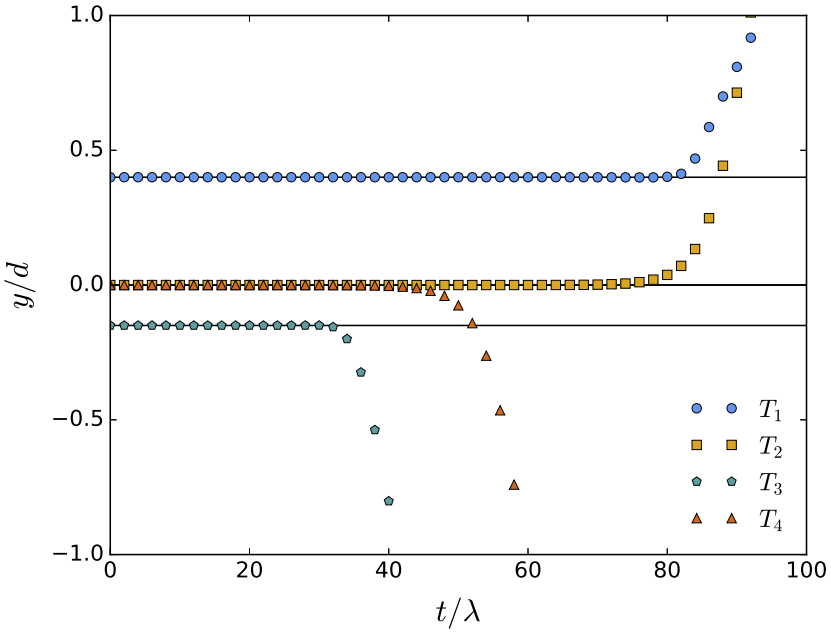

Figure D.3 – Temporal evolution of tracers' $y-$coordinate, for $\beta = 1/9$ and $Wi = 0.1$. The solid black lines are analytical curves for the particles' path in a laminar Oldroyd-B channel flow.

Appendix E

Viscoelastic flows of FENE-P fluids

We introduced and detailed the FENE-P model in Subsection 1.3.2, where we presented it as an improved (in the sense of physical coherence) constitutive equation in comparison to the linear elastic Oldroyd-B model. For the sake of comparison, we make here some brief (and preliminary) comments on this viscoelastic model, for which a concise numerical study has been performed, using the $M50$ mesh.

The maximum extensibility of the polymer molecules in this model is controlled by the L^2 parameter, which varied from 400 to 10^4 in our analysis. We also kept the viscosity ratio fixed at $\beta = 1/9$, $Re = 0$ and increased Wi aiming to characterise the levels of elasticity corresponding to the cross-slot purely elastic instabilities. For the FENE-P concentrated solutions analysed here, we observed that the flow always transitions initially to the steady asymmetric state, taking into account the range of the L^2 parameter exploited; when Wi is further increased, the second (and unsteady) transition also sets in, for $L^2 \geq 400$.

We conclude this discussion by compiling in Tab. E.1 the critical Weissenberg $Wi_c^{(\mathrm{I,II})}$ for the transitions to steady asymmetric and unsteady flows, at $\beta = 1/9$ and for increasing values of the L^2 parameter (including the limiting case $L^2 \to \infty$, equivalent to the Oldroyd-B model).

L^2	$Wi_c^{(\mathrm{I})}(\pm 0.005)$	$Wi_c^{(\mathrm{II})}$
400	0.375	2.35 ± 0.05
625	0.375	2.25 ± 0.05
900	0.375	1.75 ± 0.05
1600	0.365	1.65 ± 0.05
2500	0.365	1.65 ± 0.05
10000	0.365	1.55 ± 0.05
∞	0.365	1.54 ± 0.01

Table E.1 – $Wi_c^{(\mathrm{I})}$ and $Wi_c^{(\mathrm{II})}$ for multiple L^2 parameters of the FENE-P model, with $\beta = 1/9$. The limiting case $L^2 \to \infty$ is equivalent to the Oldroyd-B model.

Contents

Numerical simulation of the transition to elastic turbulence in viscoelastic inertialess flows

Abstract

Fluid mixing represents an important component of the field of fluid dynamics, what makes the understanding of this subject so meaningful from both the fundamental and applied (*e.g.* industrial processes) point of view. In miniaturised geometries, under typical conditions, mixing is a slow, difficult and inefficient process due to the naturally laminar character of these flows, which forces the homogenisation of different fluid elements to occur via molecular diffusion instead of faster-acting advective transport. However, recent experimental studies on low-Reynolds-number viscoelastic flows have shown that efficient mixing can be triggered in several geometrical configurations (including micro-scale devices), by the phenomenon of elastic turbulence. The first part of this thesis is devoted to the understanding and investigation of numerical challenges present in the domain of non-Newtonian fluid dynamics, focusing in particular on the high-Weissenberg number problem. The latter manifests as a breakdown of the numerical scheme when the polymeric extra-stress evolution equations are implemented in a direct way, which poses severe limits to the possibility to accurately simulate elastic turbulent flows. We provide numerical evidence of the beneficial effect (in terms of increased stability) of the square-root decomposition of the extra-stress in a finite-volume-based implementation of the governing equations in a two-dimensional channel. The second part of the thesis reports about the emergence and characterisation of purely elastic instabilities in numerical simulations of zero-Reynolds-number Oldroyd-B fluids in a two-dimensional cross-slot geometry. By means of extensive numerical work, we provide a detailed characterisation of the purely elastic instabilities arising in the system for wide ranges of both the fluid elasticity and the polymer concentration. For concentrated solutions and large enough Weissenberg numbers, our simulations indicate the emergence of disordered flow pointing to elastic turbulence. We analyse the transition to irregular dynamics and characterise the statistical properties of such highly elastic flows, discussing the similarities and differences with experimental results from the literature.

Keywords: numerical simulation, elastic turbulence, viscoelastic fluid, cross-slot, high-Weissenberg number problem, finite-volume method, Oldroyd-B, OpenFOAM, mixing

Unité de Mécanique de Lille - Joseph Boussinesq
(UML) EA 7512 – Université de Lille - Cité Scientifique – Bâtiment ESPRIT – Avenue Henri Poincaré – 59655 Villeneuve d'Ascq, France

Simulation numérique de la transition à la turbulence élastique dans des écoulements viscoélastiques sans inertie

Résumé

Le mélange de fluides représente un élément important du domaine de la dynamique des fluides, ce qui rend la compréhension de ce sujet si significative du point de vue fondamental et appliqué (*p. ex.*, les processus industriels). Dans les géométries miniaturisées (dans des conditions typiques) le mélange est un processus lent, difficile et inefficace. Cela en raison du caractère naturellement laminaire de ces écoulements, qui oblige l'homogénéisation de différents éléments fluides à se produire par diffusion moléculaire au lieu d'un transport advectif, à l'action plus rapide. Cependant, des études expérimentales récentes sur les écoulements viscoélastiques à faible nombre de Reynolds ont montré qu'un mélange efficace peut être déclenché dans plusieurs configurations géométriques (y compris les dispositifs à l'échelle microscopique), par le phénomène de la turbulence élastique. La première partie de cette thèse est consacrée à la compréhension et à l'investigation des défis numériques présents dans le domaine de la dynamique des fluides non newtonienne, en se concentrant plus particulièrement au problème du haut nombre de Weissenberg. Ce dernier se manifeste par une rupture du schéma numérique, lorsque les équations d'évolution d'extra-contraintes polymériques sont évaluées de façon directe. Ceci pose des limites importantes à la possibilité de simuler avec précision des écoulements turbulents-élastiques. Nous fournissons des preuves numériques de l'effet bénéfique (en termes de gain en stabilité) de la décomposition en racine carrée de l'extra-contrainte dans une implémentation en volumes finis des équations régissant l'écoulement dans un canal bidimensionnel. La deuxième partie de la thèse traite de l'émergence et de la caractérisation d'instabilités purement élastiques dans des simulations numériques de fluides Oldroyd-B à nombre de Reynolds zéro dans une géométrie du type *cross-slot* bidimensionnel. Grâce à un travail numérique approfondi, nous présentons une caractérisation détaillée des instabilités purement élastiques. Ces instabilités apparaissant dans le système pour de larges plages d'élasticité du fluide et de concentration des polymères. Pour les solutions concentrées et des nombres de Weissenberg assez grands, nos simulations indiquent l'apparition d'un écoulement désordonné pointant vers la turbulence élastique. Nous analysons le passage à une dynamique irrégulière et caractérisons les propriétés statistiques de tels écoulements très élastiques, en discutant des similitudes et des différences avec les résultats expérimentaux de la littérature.

Mots clés : simulation numérique, turbulence élastique, fluide viscoélastique, cross-slot, problème du haut nombre de Weissenberg, méthode des volumes finis, Oldroyd-B, OpenFOAM, mélange